Politecnico di Torino

Master of Science in Building Engineering

Department of Structural, Geotechnical and Building Engineering

Academic Year 2023/2024

October 2024

Knowledge of submerged cultural heritage through high resolution digital photogrammetry

Supervisor:

Andrea Maria Lingua

Co-supervisors:

Filiberto Chiabrando

Francesca Matrone

Candidate:

Erica Forti

A voi,

che ci avete dato tutto

Abstract

The sea covers more than 70 per cent of the earth's surface, representing an essential resource for life on the planet. This vast ecosystem is home to rich biodiversity and provides crucial resources for environmental balance and human well-being. Key elements such as coral reefs, posidonia meadows, marine fauna and ocean currents help stabilise the climate and absorb around 30% of global carbon dioxide. In addition to its ecological importance, the sea holds an underwater cultural heritage of great value, such as ancient shipwrecks and underwater cities, historical and archaeological evidence of our civilisation. However, pollution, overfishing, climate change and erosion threaten both marine ecosystems and these cultural assets. Preserving the sea, its natural elements and underwater heritage is crucial to ensure environmental sustainability and protect our cultural heritage.

Preservation is problematic for assets that are found on land, and for submerged assets the criticality increases considerably. For this reason, it is necessary to collect and analyse data that allow us to enhance and safeguard these assets in the best possible way. The Archimedes project aims to map, analyse and enhance these assets in different environments.

The environmental aspect is also of great importance. Constant monitoring of the marine environment allows changes to be observed. The Poseidon project aims to monitor the flora and fauna of the marine environment in order to assess possible interventions.

In this dissertation some techniques for underwater data collection and analysis using a photogrammetric approach will be shown.

Particular attention has been paid to the camera calibration phase, a fundamental part of underwater surveys. Different softwares ware used, which allowed to do direct comparisons. It was also evaluated which type of data is best to minimize the presence of distortions.

Another analysis that has been addressed is that of radiometric calibration of the data. The depth at which the submerged asset is located is closely related to the presence of light and this affects both the data acquisition phase and the processing phase.

The processed data are part of two different datasets. The first one was acquired at Coluccia Island (Sardinia) and the second one was acquired at Porto Cesareo (Apulia). Both datasets were acquired in shallow water.

As a final analysis, the calibration of images acquired with a new dual-camera system with the presence of a dome was done to reduce the presence of distortions in the data acquisition phase.

It is important to remember that the underwater heritage is part of our history and culture and it is our duty to safeguard it, but not only that. The Archimedes project aims not only to analyze these assets, but also to make them accessible to underwater and non-underwater tourism, through means such as virtual reality. In this way, the entire heritage, which is accessible to those with specific expertise, is made reachable to a much wider audience.

Il mare copre più del 70% della superficie terrestre, rappresentando una risorsa essenziale per la vita sul pianeta. Questo vasto ecosistema ospita una ricca biodiversità e fornisce risorse cruciali per l'equilibrio ambientale e il benessere umano. Elementi chiave come le barriere coralline, le praterie di posidonia, la fauna marina e le correnti oceaniche contribuiscono a stabilizzare il clima e ad assorbire circa il 30% del biossido di carbonio globale. Oltre alla sua importanza ecologica, il mare custodisce un patrimonio culturale sottomarino di grande valore, come antichi relitti di navi e città sommerse, testimonianze storiche e archeologiche della nostra civiltà. Tuttavia, l'inquinamento, la pesca eccessiva, il cambiamento climatico e l'erosione minacciano sia gli ecosistemi marini sia questi beni culturali. Preservare il mare, i suoi elementi naturali e il patrimonio sottomarino è cruciale per garantire la sostenibilità ambientale e proteggere il nostro patrimonio culturale.

La conservazione è problematica per i beni che si trovano sulla terraferma, e per quelli sommersi la criticità aumenta considerevolmente. Per questo motivo, è necessario raccogliere e analizzare dati che ci permettano di valorizzare e tutelare questi beni nel miglior modo possibile. Il progetto Archimede si propone di mappare, analizzare e valorizzare questi beni in diversi ambienti.

Anche l'aspetto ambientale riveste grande importanza. Il monitoraggio costante dell'ambiente marino permette di osservare i cambiamenti. Il progetto Poseidone mira a monitorare la flora e la fauna dell'ambiente marino per valutare possibili interventi.

In questa tesi verranno presentate alcune tecniche per la raccolta e l'analisi dei dati sottomarini utilizzando un approccio fotogrammetrico. Particolare attenzione è stata dedicata alla fase di calibrazione della fotocamera, una parte fondamentale delle indagini sottomarine. Sono stati utilizzati diversi software, che hanno

permesso di effettuare confronti diretti. È stato inoltre valutato quale tipo di dati sia il migliore per ridurre al minimo la presenza di distorsioni.

Un'altra analisi affrontata è quella della calibrazione radiometrica dei dati. La profondità alla quale si trova il bene sommerso è strettamente legata alla presenza di luce, e questo influisce sia sulla fase di acquisizione dei dati che su quella di elaborazione.

I dati elaborati fanno parte di due set di dati distinti. Il primo è stato acquisito all'Isola di Coluccia (Sardegna) e il secondo a Porto Cesareo (Puglia). Entrambi i set di dati sono stati acquisiti in acque poco profonde.

Come analisi finale, è stata effettuata la calibrazione delle immagini acquisite con un nuovo sistema a doppia fotocamera con la presenza di una cupola per ridurre la presenza di distorsioni nella fase di acquisizione dei dati.

È importante ricordare che il patrimonio sottomarino fa parte della nostra storia e cultura, ed è nostro dovere salvaguardarlo, ma non solo. Il progetto Archimede mira non solo ad analizzare questi beni, ma anche a renderli accessibili al turismo subacqueo e non subacqueo, tramite mezzi come la realtà virtuale. In questo modo, l'intero patrimonio, che è accessibile solo a chi ha competenze specifiche, diventa fruibile per un pubblico molto più ampio.

Contents

List of figures

14

List of tables

Introduction

The sea, which covers more than 70% of the earth's surface [1], is one of the planet's largest and most complex ecosystems and a vital resource for the survival of many species. With its crucial role in climate regulation, the sea contributes to the absorption of around 30% of the carbon dioxide (CO_2) produced globally [2], reducing the effects of global warming. In addition, its currents regulate temperatures and atmospheric circulation, influencing climate patterns on a global scale. However, the importance of the sea goes far beyond environmental issues alone, as it is also an immense reservoir of biodiversity and a bridge to the past thanks to the many underwater cultural assets it holds.

Among the sea's most prominent features are its coral reefs, which, while covering less than 1% of the ocean floor, are home to around 25% of all marine species [3]. These ecosystems are often referred to as the 'rainforests of the sea' because of their ability to host a wide variety of organisms. Posidonia meadows, another key element, perform a similar function to terrestrial forests: they absorb large amounts of CO_2 and provide shelter and food for many marine species.

Ocean currents play a crucial role in regulating global temperature by distributing heat from equatorial to polar regions. This mechanism helps stabilise the climate and makes large areas of the planet habitable. However, changes in the circulation of currents due to global warming could cause severe climate alterations, with devastating effects on a global scale.

Despite its enormous ecological importance, the sea is under unprecedented pressure. Plastic pollution is one of the most visible and serious threats, with around 8 million tonnes of plastic ending up in the oceans every year[4], harming marine wildlife and contaminating

the food chain. Other forms of pollution, such as chemical and nutrient pollution, are causing phenomena such as dead zones in the seas, where oxygen is so scarce as to make marine life unsustainable.

Climate change is making this situation even worse. Warming sea waters lead to coral bleaching, melting polar ice caps and rising sea levels, threatening coastal populations and marine ecosystems. Overfishing is depleting fish stocks, endangering the food security of millions of people and altering the balance of marine ecosystems.

In addition to its ecological importance, the sea holds a vast underwater cultural heritage. Shipwrecks, underwater cities and archaeological finds represent a unique historical record of our civilisation. These cultural assets offer a valuable insight into the past, telling stories of trade, war, exploration and colonisation. The Italian coasts are rich in underwater historical proofs.

The protection of these cultural assets is as important as the preservation of natural ecosystems. However, they are threatened by coastal erosion, pollution and, in some cases, human activities such as looting and unregulated tourism. Preserving this heritage not only enriches our historical knowledge, but also contributes to the growth of sustainable cultural tourism.

Preserving the sea means protecting not only an invaluable natural environment, but also a cultural and historical resource that enriches our understanding of the past. It is essential to adopt sustainable management strategies that reduce pollution, promote responsible fishing and combat climate change. In addition to this, it is crucial to improve the protection of submerged cultural assets through international collaboration and a growing commitment to research and conservation.

The sea is not only a source of economic and food resources, it is the beating heart of the global ecological balance and a bridge between past and present. Protecting it means ensuring a sustainable future for generations to come.

The projects presented in this dissertation aim to understand and preserve both the ecological and cultural heritage aspects of the marine environment. Results obtained in different survey campaigns under different environmental conditions will be presented. Technologies and techniques and their limitations will be shown. Their purpose is not only to acquire data for processing, but also to raise awareness of issues that are not yet widely addressed, but are of great relevance.

The projects: Archimedes and Poiseidon

2.1 Archimedes

The Archimedes [5] project was created with the purpose of studying, developing and testing innovative archeometry technologies and methodologies to provide knowledge, high resolution investigation, monitoring for the preservation "in situ" and valorization of the ancient shipwrecks indifferent depths. The finds harder to enhance, document and make them accessible are the ones from the Protohistoric Ages to the Middle Ages because of their position, depth and fragility. The ability and the possibility to document these finds are currently complex for the underwater world, while for the heritage and the environment on land there are numerous geomatic solutions. Currently it is possible to speed up and reduce the cost of the archeologists' work, ensuring safety conditions during the underwater procedures, thanks to the use of underwater photogrammetry and integrations of various type of cameras and sensors - like sonar and multibeam - installed on underwater or aerial drones operated remotely. This new method of underwater survey also allows documentation and mapping of greater depths at considerable extents.

Currently the underwater heritage is available to a few people and the technologies developed with the project aim to reduce this gap, with immersive tours and 3D models. The project main focus can be described as:

1. increase knowledge of submerged architectural heritage, with supervision and conservation;
2. safety of work operations;

25

3. expand accessibility by bringing virtual tools to the public that allow them to enhance underwater heritage.

2.1.1 Underwater archaeological sites

Underwater archaeological sites strongly depend on the chemical-physical characteristics of the environment in which they are located, on the nature of the seabed and on faunal disturbances. Submerged deposits consisting of shipwrecks can be divided into three categories:

- beached wrecks: beached wrecks are sometimes exceptionally preserved thanks to the rapid covering process and the "trap effect". Their low depth, the constant presence of wave motion and the easy fruition create problems to the investigation;
- submerged wrecks at low/medium depth, near the coast or offshore: sites that are within 35 m of depth are considered as such. These are much more exposed to plundering, less subject to monitoring and disturbed by trawling or shellfish fishing as it causes an alteration of the bottom, creating a sort of "plowing" in the perimeter areas of the hull. Furthermore, the survey and accessibility are subject to strong regulatory obligations which make the site accessible only to a small number of divers;
- deep wrecks: those who are below 60 m are considered as such. They are optimally preserved thanks to a series of factors such as cold, lack of light and low oxygen levels. This depth, however, represents a difficulty for the accessibility and use of these sites. Other problems that can be encountered in these situations are systematic looting, repeated trawling and treasure hunting which can cause the loss of a large amount of information.

From a geomatic point of view, the presence of water does not allow professionals to act as easily as in the terrestrial field. For this reason, further investigations are needed such as:
- use of high-resolution images
- photogrammetric camera and radiometric correction;

- correction of color distortion caused by light traveling through water;
- underwater and marine positioning and navigation which is also linked to the navigation of Remotely Operated Vehicles (ROV) and Uncrewed Surface Vessels (USV), a fundamental element for 3D reconstruction and monitoring. Underwater positioning is challenging due to attenuation of Global Navigation Satellite Systems (GNSS);
- creation, visualization and circulation of 3D models are an alternative to direct access to these sites. It also improves data sharing between professionals.

Underwater cultural heritage constitutes a priceless resource, ecologically, educationally and economically, which requires recognition and appropriate treatment to continue to provide significant benefits to humanity. After the UNESCO Convention on the Protection of Underwater Cultural Heritage (2001), a new phase of the process of re-appropriation of cultural heritage was implemented. This development implies risks and opportunities for the protection, since not all Underwater Cultural Heritage can be enjoyed through direct access for various reasons: location, depth and safety/integrity of the Cultural Heritage, but also safety and immersion skills of researchers, citizens, stakeholders and tourists.

2.1.2 The aim of the project

The project aims to provide methodologies and tools for the documentation and use of the submerged archaeological heritage with safety measures, bringing the find to the "surface" using digital technologies and virtual, increased and mixed reality.

Furthermore, we want to improve historical knowledge of the areas analysed, of the wrecks and of the trade routes from the Bronze Age to the Modern Age in the Mediterranean. These data are also used with the aim of identifying and cataloging the submerged heritage, focusing on the Ionian-Adriatic area. Another objective concerns the geoarchaeological field with the aim of promoting research on changes in sea level and changes in coastal areas. As a final objective, the project aims to develop and test a non-invasive multi-sensor 3D detection system that is capable of providing high-resolution surveys and monitoring for a wide range of underwater applications and it is capable of operating at medium and high depths, in order to reduce risks for operators in the field.

The study of these Cultural Heritages is the combination of the work of different specialists which aims to redesign the physiognomy of the landscapes in the various phases and includes the forms and methods of population, which have evolved over time. The main tool of landscape/seascape archeology is webGIS, which allows to collect permanent knowledge of every single cultural asset and to update it over time. Therefore, it represents a form of objectification of the Cultural Heritage: it is the place of "certification" and even of the existence of Cultural Heritage - in fact, a Cultural Heritage "does not exist" if it is not cataloged.

To date, high resolution 3D reconstruction, radiometric correction capability and positioning in the underwater context are still open questions. The project includes testing and validation phases focused on underwater archaeological and Cultural Heritage to demonstrate the versatility and suitability of the proposed methodologies and techniques. The project will therefore provide technological and methodological tools suitable to provide a tangible solution to the needs of real applications. In particular, the definition of a methodological protocol for the positioning, traditional and 3D documentation and digital valorisation of the wrecks of ancient boats (especially the remains of wooden hulls) at different depths.

The project is divided in five different stages:
1. condition of the art piece, new archaeological investigations and implementation of webGIS: preliminary reconnaissance of the condition of the art piece, supported by the most recent archaeological investigation campaigns, aimed at the implementation of webGIS of the ancient wrecks in the Ionian-South Adriatic. This stage involves collecting all the information already available relating to the sites at different depths in the areas, and carrying out a harmonization of the data which includes bibliographic and archival documentation, aerial images, scattered archaeological data, archaeological surveys, oral information and scattered archaeological data. It will directly link information sheets with images, videos, documents and 3D models of underwater sites. Thanks to simple navigation on the

digital map, it will finally be possible to access a historical heritage beyond the reach of the potential public;

2. USV exploration and multi-constellation GNSS positioning for underwater survey operations: the project develops a robust and reliable navigation system based on a multi-constellation GNSS (Global Navigation Satellite System) which mainly concerns the floating surface vessel. The system will also benefit from the introduction of inertial measurement units (IMUs) to automatically control and correct the vessel's trajectory during semi-automatic surveys;

3. test strategies for ROV underwater positioning system;

4. proposal of a hybrid visual-acoustic USV-ROV system (sensor fusion): for photogrammetric work, the focus will be on the radiometric calibration of the images and the identification of an adequate acquisition procedure thus defining a tool for planning (pre-survey) and verification (post-survey) of the geometry. Both single shots, spherical images and video recordings are evaluated. The project develops a hybrid visual-acoustic measurement system based on high resolution digital cameras with the integration of acoustic sensors (sonar and multibeam), exploring the potential of an Underwater Positioning System (UPS) based on a GNSS surface system and coded acoustic signals. These additional techniques allow us to increase the information content that can be obtained and, at the same time, reduce measurement errors due to environmental conditions;

5. geomatics data integration and processing (data fusion): the units will work on possible methodologies to optimize the acquisition and processing of high-quality data and achieve high-precision ground control point positioning (GCP).

The high-resolution detection system will be used to map, document and monitor the state of conservation of the underwater heritage represented by the wrecks. The project focuses on the following case studies: Porto Cesareo, Le Cesine. The expected results are as follows:

1. creation of multi-resolution models: the resolution of the model based on the view (multi-resolution) minimizes requirements for GPU compute power, RAM usage and bandwidth while enabling visualization of large models sizes at their full resolution on a wide range of devices;

2. implementation of extended reality and immersive visits: the application of virtual, augmented and mixed reality will provide 3D reconstructions and immersive virtual visits capable of allowing digital enjoyment and narration of the wrecks, making them accessible and usable by a wider audience and not just by a few divers. These reconstructions could be exploited in museums, in visitor centers of Marine Protected Areas (MPAs) and in all regional networks of places of culture. At the same time, extended reality techniques will allow us to respond to divulgation and study needs (not only for specialists but also for a wider audience) with the final aim of creating immersive paths and 3D reconstructions. The applications will be at two main levels: one related to expert users such as divers, researchers and technicians, who are able to view models directly in the underwater environment via mobile devices, and one related to other citizens, able to view the underwater environment on land via mobile devices;

3. scientific publications, good practices and guidelines: this point is based on the divulgation of results through scientific articles in open access journals, annual technical reports, thematic conferences and workshops focusing on distinctive aspects related to the request;

4. benchmark/workshop/summer school: benchmark data will be available for all future investigations and for the scientific community;

5. public involvement

Figure 1 - Location of the case study of Archimedes

2.1.3 The mission of Horizon Europe

ARCHIM3DES fits into the main themes identified by the Horizon Europe (HE) mission area "Healthy oceans, seas, coastal and inland waters". The main objective is to combine research and innovation to acquire new knowledge and enhance the blue economy through the development of technologies and promoting its use in different applications, thus providing tangible impacts from multiple perspectives:

- scientific impact: the project will contribute to the divulgation of underwater knowledge, improving multidisciplinary approaches and scientific collaborations between international institutions. ARCHIM3DES allows to define new procedures, algorithms and methods to solve open problems such as hybrid positioning for underwater navigation and visualization to improve high-resolution underwater surveys. The project aims to develop a high-resolution measurement system suitable for archaeological contexts requiring particular precision, especially regarding wooden naval remains at different depths.
- technological impact: the technological impact of the project consists in obtaining high resolution surveys, both in terms of geometry and colorimetry contents, thanks to the development of hardware and software capable of overcoming the difficulties of the marine environment significantly improving current common practices. The project provides a methodology.
- cultural impact: the project will contribute to creating dynamic national and international networks of underwater studies, characterized by a constant exchange of experiences and information.
- social impact: the strategy will help raise citizens' awareness of their historical heritage and identity, reaching a wider audience. Another aspect concerns the safety of technical operations since a marine drone is used where necessary.
- economic impact: the results provided by the project in terms of new equipment and new standard procedures for the survey and monitoring of archaeological assets and Cultural Heritage in underwater contexts make it possible to provide new commercial opportunities. They include both the work aspect, creating new

opportunities through the implementation of software, and the recreational aspect, trying to bring together a lot of diving tourists.

The project will also contribute to the United Nations Sustainable Development Goals, including:

- gender equality: the project consortium will strive to ensure gender balance and promote the participation of women in the different tasks of the project.
- building resilient infrastructure, promoting inclusive and sustainable industrialization and fostering innovation: the technical and technological improvements supported by ARCHIM3DES will improve industrial sustainability thanks to a smart and more efficient system.
- reducing inequalities: Social innovation focuses on policies and practices for intelligent distribution of tourists and visitors in unconventional and well-known cultural destinations, such as the underwater environment. The greater availability of virtual visit experiences will also improve the accessibility of CH to vulnerable categories, such as the elderly, the disabled or people with health problems.
- conserve and sustainably use the oceans, seas and marine resources for sustainable development: the planned activities expect the development of key tools for the documentation and management of underwater archaeological and cultural assets, supporting the conservation and restoration of wrecks and sites.

2.2 Poseidon

POSEIDON [6] aims to study, develop, and test new methodologies for ultra-high- and beyond ultra-high-resolution mapping and monitoring of Posidonia oceanica (PO) and related meadows and banquettes in the Mediterranean region. This project is driven by recommendations from international organizations such as the European Environmental Directives, the Mediterranean PO Network, the International Partnership for Blue Carbon and the Intergovernmental Oceanographic Commission of UNESCO's Save the Wave project.

The project will adhere to a specific workflow, detailed in the following sections, to enhance current knowledge of PO with a focus on blue carbon conservation. There is growing concern about the conservation status of subtidal ecological systems due to climate change effects and extreme events impacting coastal areas, combined with local anthropogenic disturbances. This has led to an increased demand for high, very-high, and ultra-high-resolution products with precise metric and radiometric details. While many geomatics instruments, techniques, and methods are available for terrestrial studies, the underwater context—covering more than 70% of the Earth—remains a challenge. Using new integrated survey methods and legacy data, PO meadows and banquettes will be mapped to understand their evolution and to identify indicators and trends that can improve our current knowledge. Additionally, the information gathered will be stored and shared through a webGIS and a dedicated app, aimed at preventing damage from activities such as sailing by providing data on PO meadows.

POSEIDON will address mission M2 of the Italian PNRR (Green Revolution and Energetic Transition) in line with component C4 (Landscape and Water Resources Protection), specifically scopes M2C4.1 (Enhancing Forecasting Capacity for Climate Change Effects) and M2C4.3 (Protecting Air Quality and Biodiversity through the Safeguarding of Green Areas, Terrestrial, and Marine Environments). The project will focus on investments I3.2 (Digitalization of Natural Parks) and I3.5 (Restoration and Protection of Seabeds and Marine Habitats). The objectives of POSEIDON align with the PNRR goals for marine habitat restoration and protection, aiming to safeguard and restore at least 20 percent of the seabed and marine habitats in Italian waters. This is essential for meeting the EU targets for biodiversity protection and promoting the sustainability of fishing, tourism, and blue growth. POSEIDON will work towards protecting marine habitats to prevent the loss of Mediterranean ecosystems, boosting tourism and knowledge of the areas studied, and advancing research with new technological tools and methods. The accompanying image illustrates the logical framework of POSEIDON, linking needs and gaps to objectives.

2.2.1 Objectives and actions of the project

As part of the Blue Carbon Initiative, POSEIDON aims to enhance the conservation of seagrass meadows by providing detailed and accurate information on the presence and development of Posidonia oceanica (PO) meadows across various conditions—pristine, degraded, and restored—as well as banquettes. To achieve this, specific marine coastal areas in Sardinia will be selected based on their conservation status: North Sardinia for pristine conditions, Olbia for degraded areas and Villasimius and Golfo Aranci for restoration sites. The project will validate new data acquisition techniques by integrating them with traditional PO data collection methods, including SCUBA visual census for meadow density and canopy structure and biochemical analysis of leaf material for fatty acid profiles.
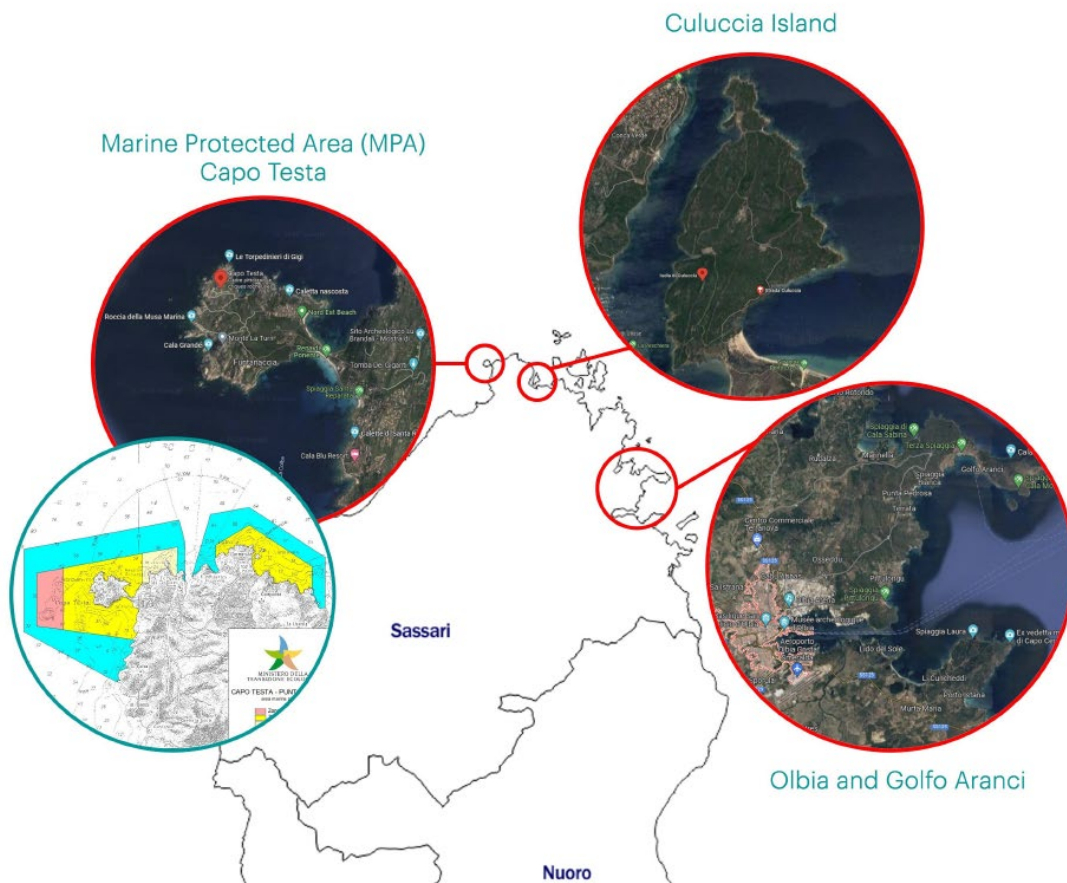
Figure 2 – Location of the case study of Poseidon

The first objective is Supporting the implementation of Environmental European Directives with new digital techniques and methods. The actions are:

- new integrated tools for ultra high resolution (UHR) mapping of maritime ecosystem;
- new methods to improve the contents of multitemporal legacy images acquired by aerial and satellite platforms;
- creation and sharing of a Spatial Data Infrastructure (SDI) to describe PO-beaches system.

The second objective is increasing the efficiency of seagrass monitoring for management and planning. The actions are:

- definition and measurements of environmental spatial indicators and metrics of PO health, ichthyo fauna and seagrass banquettes;
- new instruments/methods for indicators measurement using RGB/Multi/hyperspectral images

The third objective is Developing reproducible good practices in the Mediterranean basin. The actions are:

- New model for representing PO-beach system in local area;
- Transferability and replicability of POSEIDON project;

The fourth objective is disseminating awareness and knowledge of priority habitats and Natura 2000 marine sites in case study area. The actions are:

- the communication plan:
- public awareness and communication of results.

2.3 Workflow

The work shown within this dissertation will display data from both projects. The first part focuses on the theoretical aspects related to the work performed: the regulations, technologies, applied methodologies and physical concepts related to the underwater world.

The second part will show a series of elaborations aimed at understanding the best approach to data acquisition and processing. It will also show what limitations, not only technological but also human, have been faced.

Some of the results obtained were not always satisfactory and consistent with what was expected.

PART A

Theoretical background

Regulation of Underwater Cultural Heritage

Before showing the techniques for surveying architectural heritage, it is necessary to clarify the meaning of Underwater Cultural Heritage since it has undergone changes over time. So it is necessary to understand what it is and how it can be defined. This can also be done through conventions and documentation developed over time, which define not only the strict concept of Underwater Cultural Heritage, but also that of Marine Protected Area, marine environment and coastal landscape.

3.1 International charts and conventions on Underwater Cultural Heritage

Underwater heritage is mentioned for the first time in 1956 in the UNESCO recommendation which contains the international principles for archaeological excavations also applicable in the marine environment[7].

In 1978 a World Heritage List was drawn up [8] in which the main cultural or natural sites were included but all submerged heritage was excluded from it.

Only a few years later, in 1982, was born the first international text [9] closely linked to underwater archaeological sites and historical objects linked to those places, in which it provides that *"shall be preserved or disposed of for the benefit of mankind as a whole, particular regard being paid to the preferential rights of the State or country"* [9]. The first specific reference to submerged Cultural Heritage dates back to the 1990 ICOMOS Charter, which defines archaeological heritage as *"all vestiges of human existence and consists of*

places relating to all manifestations of human activity, abandoned structures, and remains of all kinds (including subterranean and underwater sites), together with all the portable cultural material associated with them." [10]

Attention also shifts to structures and infrastructures (ports, landing places, marine systems). The growing interest in this heritage also ignites the interest of reavers, who are able to reach the sites more easily, thanks to the development of new technologies. For this reason, in 1992, the European Council mobilized and created a European convention on the protection of this heritage, with the idea of creating underwater archaeological parks [11].

A year earlier, in 1991, an international committee for Underwater Cultural Heritage was founded in Australia with the aim of promoting international cooperation in the protection and management of these.

On 8-10th March 2001, an International Conference "*Means for the protection and tourist promotion of marine cultural heritage in the Mediterranean*" was held in Palermo and Syracuse, and the most recent international document was drawn up [12], called the "UNESCO Convention of 2001 on the protection of underwater cultural heritage".

In this latest document, the definition of Underwater Cultural Heritage is proposed (for the first time) as "*any trace of human existence of a cultural, historical or archaeological nature that has been partially or totally underwater, periodically or continuously, for at least 100 years such as: sites, structures, buildings, artefacts and human remains, together with their archaeological and natural context; ships, aircraft, other vehicles or parts thereof, their cargo or other contents, together with their archaeological and natural context and objects of a prehistoric character*" [12].

The Convention establishes the fundamental principles for the protection of Underwater Cultural Heritage, outlining four fundamental principles:

"Obligation to preserve underwater cultural heritage - States parties should preserve underwater cultural heritage and act accordingly. This does not mean that ratifying States must necessarily undertake archaeological excavations; they just need to take measures

according to their capabilities. The Convention encourages science, research and public access.

In situ conservation as a first option - In situ conservation of underwater cultural heritage (i.e. in its original location on the seabed) should be considered as a first option before permitting or undertaking any further activities. The recovery of objects may, however, be authorized for the purpose of making a significant contribution to the protection or knowledge of underwater cultural heritage.

No commercial exploitation - The 2001 Convention states that underwater cultural heritage should not be commercially exploited for trade or speculation and that it should not be irretrievably lost. This regulation complies with the moral principles that already apply to cultural heritage in the area. It should not be understood as an impediment to archaeological research or tourist access.

Training and information sharing - States Parties shall cooperate and exchange information, promote training in underwater archaeology, and promote public awareness of the value and importance of underwater cultural heritage." [13]

After the UNESCO convention on the protection of Underwater Cultural Heritage (2001), the new stage in the current process of re-appropriation of Cultural Heritage as a common good, a "popular" good, is represented by the "Framework" convention on the value of Cultural Heritage for Society [14], adopted by the Commission of Ministers of the Council of Europe on 13th October 2005 in Faro, in force from 1 June 2011 and ratified by Italy on 23 September 2020 (Camera of Deputies). The Convention had the merit of defining an innovative and revolutionary concept of cultural heritage, intended as the set of resources inherited from the past, identified by citizens as a reflection and expression of their continuously evolving values, beliefs, knowledge and traditions. It recognizes the right of the individual citizen and of all humanity to benefit from Cultural Heritage, moderated by the responsibility to respect it. These principles are the basis of the chain of research, conservation, protection, organization, participation and cultural dialogue, which promotes the creation of a sustainable, multicultural, political and economic environment. It is a fact that submerged Cultural Heritage is increasingly required to have a social return beyond the cultural aspect, seeking a positive impact on the economic and social fabric of

41

a community. However the European Union guidelines promote the "Blue Growth" and responsible and sustainable tourism linked to the sea and submerged CH.

Exploring the underwater past is becoming a huge aspect of the leisure industry and "experience economy". This development implies risks and opportunities for protection as not all submerged heritage can be enjoyed through direct access for various reasons: their location, depth and safety/integrity, but also safety and immersion capacity of researchers, citizens, stakeholders and tourists.

20 years after the Sofia Dissertation for the Protection and Management of Underwater Cultural Heritage [15], a summit in Udine drew a picture of the most recent experiences in Italy which led to the creation of the Udine Dissertation for Underwater Archeology [16] which represents the result of a scientific community debate on Underwater Cultural Heritage to try to ensure the developing of public and research interest.

On 8th and 9th September 2022, a first workshop was held to update the Udine Dissertation, to ensure the inclusion of aspects linked to surface waters, such as rivers and lakes.

3.2 Preservation of cultural heritage

Through all the regulations created over time, the conclusion has been reached that submerged assets need not be recovered, on the contrary, sometimes this is not justified, and depends on factors such as the method of sinking, the preservation of the asset, as the operation does not guarantee the maximum preservation of the asset, risking increasing the state of degradation of the asset. It is also necessary to consider the complexity of in situ conservation both in terms of approach and operational workflow. For this reason, it is important to take into consideration innovative technologies for documentation and study even by those who do not have the skills or ability to go underwater.

To explain the current system of protection of the marine environment it is necessary to show the concept of "Marine Protected Areas" [17] to protect the marine environment, the underwater archaeological heritage and the territory. Marine protected areas have been

defined as "Any area of intertidal or subtidal land, together with the overlying waters and associated flora, fauna, historical and cultural features, which has been set aside by legislation to protect some or all of of the closed environment" [18], [19]. With this definition we wanted to protect not only the seabed, but biodiversity, flora and fauna, trying to create an integrated sea-land system.

The areas are divided into 6 different types, depending on their objectives [20]:

Category I – Protected area managed mainly for science or wilderness protection (Strict Nature Reserve/Wilderness Area);

Category II – Protected area managed mainly for ecosystem protection and recreation (National Park);

Category III – Protected area managed mainly for conservation of specific natural features (Natural Monument);

Category IV – Protected area managed mainly for conservation through management intervention (Habitat/Species Management Area);

Category V – Protected area managed mainly for landscape/seascape conservation and recreation (Protected Landscape/Seascape);

Category VI – Protected area managed mainly for the sustainable use of natural ecosystems (Managed Resource Protected Area). (IUCN, 1994)

It is possible to establish some criteria for the restoration of underwater assets, marine areas and coastlines. It is necessary to make an average between socio-economic needs and those of conservation of the heritage. In order to have the best results, it is necessary not only to focus on a single element, but also to consider the relationships between the heritage and the surrounding area.

The study of underwater archaeological sites is closely linked to the history of the coastlines, which is why it is necessary to use different types of data (geological, geomatic, ...) to better understand the development of places over time. The study of the context in which the submerged assets are located can allow us to understand and anticipate future events, sometimes making it possible to create countermeasures for their protection [17].

Chapter 4

Tools and methodologies for underwater surveying

Geomatics is a discipline that deals with the automated management of information relating to the territory. This science developed to respond to the need to analyze data and information collected with different methodologies and tools. The subjects that contribute to Geomatics are many, including IT for the use of specific software for data analysis; cartography since it describes the shape of the surrounding environment through the graphic or numerical representation of more or less large areas using pre-established rules; geodesy as a science that studies the Earth to define the reference surface in its complete form (geoid) and in its simplified form (ellipsoid); the surveying which consists in the direct survey of the territory; photogrammetry which, through the use of photographs, allows the position and shape of the objects affected by the survey to be determined; the laser scanner which allows the identification and measurement of objects through the use of light radiation; satellite positioning which allows the determination of the three-dimensional position of objects, even in movement, in space and time across the entire globe; territorial information systems (SIT) or Geographic Information Systems (GIS) software capable of representing and processing georeferenced data.
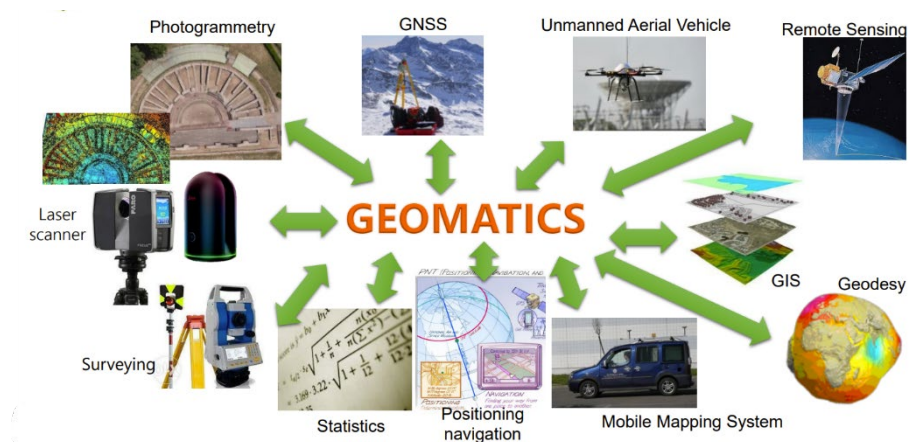
Figure 3 - Disciplines of geomatics

The term Geomatics was first used in the 1970s by the French Ministry of Infrastructure to refer to computer-assisted mapping [21].

Subsequently, a Canadian surveyor used this term to describe the set of technologies and methods used for data acquisition and their processing. The word was "officialized" in 1982, and, a few years later, in 1986 the first chair was awarded for a degree course in Geomatics.

This discipline allows us to understand the territory that surrounds us, allowing us to interact with it through the insertion of artificial infrastructures. Over time it has developed considerably, allowing the information collected to be implemented in increasingly shorter times and with relatively lower costs.

The analysis of the territory takes place according to a well-defined process, which begins with the investigation of the built heritage; the understanding of the object in question and the analysis of the various problems (state of the places, accessibility, vegetation, etc., ...) allows for timely planning of the survey in qualitative and methodological terms. The design of the survey includes the choice of the coordinate system to use in order to be able to georeference the document correctly.

4.1 Characteristics of geomatics

The qualitative characteristics of the metric survey, linked to precision, maximum allowable error and level of detail, constitute a fundamental point to take into consideration.

These elements must be defined previously, based on the client's request and the purpose of the measures. This allows you to make the best choices related to the different types of instruments to be used in order to obtain the necessary data with the desired characteristics in the shortest possible time.

Every data in Geomatics be certified with an estimate of precision/accuracy.

Precision is linked to random errors, and it is the degree of closeness of the observation of a physical quantity relative to their estimated mean. It is considered high when the observations are concentrated close to the estimated mean.

To establish the minimum precision it is necessary to know the representation scale, the formula that relates these elements is the following:

$$s = 0.2mm * n \qquad (1)$$

where:

s is the precision

0.2 is the graphic error

n is the nominal scale

Accuracy, which is quantified with tolerance (T), is linked to systematic errors, and represents the degree of closeness of the observations of a physical quantity compared to the true value (taken as a reference): it is high when the estimated value is very close to the reference value, low in the opposite case. It is linked to the level of detail according to this law:

$$T = 0.4mm * n \qquad (2)$$

Summing up for the main scales of representation we will have:

Type	Scale	Precision (m)	Tolerance (m)	Extension
Medium scale	1:25.000	5	10	state
Mediun scale	1:1000	2	4	region
Large scale	1:5000	1	2	province
Large scale	1:2000	0.4	0.8	municipality
Very large scale	1:1000	0.2	0.4	municipality
Very large scale	1:500	0.1	0.2	Historical center
Architectonic scale	1:200	0.04	0.08	building
Architectonic scale	1:100	0.02	0.04	building
Architectonic scale	1:50	0.01	0.02	Building
Very little scale	1:20	0.004	0.008	Archeological site
Very little scale	1:10	0.002	0.004	Cultural heritage
Very little scale	1:5	0.001	0.002	Cultural heritage

Table 1 - Accuracy and precision

It is therefore possible to state that Geomatics can be applied in multiple fields with notable advantages. This discipline does not have the sole purpose of architectural survey, but it can also be used for the analysis of the territory, infrastructures and more complex scenarios.

Regarding surveys in the marine environment, the complexity of the techniques increases considerably, therefore it is necessary for operators to have complete knowledge of the site (e.g. morphology, depth, currents, visibility and transparency of the water, general conditions of the sea, ...), where one of the fundamental parameters is depth, which impacts on safety issues for operators, but also on the presence of light on the site.

4.2 The technologies for geomatics

Geomatics, over time, has developed using new technologies always based on the same concepts. Nowadays these types of tools and methods are mainly used:

- Total station
- GNSS
- Laser scanner
- Mobile mapping system
- Photogrammetry

Each tool has different functionality and precision and the choice of their use depends on the type of work that needs to be performed.

All these technologies are part of the integrated approach, i.e. technologies, methodologies and disciplines to collect, analyse and manage spatial data more effectively. This approach makes it possible to tackle complex problems related to spatial planning, natural resource management, the environment and urban development. Some key aspects of the integrated approach in geomatics are:

1. data integration: combines data from different sources, such as remote sensing, GIS (geographic information systems), photogrammetry.

2. interdisciplinary collaboration: involves experts from different disciplines, such as engineers, urban planners, ecologists and sociologists, to ensure that solutions are based on diverse and comprehensive knowledge.

3. advanced spatial analysis: uses spatial analysis techniques to identify trends, relationships and patterns in data, supporting informed decisions for planning and resource management.

4. sustainability: focuses on environmental and social sustainability, contributing to decisions that consider the long-term impacts of proposed actions.

5. community participation: promotes the active participation of local communities in the data collection and analysis process, ensuring that the needs and concerns of the population are considered.

6. practical applications: can be applied in various fields, such as land management, urban planning, environmental conservation, water management and climate change monitoring.

4.2.1 Total station

It is a surveying instrument used for indirect survey, i.e. the acquired measurements must be processed to obtain the real dimensions of the object.

It is the evolution of the theodolite which allowed the measurement of only angles with great precision, and of the tacheometer which also allowed distances to be measured using staffs. The total station then acquires data relating to vertical and horizontal angles and measures topographic distances and height differences with the aid of optical prisms or laser readings. Although there are different models, each total station is made up of some common elements:

1. a *base* with 3 lowering screws which allows you to obtain a horizontal surface on which to work;

2. two *levels*, one spherical and one toric, used to approximate the horizontality of the plane;

3. a *telescope* with distance meter to focus on the object of interest and subsequently measure it;

4. an *on-board computer* that allows you to enter and manage project data;

5. an *electronic goniometer,* with two graduated circles for reading the azimuth angle and the zenith angle;

6. a *tripod,* accessory on which to place the total station;

7. a *reflecting prism* mounted on a pole or a second tripod, which allows you to measure the topographic distance and the difference in altitude*.*

The characteristics of this instrument, that can be included among its advantages, are the high angular precision which can even reach 0.5 second of a centesimal degree and the long measurement range (up to 3 km with a prism but which can be overcome with the use of multiple reflective optics). The use of this tool very often involves the development of polygonals which require the efford of at least two operators. Its biggest limitation is the need for intervisibility between the various stations and the visibility of the objects to be measured.

Figure 4 – Example of total station

4.2.2 Global Navigation Satellite System

Global Navigation Satellite System (GNSS) is a system based on the use of signals emitted by satellites.

These are received by an instrument equipped with an antenna and used to calculate the position of a point through a mathematical process of trilateration based on the satelites. To do this, at least four satellites are needed. Nonetheless, the measurement precision would be too low; the acquisition of data transmitted by additional satellites allows improving the positioning of the antenna. To eliminate the biases, the calculation is performed by comparing the data from multiple antennas. This allows you to calculate the difference in coordinates between the various devices and achieve sub-centimeter precision.

GNSS systems return three coordinates: latitude, longitude and altitude; the latter refers to the ellipsoid.
The measurement system consists of an antenna, a receiver and a controller. This tool can be used in several ways; the most used are static mode and RTK (Real Time Kinematic) mode.

The first case is a relative approach, a positioning technique that determines the position of a receiver relative to another known reference receiver. This method is particularly useful for improving the accuracy of measurements, as it reduces the effects of systematic errors. Antennas statically acquire data over long periods, these are processed afterwards. In this mode, millimetre accuracies can be achieved.
With the RTK system it is possible to correct the data in real time and therefore obtain the position of the rover instantly. This methodology allows achieving centimeter precision. Using this mode is very advantageous in terms of time, as it allows you to acquire a lot of data in a relatively short time.

To obtain better results it is necessary to have good visibility of the satellites, therefore the fewer obstacles such as trees, buildings, or other natural or artificial impediments, the greater the precision obtained. The main advantage of the GNSS system is that it can measure multiple points without there being intervisibility between them.

Figure 5 - Example of GNSS antenna

4.2.3 Laser scanner

The laser scanner is an instrument that acquires millions of points autonomously and allows you to carry out extremely detailed surveys. In addition to the coordinates of the single point, informations on reflectance and, optionally, on color are also acquired. The result obtained is a point cloud. In recent years there has been such extensive technological development that has allowed the use of laser scanners not only on earth, but also in the sky.

To carry out the survey, the instrument uses a laser composed of a single frequency, which is extremely directional even at long distances.

These tools are divided into main distinct categories, based on the technology used. The first is based on flight time: the instrument emits a light pulse that hits the survey object; the time between the starting pulse and the returning pulse determines the distance. The second is based on the phase difference; in this case the time taken by the impulse to return is not calculated, but the phase difference between the wave emanating and the wave that returns after impacting the object is.

There are a multitude of laser scanners, each with its own characteristics, so it is very important to choose the right tool for the result you want to achieve. Laser scanners are high-performance tools, but require equally high investments.

Figure 6 – Example of laser scanner

4.2.4 Mobile mapping system

Mobile mapping systems are the combination of multiple navigation and measurement technologies on a common mobile platform. They collect data quickly and comprehensively [22]. This method is based on three main components: the positioning system, the photographic cameras and the lidar; furthermore, two different detection methods can be distinguished, called IMU (differential inertial measurement unit) and SLAM (simultaneous localization and mapping).

The first is based on the principle according to which, within a reference system, it is possible to determine the movement of a body by observing the external forces acting on it.

Inertial measurements are subject to the laws of classical Newtonian mechanics:

- a body remains in its resting state until disturbed by external forces;
- the force is proportional to the change in velocity (acceleration) over time and therefore to the change in position. The ability to measure force allows us to know the acceleration and therefore the change in position;
- it is necessary to know the direction of the accelerometers during body movement.

The second is an area mapping process, which keeps track of the position of the device within the survey area. This mechanism consists of measuring large areas in a shorter time, compared to other methods, since it uses mobile robots, drones or vehicles. This methodology can be used for both internal and external environments.

There are various types of SLAMs, including:

- the visual one: calculates the position and orientation of the device with respect to the environment and uses visual input derived from a camera to map its surroundings.
- the lidar one: this type uses a laser sensor to generate the 3D map of the environment. This approach is accurate and rapid and has a wide range of applications.

These tools, as already mentioned, can be very fast, but with the disadvantage of not being cheap.

Figure 7 - Examples of Slam instruments

4.2.5 Photogrammetry

Photogrammetry is an indirect survey technique that allows you to determine, from a metric and radiometric point of view, the shape and position of objects starting from at least two different frames. To analyze objects from photography to the real environment, the position of the points within the image must be determined through geometric relationships that project 3D into 2D. To do this, the presence of multiple frames with different grip points is necessary.

The photogrammetric survey has different phases:

- data acquisition: operation which concerns the taking of images with appropriate means and techniques;
- orientation: activities are carried out that allow the reconstruction of the shape and size of the object;

- restitution: allows you to carry out measurements on the reconstructed object. A model is created, from which different information can be extrapolated in different forms.

Photogrammetry has various advantages, in particular the possibility of determining various characteristics of the analyzed object without having direct contact with it. Another favorable aspect is the relatively low cost compared to other measuring instruments. The use of drones is not always permitted as sometimes authorizations to fly or licenses are required to use certain tools.

There are various types of photogrammetry:
- architectural: mainly used for architectural survey, whose distance between sensor and object does not exceed 10 meters;
- satellite: composed mainly of meteorological satellites;
- UAV and aerial: remotely piloted aircraft are part of the category or instruments capable of taking photographs are placed on aircraft flying over the position of the territory concerned;

Photogrammetry has multiple applications ranging from cartography, both large and small scale, to archaeology, for mapping or researching historical finds.

To determine the positions of the object in the real environment using the positions of the corresponding points on the photograph, it is necessary to define geometric relationships.

Each point on the three-dimensional object corresponds to a homologous point on the plane. The grip centre O is a point on the camera lens, while the distance of O from the plane is called the principal distance. The main distance is kept fixed and can be considered equal to the focal distance (without considering distortions) [23].
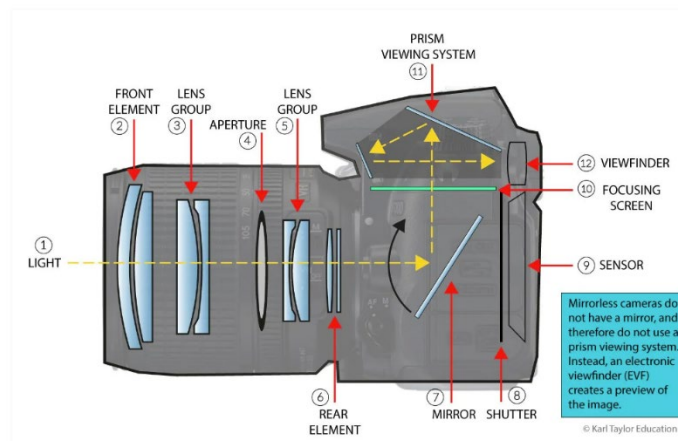
Figure 8 - How a camera lens works

The photogrammetric process can be divided into 4 main phases: data acquisition, internal and external orientation of images, collimation of control points and the creation of metric products.

The survey groups together all the operations relating to the taking of images carried out with drones or cameras using appropriate techniques. During this phase it is important to remember the principles on which photogrammetry is based; any point on the object corresponds to an image point on the projection plane. The necessary condition, in order to establish any point of the object in three-dimensional space starting from the coordinates of the image, is to have at least two frames of the same point, with different points of view. The movements between one image and another take place with rectilinear trajectories along which photographs will be taken which, for a successful survey, must have a transversal overlap of 60% and a longitudinal overlap of 80%. Images taken along the same straight trajectory are called swipes.

Orientation is the preliminary operation that allows you to determine the parameters that allow you to position the grip centers, in order to reconstruct the shape and dimensions of the object. It is both internal and external, the which is still distinguished as relative and absolute. Relative orientation allows you to create a three-dimensional model on an arbitrary scale, while absolute orientation allows you to obtain a model at the desired scale, but to do this, support points are necessary. It allows you to accurately establish the

56

internal and external orientation parameters. The internal orientation allows you to identify the position of the center of perspective of the camera and the plane in which the image is formed, eliminating the effects of distortions caused by the lens used for taking the image.

After acquiring the data, processing begins using software that uses algorithms based on "structure from motion" [23]. This process consists of creating 3D models starting from two-dimensional frames. It is divided into three phases:

1. Features point detection
2. Matching point
3. Bundle block adjustment

The first part consists of identifying characteristic points called 'descriptors', i.e. established high-contrast points, which are indispensable for the search for homologous points.
Once the descriptors have been identified for each image, characteristic points belonging to different frames are connected. In the last step, the collinearity equations are solved to return the binding points from 2D space to 3D space.
To obtain the equations, it is necessary to estimate the position of the cameras and their orientation in each image. With this step, the rotation matrix R and the translation matrix T can be derived.

R is a 3x3 matrix representing a linear transformation that rotates points from one coordinate system to another without changing distances or angles, thus preserving the geometric structure.

$$R = \begin{bmatrix} r_{11} & r_{12} & r_{13} \\ r_{21} & r_{22} & r_{23} \\ r_{31} & r_{32} & r_{33} \end{bmatrix} \tag{3}$$

T a 3x1 vector indicating the translation of the camera along the x,y and z axes.

$$T = \begin{bmatrix} T_x \\ T_y \\ T_z \end{bmatrix} \tag{4}$$

57

The intrinsic matrix K is also calculated and is a 3x3 matrix.

$$K = \begin{pmatrix} f_x & 0 & c_x \\ 0 & f_y & c_y \\ 0 & 0 & 1 \end{pmatrix} \tag{5}$$

Combining the three matrices results in the projection matrix M, which projects a 3D point onto the 2D coordinates of the image.

$$M = K[R|T] \tag{6}$$

Once the 3D points and the position and orientation of the cameras are known, we can formulate the collinearity equations, which describe the projection of the 3D points onto the image plane. The collinearity equations are fundamental in photogrammetry and are based on the assumption that point P(x,y,z), the centre of the camera and the point projected onto the image lie on the same line (hence the term 'collinearity')

$$x = (c_x + dx) - f \frac{r_{11}(X - X_0) + r_{21}(Y - Y_0) + r_{31}(Z - Z_0)}{r_{13}(X - X_0) + r_{23}(Y - Y_0) + r_{33}(Z - Z_0)}$$
$$y = (c_y + dy) - f \frac{r_{12}(X - X_0) + r_{22}(Y - Y_0) + r_{32}(Z - Z_0)}{r_{13}(X - X_0) + r_{23}(Y - Y_0) + r_{33}(Z - Z_0)} \tag{7}$$

where there are:

- Parameters of internal orientation:

    f = principal distance

    c_x, c_y = coordinates of principal point

- Parameters of external orientation:

    X_0, Y_0, Z_0 = absolute coordinates of the gripping centre

    r_{ij} = rotation parameters

Underwater photogrammetry has become one of the most convenient methods for studying and building underwater architectural assets. The acquisition and processing phases are similar to the aerial ones, paying attention to problems related to the marine

world. This methodology, although widely applied, still faces some problems related to georeferencing of images, data acquisition, because sometimes the images are not fully in focus since the operator is unable to stop to acquire the frame, so it is possible also the presence of drag problems. Another problem that can be encountered during the acquisition phase is related to the cleaning of the site, or to the movement of the seabed which causes the lifting of sand and particles which partially obscure the object under examination. A fundamental aspect is that of radiometry strictly linked to depth.

4.3 Camera calibration

Camera calibration is a process used for preserving metric consistency and having reliable metric data. This process is carried out not only for traditional photogrammetry, but also - and especially - for underwater photogrammetry. With this calibration it is possible to describe geometric distortions on acquired images. These distortions are due to the lenses (material and shape), the optics used in surveying, and the characteristics of the camera.

This procedure allows you to obtain the camera's own parameters, which describe the internal orientation and distortion of the lens (f, c_x, c_y, k_1, k_2, k_3, k_4, b_1, b_2, p_1, p_2). Using these parameters in processing allows you to obtain images as close to reality as possible, making the survey more precise [23].

The parameters represent:
- f - Focal length;
- c_x, c_y - Principal point coordinates, i.e., coordinates of lens optical axis intersection with sensor plane;
- b_1, b_2 - Affinity and non-orthogonality (skew) coefficients;
- k_1, k_2, k_3, k_4 - Radial distortion coefficients;
- p_1, p_2 - Tangential distortion coefficients.

These parameters are derived from Brown's 10-parameter model, which introduces differentials within the collinearity equations to consider deformations [24] (equation (7)).

Applying Brown's model:

$$dx = (x - c_x)\left[k_1 r^2 + k_2 r^4 + k_3 r^6\right] + p_1\left[r^2 + 2(x - c_x)^2\right] + p_2(x - c_x)(y - c_y) + b_1(x - c_x) + b_2(y - c_y)$$
$$dy = (y - c_y)\left[k_1 r^2 + k_2 r^4 + k_3 r^6\right] + p_2\left[r^2 + 2(y - c_y)^2\right] + 2p_1(x - c_x)(y - c_y)$$

(8)

Here there is a display of the 10 values that allow us to evaluate distortions:

$$r = \sqrt{(x - c_x)^2 + (y - c_y)^2}$$ radial distance

f, c_x, c_y

k_1, k_2, k_3 radial distortion coefficient

p_1, p_2 tangential distortion coefficient

b_1, b_2 affine and shear distortion coefficient

There are several methods including computer vision algorithms that allow for self-calibration of the camera [25]. In some cases, it is possible to pre-calibrate the camera. This process is performed in a controlled environment using checkerboard or dot calibration panels. The parameters obtained from this process can be used as initial data during the data processing phase.

4.3.1 Radial distortion

The main component of distortion is radial distortion, as it becomes more pronounced with moving away from the main point. It is also prevalent over the other distortions. This distortion influences both ξ that η [26].

There are two main types of radial distortion:
- Barrel Distortion:
  - Straight lines appear as curves moving away from the centre of the image, creating a 'barrel' effect.
  - Common in wide-angle lenses.

- Pincushion Distortion (Pincushion Distortion):

- Straight lines appear as curves approaching the centre of the image, creating a 'cushion' effect.
- Common in telephoto lenses
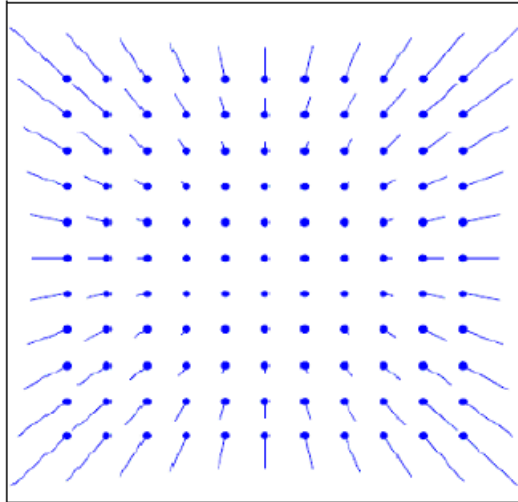
Figure 9 - Effects of radial distortion

The calculation of these coefficients is given to us by:

$$\Delta x_{rad} = \frac{x - c_x}{r} \Delta r \qquad\qquad \Delta y_{rad} = \frac{y - c_y}{r} \Delta r \qquad\qquad (9)$$

The distortion curve is depicted:
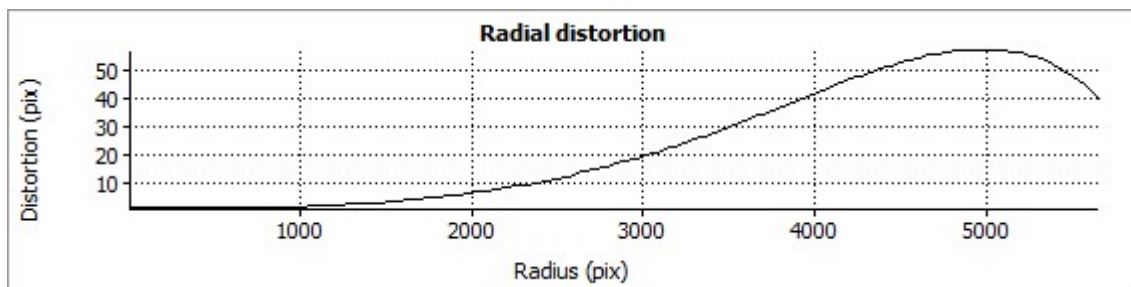
Figure 10 - Radial distortion curve

4.3.2 Tangential distortion

This type of distortion is due to imperfect centring of the lenses that make up the lens [26]. Tangential distortion causes a displacement of image points in a tangential direction, along a path that is tangent to an imaginary circle centered on the optical axis of the lens. This

displacement is not radial (not going towards or away from the centre), but follows a direction tangential to the center of the lens.
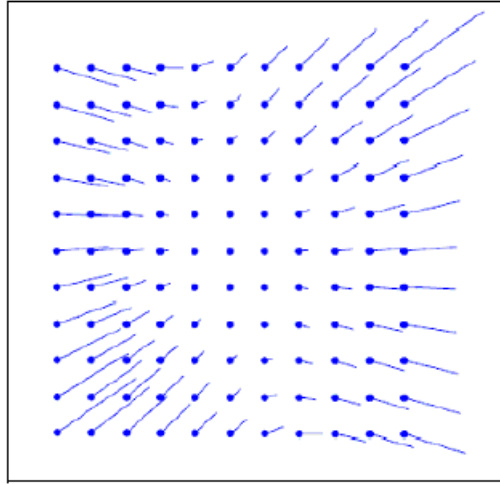
Figure 11 - Effects of tangential distortion

Similarly, the calculation for tangential distortion has been defined:

$$\Delta x_{tan} = p_1(r^2 + 2(x - c_x)^2) + 2p_2(x - c_x)(y - c_y)$$
$$\Delta y_{tan} = p_2(r^2 + 2(y - c_y)^2) + 2p_1(x - c_x)(y - c_y)$$

(10)

The distortion curve is depicted:
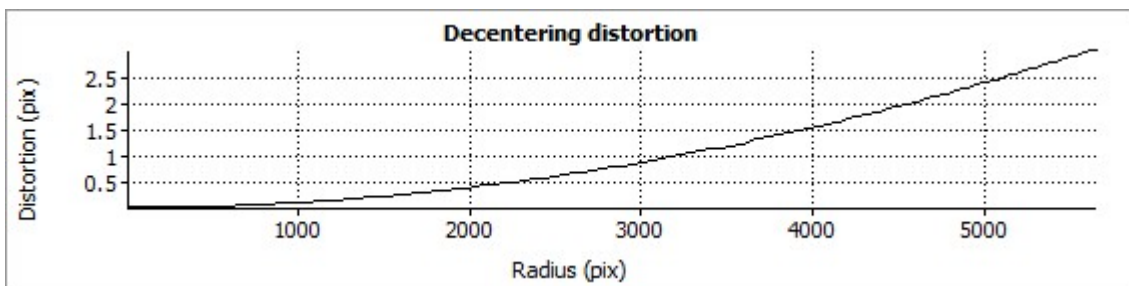
Figure 12 - Tangential distortion curve

62

4.3.3 Affine and shear distortion

Affine and shear distortion are two types of geometric distortions that can affect the accuracy of three-dimensional images and reconstructions. They are less common than radial and tangential distortions, but can still have a significant impact on the accuracy of photogrammetric data.

Affine distortion alters the proportions and angles of images, but preserves the collinearity of straight lines. In other words, the straight lines in the real world remain straight lines in the distorted image, but the scales along the different axes may change, and the angles between the lines may be altered.

Shear distortion is a related type of distortion that occurs when straight lines in the real world change to oblique parallel lines in the image. This type of distortion manifests itself as a parallel shift of image points along a specific axis. Shear distortion can be caused by lens mounting errors, sensor deformations or camera tilts relative to the image plane [27].

This type of distortion can be represented
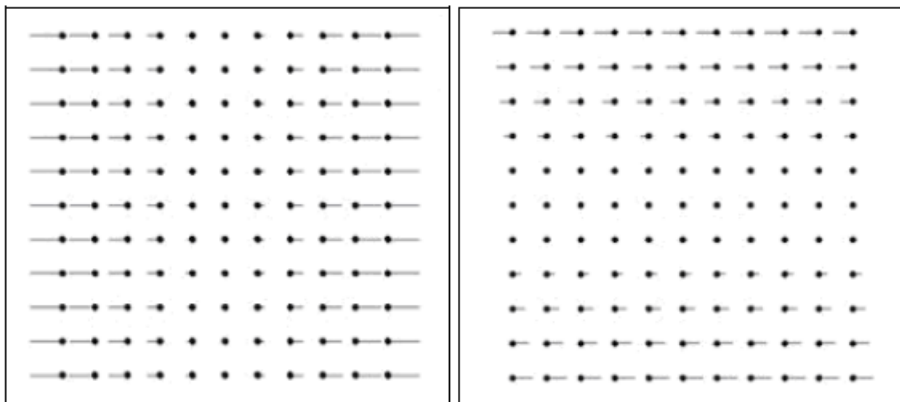
Figure 13 - Effects of affine (left) and shear distortion (right)

This type of distortion only affects x [26]:

$$\overline{\Delta x}_{aff+tag} = b_1 x + b_2 y$$
$$\overline{\Delta y}_{aff+tag} = 0$$

(11)

4.4 Important physical aspects in underwater photogrammetry

As far as underwater photogrammetry is concerned, it is necessary to consider certain physical aspects that greatly influence the processing of the data. It is essential to understand these aspects and how they affect both the data acquisition and processing phases. It is possible to counteract these effects both in the field and afterwards.

Data acquisition techniques vary considerably depending on depth, in shallow water you can use cameras and sonar, beyond 50 metres you can use sonar and beyond 500 metres you can use satellite gravimetry [28].
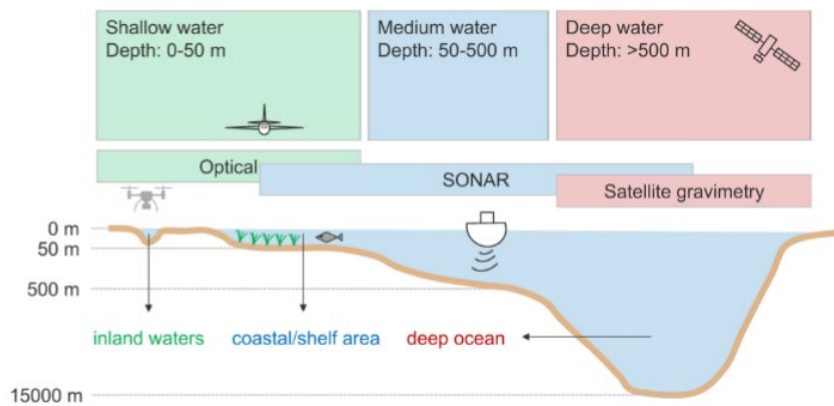
Figure 14 – Types of instruments according to depth (Mandlburger, 2022)

Considering that the physical characteristics of water differ considerably from those of air, greater attention must be paid to [28]:
- refraction;
- high electrical conductivity;

- water's own weight, which affects the mechanical stress applied to the instruments;
- wavelength selective light absorption, scattering and backscattering;
- dynamic environment.

4.4.1 Refraction

The first phenomenon we are talking about is refraction. It occurs when light passes through two media that have a different refractive index, in this case air and seawater.

This happens because there is a change in the speed of propagation. This phenomenon can be described using Snell's law [29]:
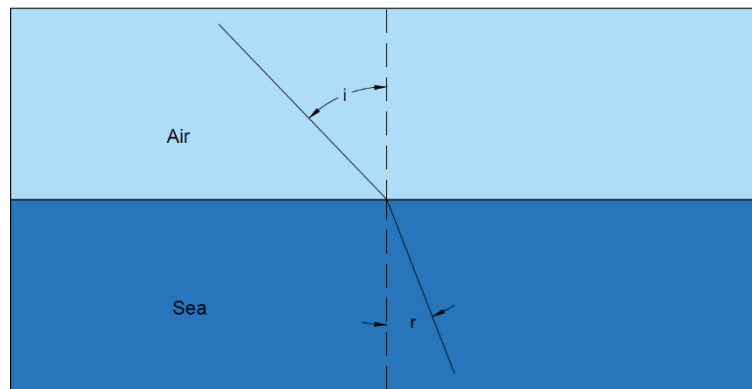
Figure 15 – Snell's law

$$\frac{sen\hat{i}}{sen\hat{r}} = \frac{n_2}{n_1}$$

(12)

where:

$\hat{i}$ = angle of air incidence

n_1 = air refraction index (about 1.0003)

$\hat{r}$ = angle of water incidence

n_2 = water refraction index (from 1.3330 to 1.3721 [30])

It is necessary to consider approximations due to random phenomena caused by wave motion that can cause the angle of incidence to change [17].

4.4.2 Selective absorption

One of the most important phenomena to take into account is selective absorption. It is closely related to depth as water absorbs part of the light in an uneven manner. There is a progressive colour degradation starting with the colour red and ending with the colour blue [31]. This is why submerged objects appear blue/green in colour.

Sunlight is electromagnetic radiation with wavelengths ranging from tens of metres to a trillionth of a metre. The earth's surface is reached by wavelengths between 400 and 700 nanometres. This spectrum is continuous, i.e. it has no white spaces between the different wavelengths[32].

The properties that control the attenuation of light depend on dispersion and absorption [33]. These light attenuation coefficients develop exponentially as a function of the depth travelled [34]. Only 1% of the light reaching the water surface reaches a depth of 100 metres [35].

The first components to disappear are those of the red color as early as 5 meters deep. Orange disappears from 7.5 meters, yellow between 10and 14 meters, and green at about 21 meters [36].
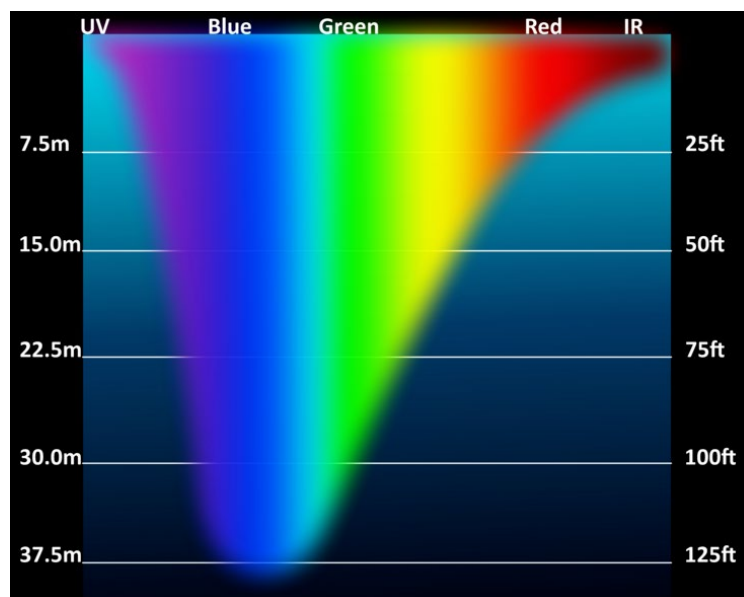
Figure 16 - Light penetration spectrum in water

Some digital cameras allow white balancing during data acquisition, making the images more real, but do not allow the red band to be recreated, which is lost with depth. It is also possible to counteract this problem by using a light source, either a flash or special equipment that illuminates the desired object.

The best choice is to use not only lighting equipment, but also other auxiliary equipment that allows radiometric correction in the data processing phase.

4.4.3 Diffusion and backscatter

The last aspect to be analysed is the presence of suspended materials in the water. The main problem in the areas examined is the presence of sand, algae or other small disturbing elements, which can make the photo less sharp.

Backscatter is a diffuse reflection due to scattered light from a flash or other illuminating elements. This can cause spots to appear in photographs[17].

To reduce this phenomenon as much as possible, it is necessary to be as close as possible to the object.

4.4.4 Ports for underwater photogrammetry

Through the use of additional instrumentation used with the camera, the distortions created on the images can be reduced.

Ports can be of different types and characteristics.

The flat port can be made of polycarbonate or glass. has a reduction in the field of view (limited to 96°) and the focal length undergoes an increase.

The object appears closer to the camera by a factor of about 25 percent. This port creates radial distortions. One advantage of it is cost; it is an inexpensive instrument.

The spherical dome port is a concentric lens that acts as an additional optical element; it varies neither the field of view nor the focal length. This port focuses a lot on the virtual

image you create, so you have to pay attention to focus. One disadvantage of it is the high cost.
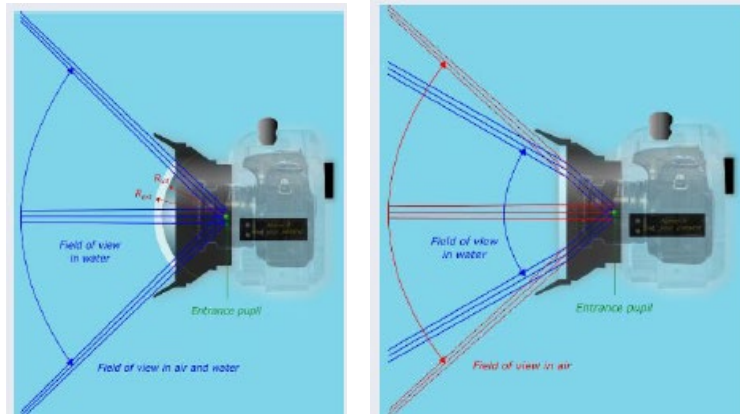
Figure 17 - Comparison of spherical dome (left) and flat port (right)

It was possible to observe that the use of the corrected port significantly decreases distortions [37]. The use of the flat dome greatly increases the presence of radial distortions on the image. It is possible to notice them since there is a division of the color bands on the sides of the image.
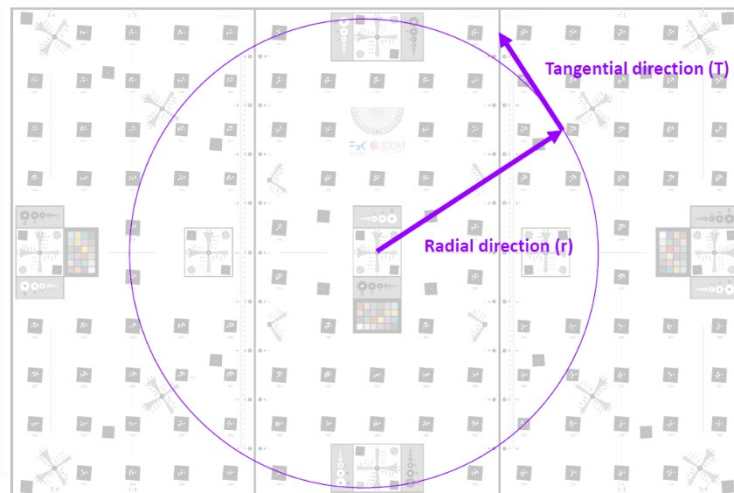
Figure 18 - Distortion distribution in the marine environment[37]

F. Menna's work shows how using a different port affects the acquired image. Assuming surveying, a submerged point P is projected on the sensor at the distance $\bar{r}_i$ from the principal point following the blue path according to Snell's law [38].

In air the red collinearity line would instead directly link the object point P with its image projection on the sensor, differing by the quantity $\overline{\Delta r}$ with respect to the submersed case. $\overline{\Delta r}$ is function of the distance $\overline{Z}$
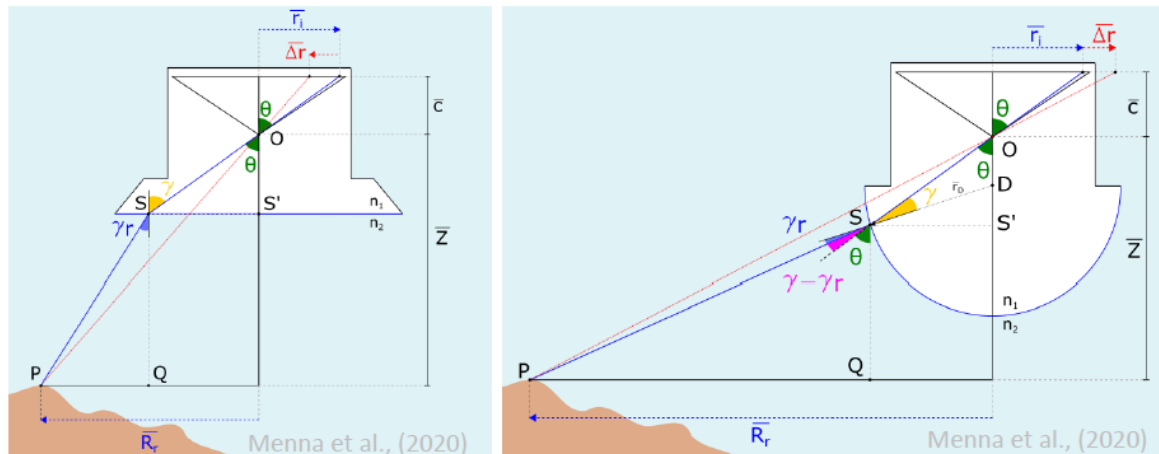
Figure 19 – Functioning of the flat port and spherical dome port [38]

4.5 Problems in underwater photogrammetry for operators

Underwater surveying presents more difficulties than terrestrial surveying and this affects the success of the data acquisition. Among the 'classic' difficulties that can be encountered during a survey, one must take into account increased psychological pressure, due to the need to keep tank pressure under control, the psycho-physical condition of the workmate and all possible problems related to equipment and diving. There must be at least two professionals diving and they must have not only their diving licence, but also the necessary equipment (wetsuit, tanks, regulator, etc., ...).

In addition, the depth at which the site is located must be taken into account, since at different depths there are different difficulties. For deeper sites, the most critical issues are the lack of lighting and the time available. The latter is reduced because it is necessary to manage the oxygen supply for both the 'active' part of the survey and the 'passive' part, i.e. the operator's descent and ascent, which beyond a certain depth includes compression stops of at least three minutes. One must consider that every 10 meters of depth the pressure increases by 1 atmosphere, this creates considerable stress on the body if the

pressure increase is not managed properly. There are several diving patents divided into categories: for depths beyond 18 metres, it is not sufficient an open licence, but an higher level one.

For shallow depths, the issue is not oxygen management, as it is easier to ascend and change cylinders, but the ability to stay buoyant. It is not possible for the operator to stay too close to the bottom, to avoid moving targets or muddying the water, nor to stay too far away from the artefact.

In both cases, it is important to consider that the operator has a physical limit. When conducting repetitive dives, i.e. several dives in a short interval of time, it is crucial to take precautions to avoid risks related to nitrogen build-up in body tissue, which can increase the risk of developing decompression sickness (MSD). After each dive, it is important to give the body time to eliminate the nitrogen accumulated during the dive. This process occurs mainly through breathing during the period between dives, called the surface interval. It can be monitored using dive computers or SSI tables [39]. The time for each dive depends on the oxygen supply, psycho-physical conditions, time and depth of previous dives. For this reason, it is essential to plan the survey as precisely as possible.

Another fact that greatly influences survey is the presence of underwater currents. They can be weak or strong, but in both cases they affect the operator, because swimming against the current requires physical exertion that causes a greater use of oxygen. In addition, the current affects not only the submerged operator, but also the surface, causing the boat on which the operators rest to move, which may require additional physical effort to reach it.
In addition, sea currents can cause water clouding, reducing visibility.

Some of these issues can be managed through training and experience gained over time.

4.6 Mathematical and Nerf method for color correction

On the topic of colour correction there are numerous studies, some based on the physics of the problem, others based on NeRFs (Neural Radiance Fields). Both methods have strengths and some critical issues.

4.6.1 Mathematical method

The work of Bianco [36] aims to correct images using a mathematical method in an attempt to mimic the performance of the visual field. Assumptions are made:

- the environment is uniformly illuminated by a coloured light source (constant light intensity);
- no degradation effects (noise or blurring of the image) are considered;
- surfaces are Lambertian, i.e. they reflect light equally in all directions.

The colour space, *lαβ,* used for the analysis is lab proposed by Ruderman [40]. The coordinate "*l*" represents the achromatic luminance component, ranging from 0 (black colour) to 100 (white colour). The components of "*α*" and "*β*" give information on hue and saturation and can have positive or negative values [41].

In order to perform this colour correction, it is firstly necessary to correct the RGB image from non-linearity (gamma correction) to obtain linear RBG coordinates.

The standard formula for the correction is [42]:

$$C_{linear} = \begin{cases} \dfrac{C_{gamma}}{12.92} & C_{gamma} \leq 0.04045 \\ \left(\dfrac{C_{gamma} + 0.055}{1.055} \right)^{2.4} & C_{gamma} > 0.04045 \end{cases} \qquad (13)$$

where:

- C_{gamma} is the RGB gamma-corrected value (between 1 and 0);

- numerical values are for conversion from non-linear to linear;
- 12.92: This is the normalisation factor used for the lowest values of C_{gamma} derived from the definition of the sRGB gamma curve;
- 0.04045: This is the threshold value separating linear and non-linear behaviour in gamma correction;
- 0.055 and 1.055: These are constants derived from the sRGB transfer function and are needed to correctly transform non-linear colours into linear values.

The C_{gamma} values must be normalised between 1 and 0 where 0 represents black (no light) and 1 represents white (maximum light intensity).

Next, it is necessary to convert to XYZ tristimulus values. This conversion is achieved by multiplying the linear RGB coordinates $f_i(m, n)$ with $T_{xyz,ij}$ matrix [36]:

$$x_j(m,n) = T_{xyz,ij} f_i(m,n) \qquad (14)$$

where:

- $x_j(m,n)$: j-channel colour values for a given pixel with co-ordinates (m,n);
- $f_i(m,n)$: colour values of channel i for a given pixel with co-ordinates (m,n);
- $T_{xyz,ij}$: colour space transformation matrix.

Subsequently, the conversion into LMS space (Long, Medium, Short) [36]:

$$l_j(m,n) = T_{lms,ij} f_i(m,n) \qquad (15)$$

where:

- $l_j(m,n)$: j-channel colour values for a given pixel with co-ordinates (m,n);
- $f_i(m,n)$: colour values of channel i for a given pixel with co-ordinates (m,n);
- $T_{xyz,ij}$: colour space transformation matrix.

The last conversion is into logarithmic space[36]:

$$l_{\log}(m,n) = \log l_i(m,n) \qquad (16)$$

At the end of the processing, the image vector coordinates are obtained in lab space, described as [36]:

$$l_{1\alpha\beta}(m,n) = T_{pca,ij} l_{\log,i}(m,n) \qquad (17)$$

- Luminance: achromatic α *(r+g+b)*
- α: yellow-blu α *(r+g-b)*
- *ß: red-green α (r-g)*

To sum up, it is necessary to increase the contrast of the images, balance the colour components and lengthen the luminance component.

The obtained results [36] show that the best ones are achieved with the assumption of a grey world and homogeneous ambient illumination and they are only acceptable if the acquisition is close and in shallow water

4.6.2 NeRFs method

The NeRFs method is based on neural radiance research, i.e. the use of artificial intelligence to represent complex three-dimensional scenes.

This technology is based on volumetric rendering that takes into account the points sampled along the 3D rays [43].

One problem with this technology is that it has always considered imaging in a clear environment, which is extremely rare in the marine world due to floating particles and vegetation. To try to solve this, a new model has been introduced that takes into account the diffusion media [44].

This can be done by using different parameters for the media and the object for density and colour.

The new version of this model makes it possible to improve several issues that might be present, such as blurring, low brightness, super-resolution and denoising. It is possible to make a comparison between the first algorithm and the one implemented[44]:

- The original NeRF equation:

$$\hat{C}(r) = \sum_{i=1}^{N} T_i (1 - \exp(-\delta_i \sigma_i)) c_i$$

$$T = \exp(-\sum_{i=1}^{N} \delta_i \sigma_i)$$

(18)

- new Sea-thru equation:

UW image = Clear image x attenuation + backscatter

$$\hat{C}(r) = \sum_{i=1}^{N} \hat{C_i^{obj}}(r) + \sum_{i=1}^{N} \hat{C_i^{med}}(r)$$

$$\hat{C_i^{obj}} = T_i^{obj} \exp(-\sigma^{attn} s_i)(1 - \exp(-\sigma_i^{obj} \delta_i)) c_i^{obj}$$

$$\hat{C_i^{med}} = T_i^{obj} \exp(-\sigma^{bs} s_i)(1 - \exp(-\sigma_i^{bs} \delta_i)) c_i^{med}$$

(19)

where:

- c^{med}: color of medium, uniform per light ray
- σ^{bs}: backscatter coefficient
- σ^{attn}: attenuation coefficient

However, this model has some limitations. It does not take into account multiple scattering, artificial lighting that may be used in the environment, and possible flickers.
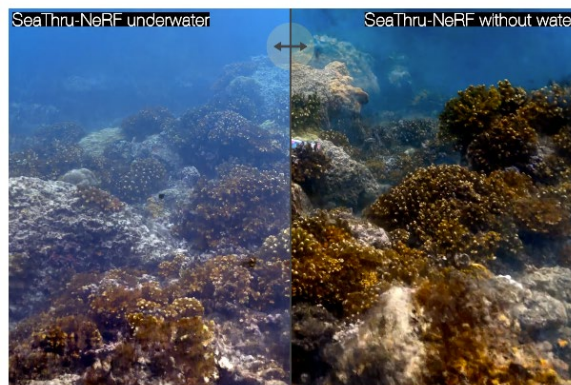
Figure 20 - NERF-processed images compared

PART B

Case studies

Chapter 5

Single camera calibration

In this section of the dissertation, the calibration of individual cameras will be shown. Subsequently, we will also deal with the case of stereo cameras.

The analysis was carried out on two datasets. The first was acquired at Coluccia Island with a total of 191 images. A selection was made, discarding those where the calibration panel was not clearly visible or excessive blurring was present. The total number of images used is 159. For this analysis, the circular targets and the checkerboard were chosen for calibration, because the two of them were really close to each other. The camera with which the images were taken is an Olympus TG-6 with the following specifications:

Figure 21 – Olympus TG-6

Type of camera	compact
Image sensor	1/2.33-inch CMOS
Camera lens	x4 optical zoom
Focal length	4.5-18.0 mm
Focusing method	Autofocus with contrast detection
Image size in pixels	4000x3000
ISO sensitivity	100-12800

Table 2 - Technical Specifications Olympus TG-6

The second dataset was acquired in Porto Cesareo with a total of 74 images, but in this case the checkerboard was chosen. The camera with which the images were taken is a Sony ILX-LR1 with a Sony 17MM F/4 lens mounted on it with the following technical specifications:

Figure 22 – Sony ILX-LR1

Type of camera	Digital camera with interchangeable lens
Camera lens	x4 optical zoom
Focal length	17 mm
Focusing method	Autofocus with contrast detection
Image size in pixels	6000x4000
ISO sensitivity	100-32000

Table 3 - Technical Specifications Sony ILX-LR1

For both datasets, a two-pronged approach was used. The first one is to use the original data, the second one is to split the images into the different RGB channels. Using this method, it is possible to work out which is the best to minimise camera distortions.

5.1 Application on matlab

5.1.1 Application on original dataset of Coluccia island

The first application shown uses data from the Olympus camera. The used code allows to employ the app within the 'Camera calibration' software. Not all the images in the dataset were used, only 13 images were selected. This choice was made because the software had problems recognising the checkerboard as some images were very similar, so they were removed manually. In addition, one part of it was discarded directly by the software.
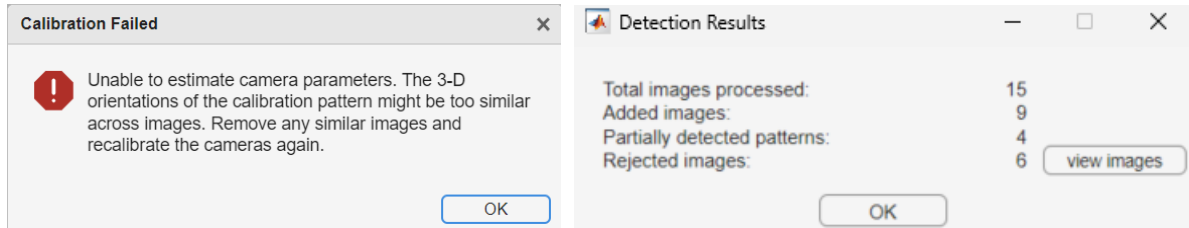
Figure 23 - Errors obtained by Matlab when importing and calibrating images

Once the import is completed, it is necessary to set the right parameters for the calibration panel, i.e. the type, in this case the checkerboard, and the size of the squares, in this case 10 cm.
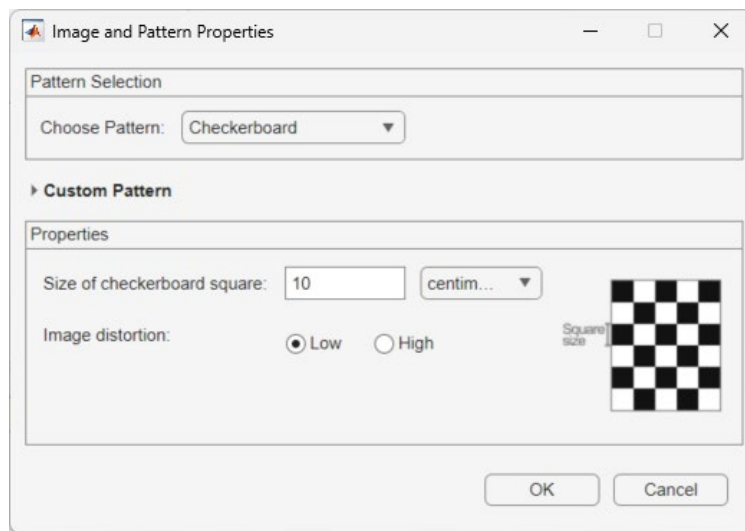
Figure 24 – Image and pattern properties

In the camera calibration tool, it is possible to choose which parameters to calculate. For a more precise analysis, all parameters (f, c_x, c_y, k_1, k_2, k_3, k_4, b_1, b_2, p_1, p_2) were calculated.

After calibration, the work done can be exported in the form of a script. This application processes the data until the undistorted image is obtained, without an export or the possibility of using parameters outside Matlab.
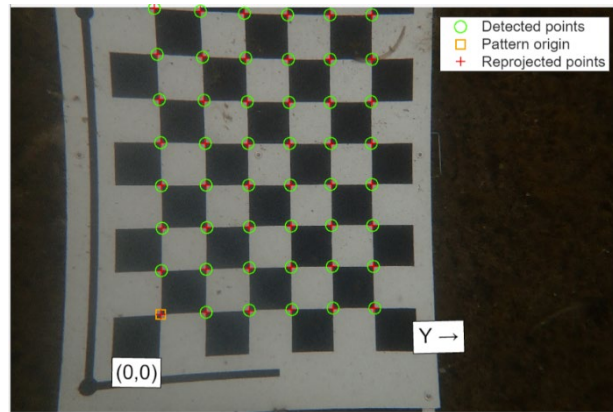
Figure 25 – Image with reprojected points

For this reason, the code was implemented (appendix A) by adding a part in which the calculation of the camera's intrinsic values, the export of the inverse matrix, the export of the undistorted image and the creation of a text file that can be used in future steps on photogrammetry software is carried out.

From the results obtained, it can be seen that the average error is 0.89 pixels:
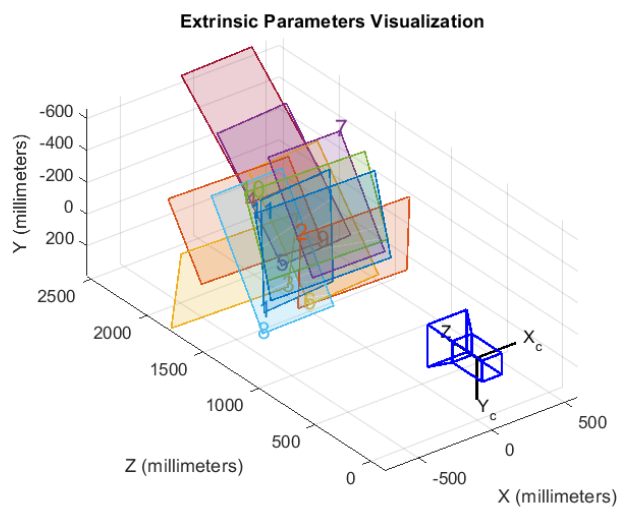
Figure 26 - Extrinsic parameters visualization original dataset
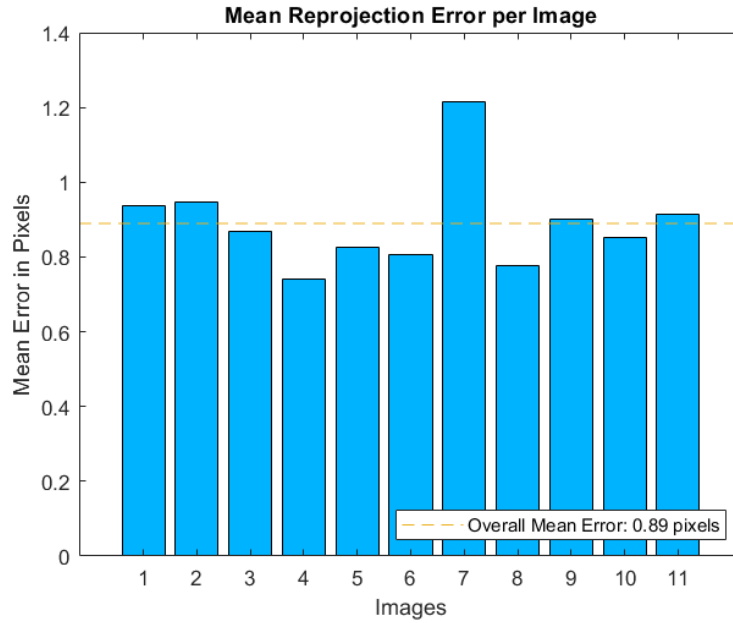
Figure 27 - Mean reprojection visualization original dataset

It can be seen that for the purposes of the final calibration, two more images were removed in order to get the average error as low as possible. Being below the pixel, we can consider this acceptable.

Summarising the parameters of focal length, principal point and distortion coefficients:

f_x [pixel]	3954.0
f_y [pixel]	3954.0
c_x [pixel]	2005.0
c_y [pixel]	1322.6
k_1	0.421165
k_2	0.051302
k_3	0.380903
p_1	-0.003311
p_2	0.002496
b_1, b_2	-1.172463

Table 4 - Distortion coefficients of the original dataset

5.1.2 Application on division of the dataset into channels of Coluccia island

The second application differs from the first in the type of input data. This division into channels is done to better study radial distortions, which as explained in Section 4.4.4 are more present with the absence of a spherical dome. By dividing the channels, one wants to understand whether there is an improvement in the final result compared to those where the RGB division is not applied. The division can be done either with commercial software, such as Matlab or Photoshop, or with free software. The next steps were the same as those described in Chapter 7.1.1 with the difference that three different scripts were created, one for each colour.

The results obtained are different for each channel, which extrinsic parameters and average error expressed in pixels will be shown in the following diagrams.

For the blue channel we obtained:
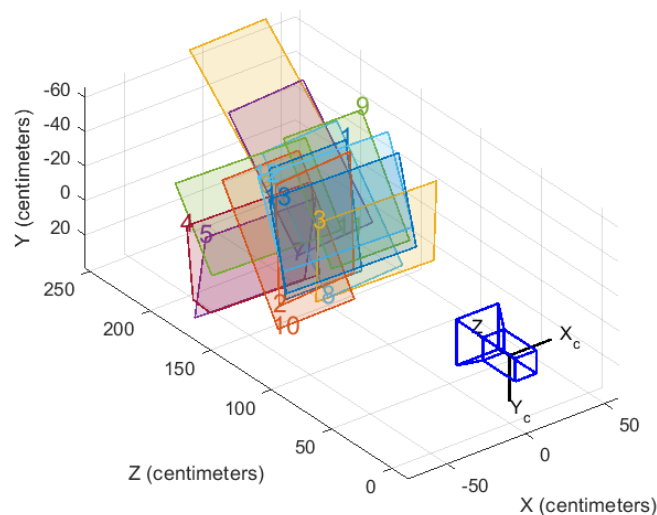
Figure 28 – Extrinsic parameters visualization blue channel
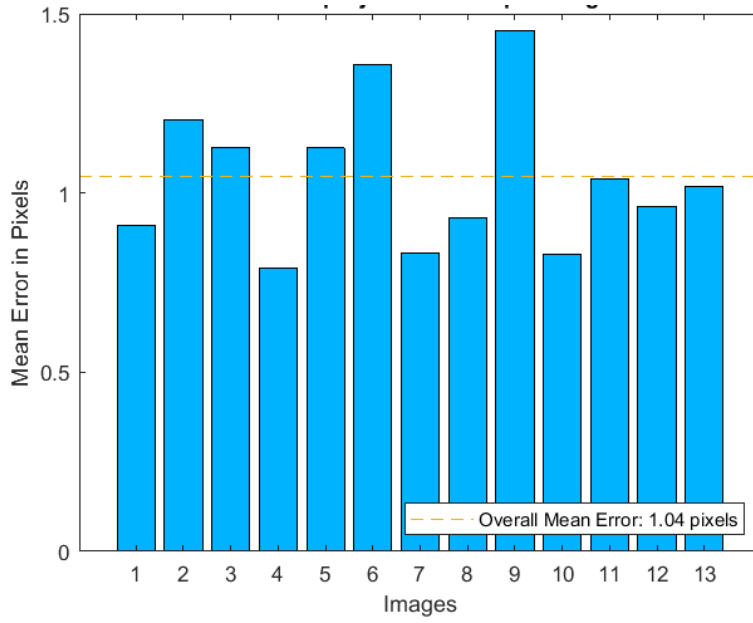
Figure 29 – Mean reprojection visualization blue channel

For the red channel we obtain:
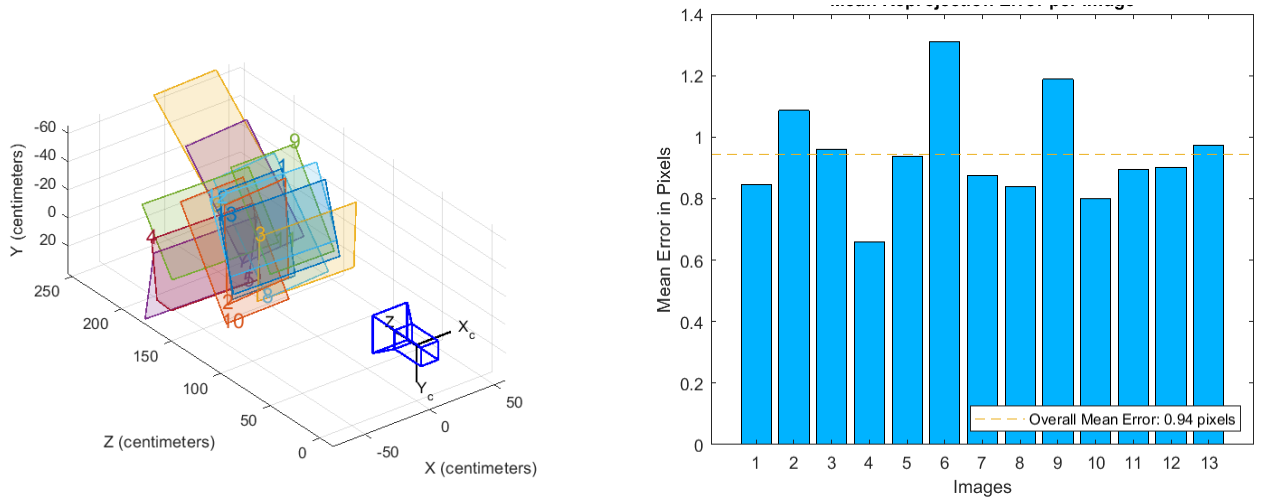
Figure 30 – Extrinsic parameters and mean reprojection visualization red channel

For the green channel we obtain:
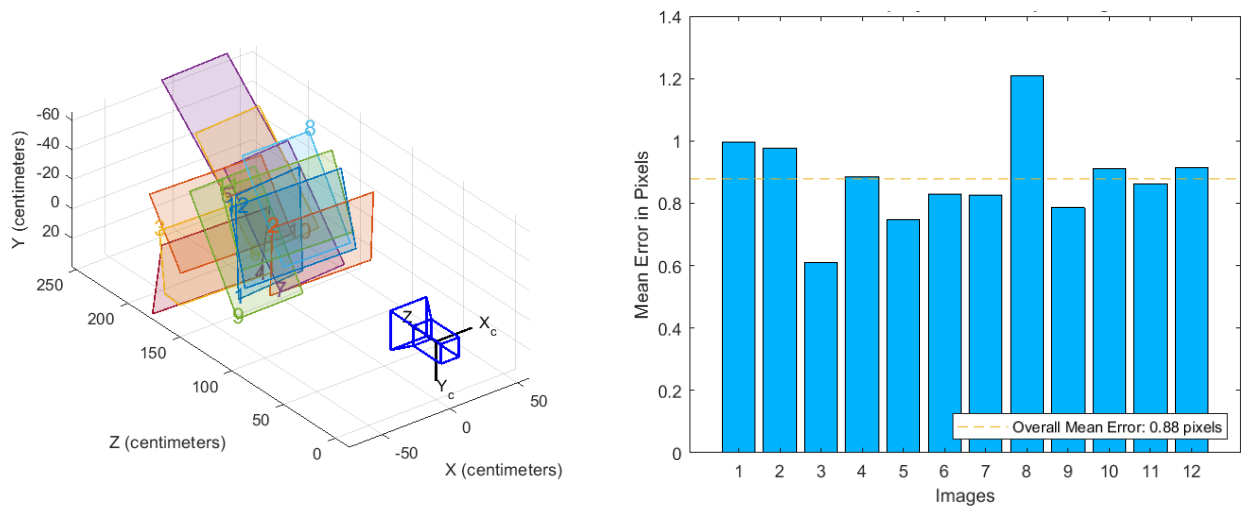
Figure 31 – Extrinsic parameters and mean reprojection visualization green channel

From the results obtained, it can be seen that the channel with the lowest average error is the green channel (0.88 pixels), while the one with the largest mean error is the blue channel (1.04 pixels).

Thanks to the script we used within Matlab, it is possible to compare the results of the camera calibrations. We summarise the output in the following table

	Blue channel	Red channel	Green channel
f_x [pixel]	3960.5	3960.0	3960.3
f_y [pixel]	3960.1	3960.1	3960.9
c_x [pixel]	2008.6	2010.3	2006.2
c_y [pixel]	1323.7	1317.7	1322.1
k_1	0.415566	0.410638	0.422291
k_2	0.151986	0.125623	0.080361
k_3	0.187264	0.146429	0.285044
p_1	-0.003163	-0.003886	-0.003019
p_2	0.003564	0.003594	0.002776
b_1	-1.198961	-1.832586	-1.593999
b_2	-1.198961	-1.832586	-1.593999

Table 5 - Distortion coefficients for each channel

After obtaining all the data divided by channels, it is necessary to merge them to obtain the final result. The union of the data can be done in several ways. It is possible to use graphical software such as photoshop or, as in our case, to make the process faster, autonomous and with a low risk of making mistakes, to apply a script on matlab (Appendix B).

The first part of the script consists of inserting the images to be analysed through their path. Three different folders have been created, once for each colour in order to make the procedures clearer and faster. It is possible that the image has more than one dimension, so only the first channel needs to be extracted, because it is the one that contains all the information we need. Once all these steps have been completed, it is possible to combine the RGB channels into a single image, within which the distortions will no longer be present.

5.1.3 Coluccia island results compared

The reason why this two-pronged approach was chosen was to find out whether analysing individual channels reduces distortions to a greater extent, having an improvement when calibrating the camera.

First of all, it can be seen that in this image dataset, the presence of distortions within the images is evident.
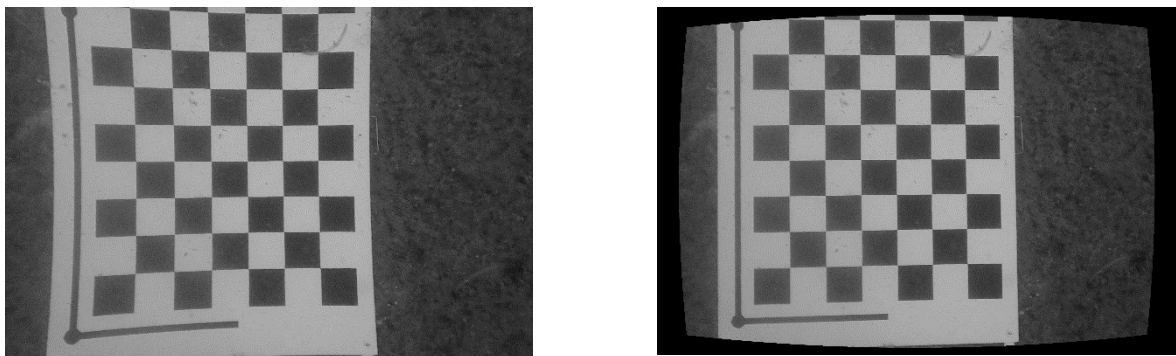
Figure 32 – Comparison of original (left) and undistorted image (right)

85

In the figure 27, you can see the original image on the left and the undistorted image on the right, after the channels have been merged. The corrected image appears to have sharper edges, reducing the effect created by the blue and red colours typical of radial distortion.

Analysing this result, we can consider ourselves satisfied as the final image is better in terms of geometric correction.
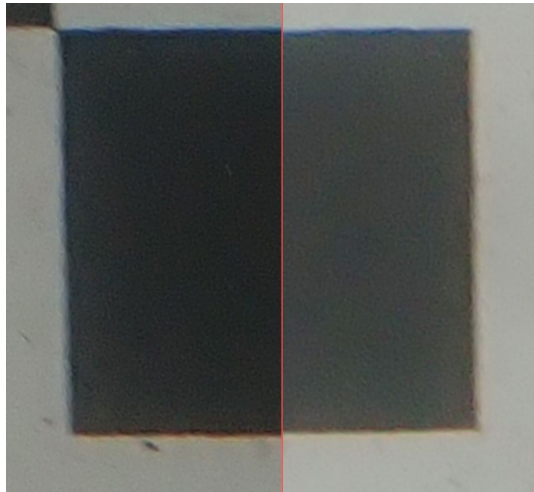
Figure 33 – Comparison of original and undistorted image with all the channels

The most important comparison is the image analysed by dividing the RBG channels or keeping it together.
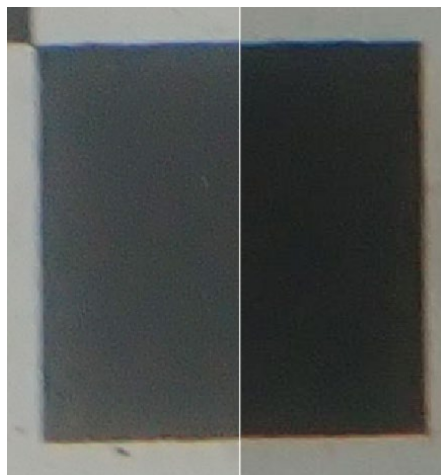
Figure 34 - Comparison of undistorted image with all the channels (left) and undistorted original photo (right)

In the image analysed using RGB division It is possible to see the reduction of red and blue components, which indicates a better calibration.

For a better comparison and to be sure of the above, the ENVI software was used and two spectral profiles were extracted on the x-axis.

The first is that of the original data:
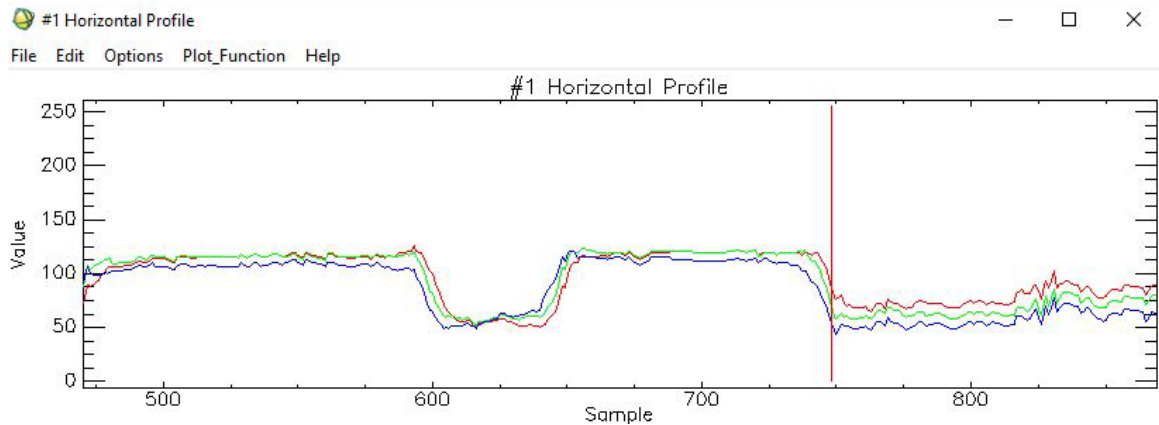
Figure 35 - Profile on the x-axis of the original undistorted image

The second represents the merged data after processing the individual RGB channels:
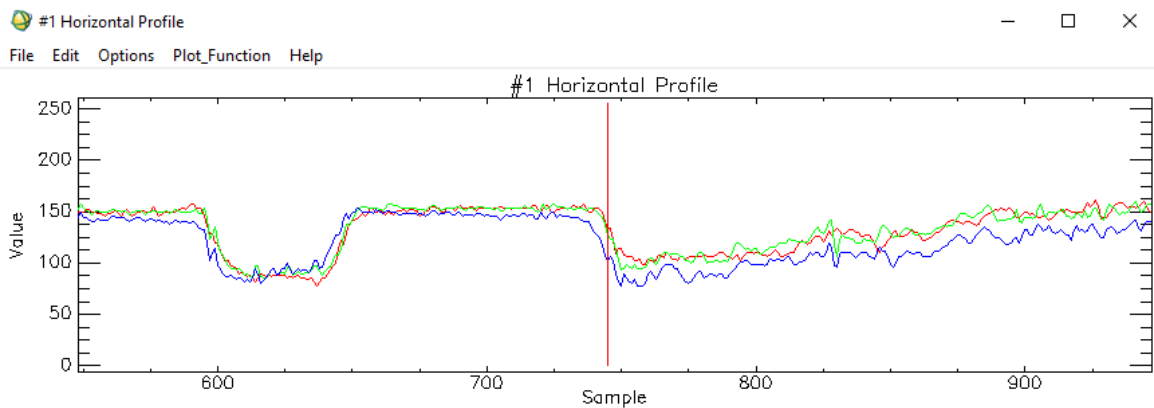
Figure 36 - Profile on the x-axis of the undistorted image of the of the analysis of RGB channels

The x-axis (sample) represents the position along the horizontal line (expressed in pixels) on the image, from which the spectral values were extracted. Y-axis (Value) represents the signal intensity for each spectral band, in radiometric units. Each lines each represent the RGB channel.

87

The profile was drawn at a significant point in the image, i.e. at the edges, as the presence of distortions increases significantly.

In both profiles it is possible to notice a deviation between the various channels, but in the second profile the overlap is better, there is a more uniform and coordinated behaviour between the RGB channels.

It can therefore be concluded that the analysis of the individual channels and their subsequent merging leads to a better result than the analysis of the original data.

5.1.4 Application on original dataset of Porto Cesareo

For this third application, data acquired from the camera Sony ILX-LR1 with a Sony 17MM F/4 was used. All 70 images were imported, of which 57 were used for calibration. The others were partly discarded by the software and partly deleted manually as they were considered incorrect, because the calibration panel was not recognised correctly.

As the previous applications, all parameters (f, c_x, c_y, k_1, k_2, k_3, k_4, b_1, b_2, p_1, p_2) were calculated. The script used is the same (Appendix A).

The results obtained are:
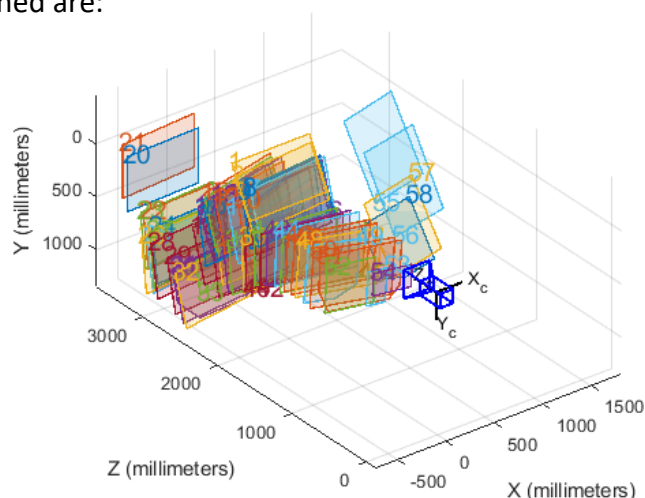
Figure 37 - Extrinsic parameters visualization original dataset
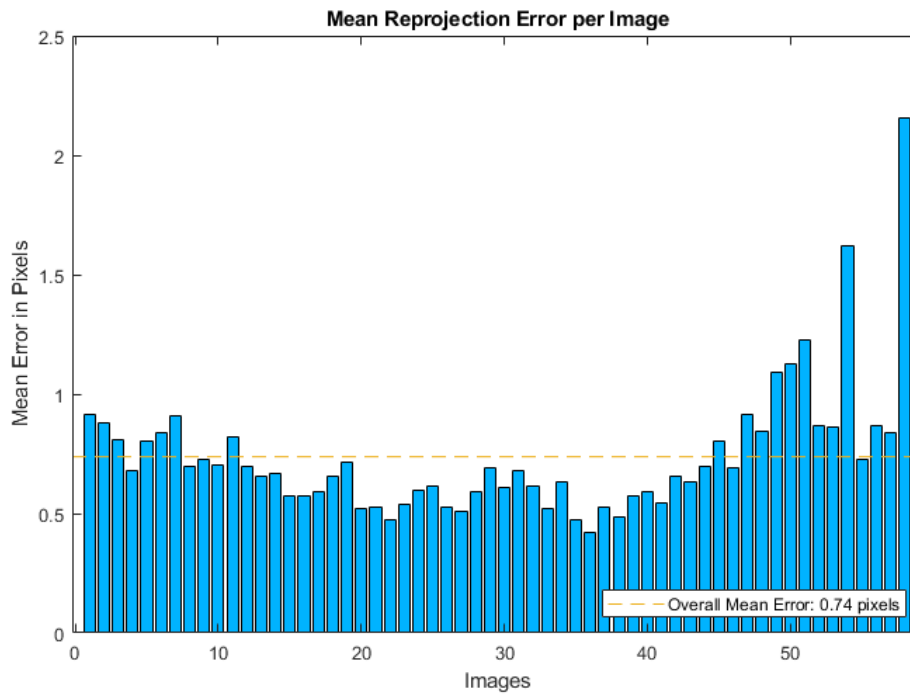
Figure 38 - Mean reprojection visualization original dataset

Since the average error is equal to 0.74 pixels, thus below the pixel, we can consider a good camera calibration.

Summarising the parameters of focal length, principal point and distortion coefficients are:

f_x [pixel]	5270.3
f_y [pixel]	5275.2
c_x [pixel]	4719.2
c_y [pixel]	3140.9
k_1	-0.006724
k_2	-0.017874
k_3	0.022570
p_1	-0.001930
p_2	-0.000292
b_1, b_2	-0.539921

Table 6 - Distortion coefficients of the original dataset

5.1.5 Application on division of the dataset into channels of Porto Cesareo

For this last application on Matlab, the same procedure was performed as in Chapter 5.1.2. At this stage, many more photos were discarded than in the previous approach, especially for the blue channel.

We have 27 calibrated images for the blue channel, 48 for the red channel and 36 for the green channel. The results that were obtained for each channel are:

For the blue channel:
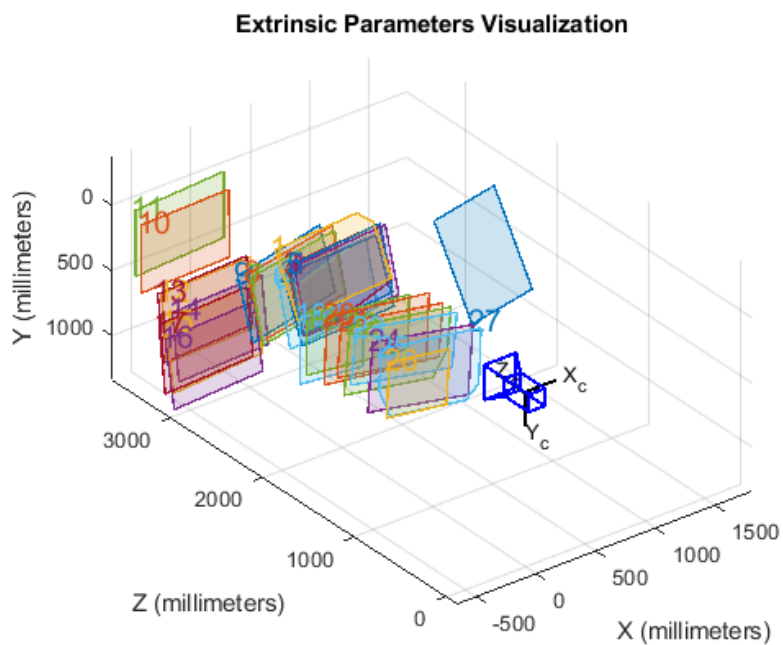
Figure 39 - Extrinsic parameters visualization blue channel
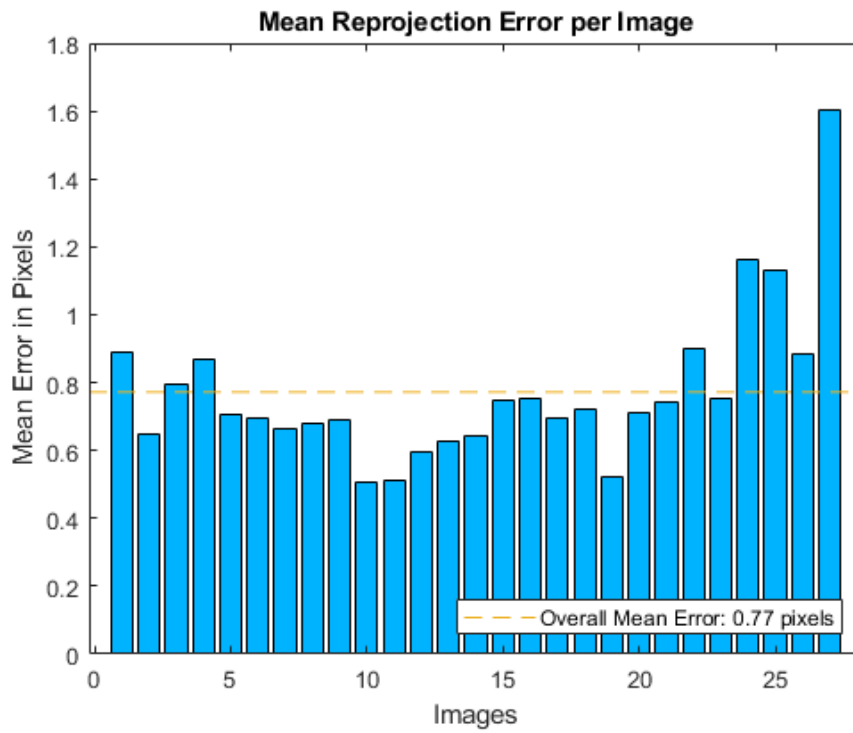
Figure 40 - Mean reprojection visualization blue channel
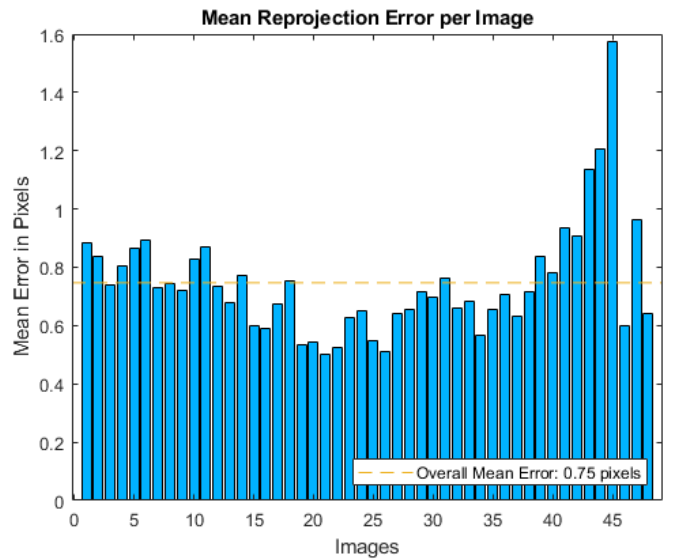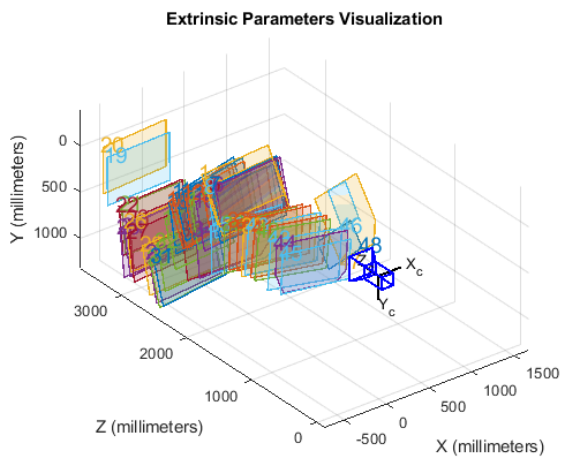
For the red channel:

Figure 41 - Extrinsic parameters and mean reprojection visualization red channel

For the green channel:
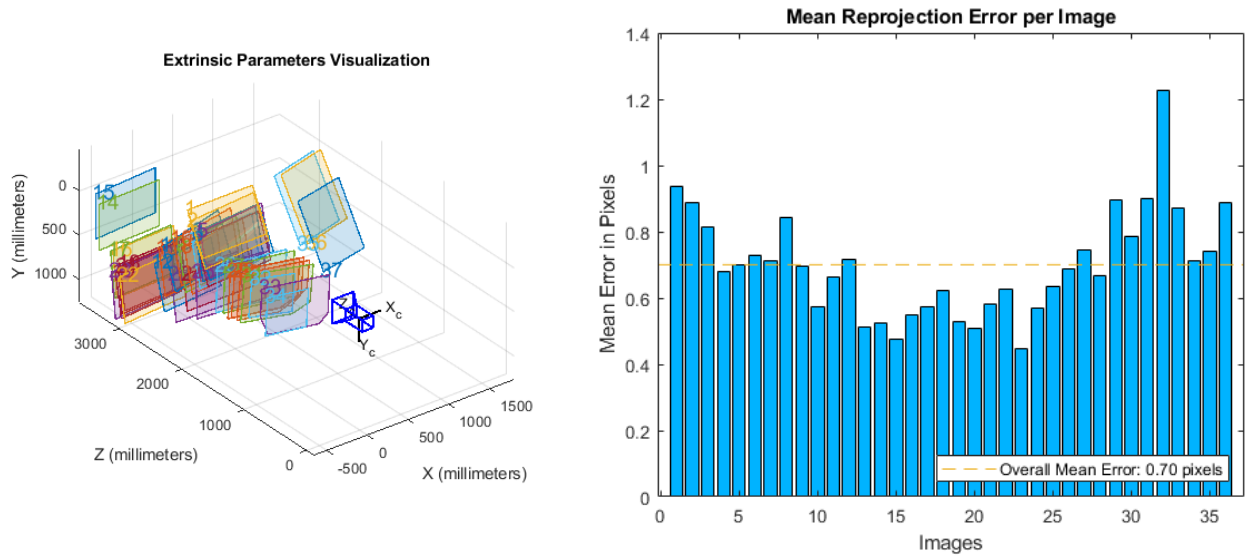
Figure 42 - Extrinsic parameters and mean reprojection visualization green channel

From the results obtained, it can be seen that the channel with the lowest average error is the green channel (0.70 pixels) while the one with the largest error is the blue channel (0.77pixels).

Thanks to the script we used within Matlab, it is possible to compare the results of the camera calibrations. We summarise the output in the following table:

	Blue channel	Red channel	Green channel
f_x [pixel]	5297.3	5286.0	3960.3
f_y [pixel]	5302.0	5290.0	3960.9
c_x [pixel]	4723.7	4720.0	2006.2
c_y [pixel]	3133.1	3132.5	1322.1
k_1	-0.003869	-0.008549	0.422291
k_2	-0.024314	-0.022288	0.080361
k_3	0.027779	0.025155	0.285044
p_1	-0.001791	-0.001822	-0.003019
p_2	-0.000661	-0.000411	0.002776
b_1	0.896018	-0.121878	-1.593999
b_2	0.896018	-0.121878	-1.593999

Table 7 - Distortion coefficients for each channel

92

After calibration, as with the previous approach, the channels had to be merged again, using a script (Appendix B), but first the images that were not present in the calibration for all three RGB channels were removed. After calibration, as with the previous approach, the channels must be merged again, using a script (Appendix B).

5.1.6 Porto cesareo results compared

In the previous dataset, we could see that analysing the images divided by RGB channel leads to an improvement in the final result. We will now see if this is also the case with another camera.

The first thing to note, however, is the considerable difference between the images acquired at Coluccia Island and Porto Cesareo in terms of the presence of distortion.

The second dataset shows much less radial distortion thanks to the use of a dome, which greatly helps the camera to reduce it.
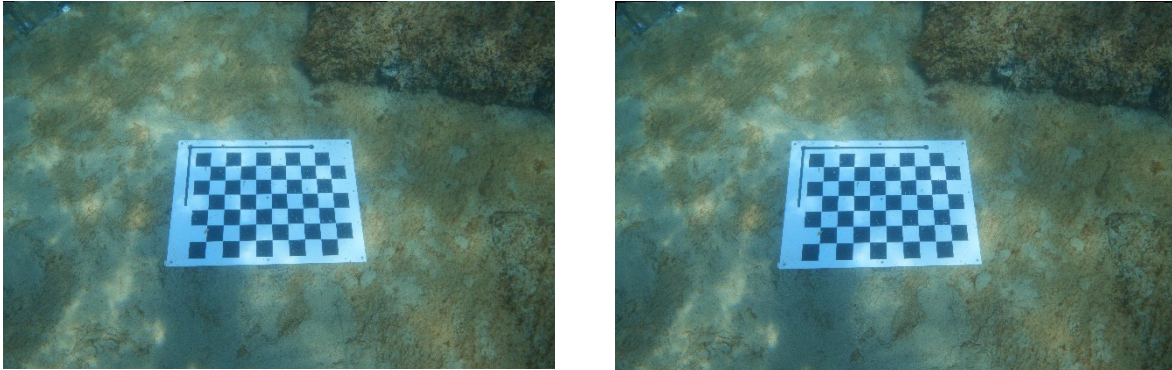
Figure 43 - Comparison of original (left) and undistorted image (right)

In fact, it is possible to notice a small correction of the images only at the edges, which is much less pronounced than in the first dataset analysed.

Figure 44 - Focus on the image to show distortion

In figure 43, you can see the original image on the left and the original image on the right after the channels have been merged. In contrast to the previous analysis, here no improvement can be seen with the naked eye, this is because, as explained above, the presence of a dome significantly reduces distortions.
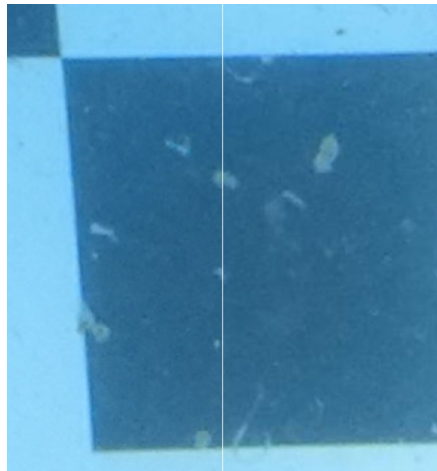
Figure 45 - Comparison of original (left) and undistorted image with all the channels (right)

The same lack of major differences can be seen between the original undistorted image and the image processed by channel division.

Figure 46 - Comparison of undistorted original photo (left) and undistorted image with all the channels (right)

In this case, as opposed to the previous case where it was already possible to see the diversity of the result, a more in-depth analysis is required to try and work out which approach is best. To do this, Envi was used again, creating spectral profiles on the x-axis.

The first is that of the original data:
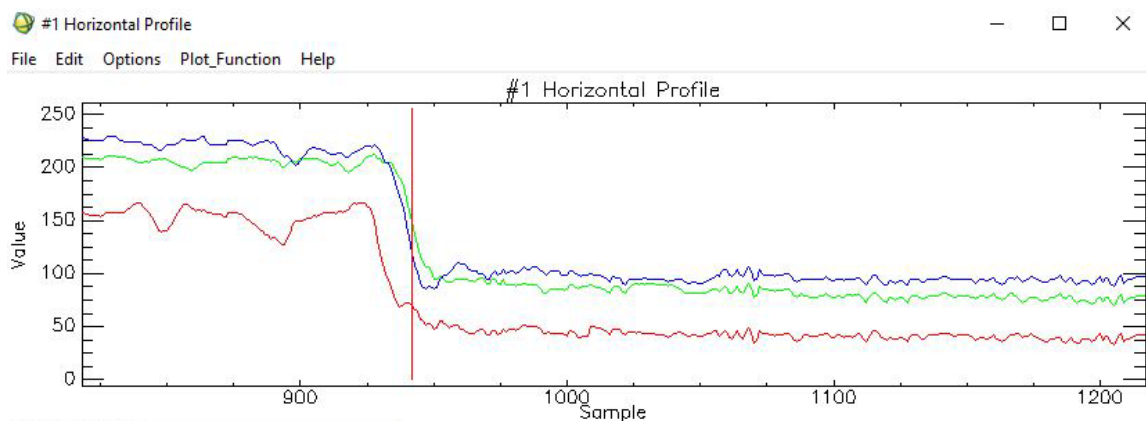
Figure 47 - Profile on the x-axis of the original undistorted image

The second of the merged data after processing the individual RGB channels:
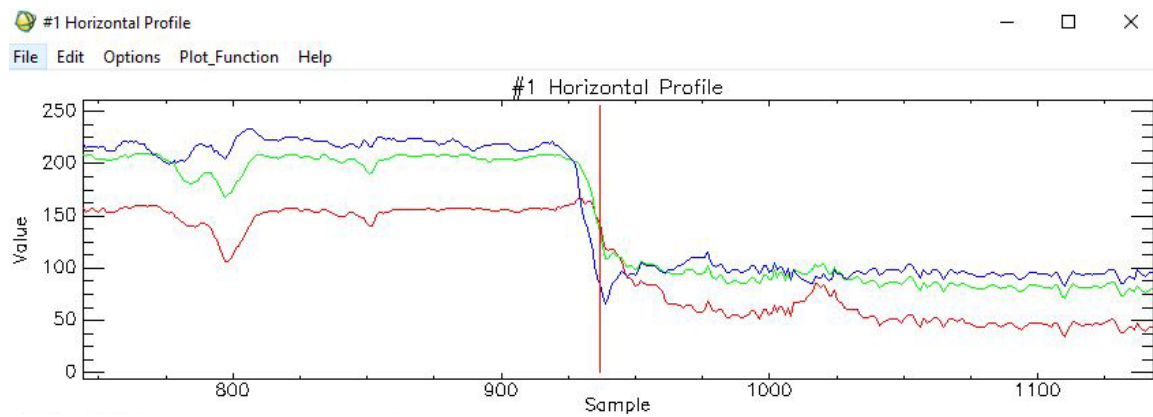
Figure 48 - Profile on the x-axis of the undistorted image of the of the analysis of RGB channels

In both profiles there are deviations between the various channels, but in the second profile the overlap is better and there is more uniform and coordinated behaviour between the RGB channels.

Therefore it can be concluded that the analysis of the individual channels and their subsequent merging leads to a better result than the analysis of the original data, exactly as could be seen in the Coluccia island application.

Therefore it can be concluded that, as far as calibration with Matlab is concerned, there is an improvement of the image if the channels are analysed individually and subsequently merged.

5.2 Application on Metashape

Metashape is one of the most common softwares for photogrammetric applications. This software also allows you to make a camera calibration that you can then use on the survey dataset. The method used is different from the one shown above on Matlab: for the Coluccia island dataset the calibration was done using circular targets, while for the Porto Cesareo dataset it was used the checkerboard. We will now see what were the basic steps and which results were obtained.

The tests that were carried out are the same as in Matlab, i.e. one processing on the original images and the other on the images divided by RGB channel.

5.2.1 Application on original dataset of Coluccia island

For this calibration, 155 images were used. The steps are very similar to those of a classic photogrammetric processing. First of all, the images have to be aligned. This step was done by setting an average accuracy, the generic preselection was removed and the default key point limit and tie point parameters (40,000 and 4,000) were kept. The processing is not complicated as the number of images is not high, in fact the time used is very low, about 1 minute 40 seconds. At the end of the process only one image was not aligned.

As mentioned above, decoded circular markers were used, which the software recognises automatically. Starting the process is simple and intuitive by going to the 'detect marker' section. The marker type and tolerance were chosen as input parameters. In our case a 'Circular 12 bit' marker was chosen because the dataset is small and there is a tolerance of 90. Running the command only takes just under a minute for the program to detect the targets, to which it gives automatic names.
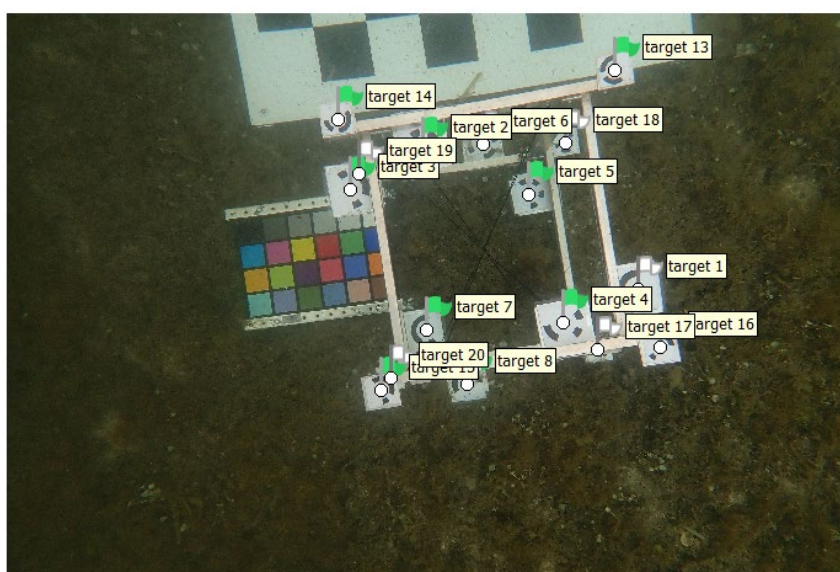
Figure 49 - Output of automatic marker recognition

97

During automatic target recognition, the software also makes projections on the images:

Target 1	31
Target 2	37
Target 3	18
Target 4	31
Target 5	27
Target 6	15
Target 7	17
Target 8	11
Target 13	36
Target 14	37
Target 15	37
Target 16	29
Target 17	49
Target 18	52
Target 19	31
Target 20	30

Table 8 - Number of targets recognized

The next step is to import the coordinates. Since we have used a coded format we import the points ignoring the name and automatically recognise the target to which the coordinates belong. During this step, however, 'target 7' was not recognised, while a new point 'C5' was created, but not in the correct position.
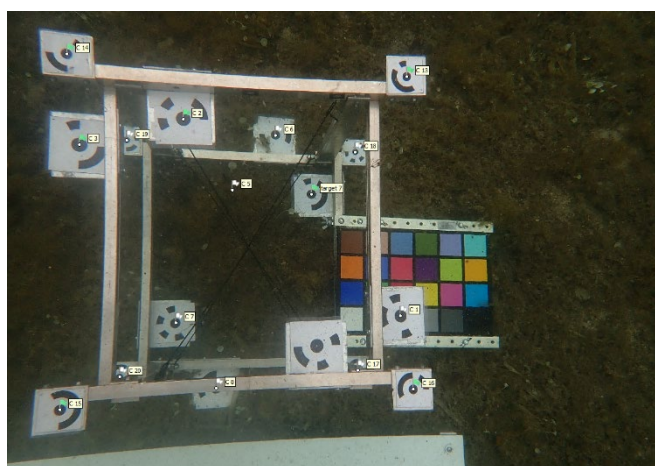
Figure 50 - Image after importing coordinates on coded targets

The control points must have an error congruent with the scale at which the final survey results are to be produced (orthophoto, point cloud, mesh). So if we want a 1:20 scale

output, the error must be below 0.4 cm. The error present in our calibration is 2.4 cm, so it is not acceptable because point 'C4' has the largest error (8.2 cm). By placing it also as a control point, the tolerance is not respected, so it was chosen to remove it.

By doing this, the error is reduced to 0.0089 m and is therefore acceptable.
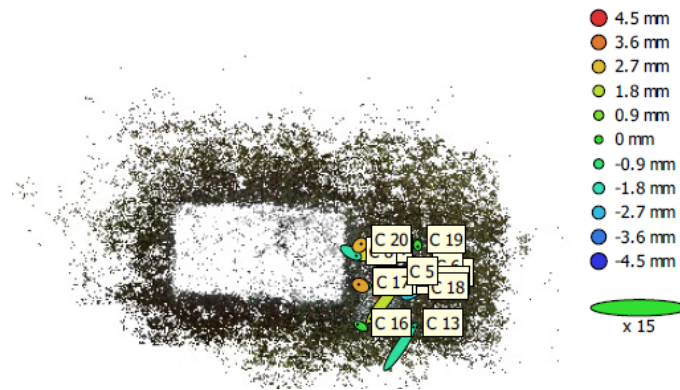
Figure 51 – GCP location and error estimates

The collimated points are more than enough to continue the calibration without manual intervention. The next step is to calculate all the camera parameters (f, c_x, c_y, k_1, k_2, k_3, k_4, b_1, b_2, p_1, p_2). It takes only a few seconds for the machine to calculate these parameters, which once obtained can be easily exported for use during survey processing.

f [pixel]	3945.6
c_x [pixel]	9.4
c_y [pixel]	-1.8
k_1	0.401907
k_2	0.134735
k_3	0.225395
p_1	0.00423102
p_2	0.000248378
b_1	0.823225
b_2	0.119542

Table 9 - Distortion coefficients of the original dataset
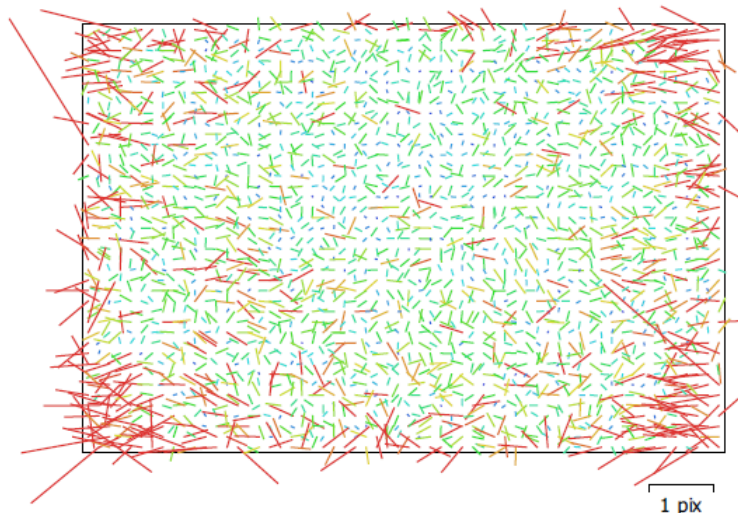
Figure 52 – Image residual after calibration

Once the calibration is complete, Metashape also gives you the option of exporting the undistorted images.

5.2.2 Application on division of the dataset into channels of Coluccia island

As in the previous analysis, which was done with Matlab, images divided by RGB channels were used. Three different datasets were created (one for each channel). Decoded markers were also used in this case. A total of 159 images were processed.

The first step is to import and align the photos. The same settings were used for the three channels, but the results obtained are different. As in the previous case, the characteristics chosen were: an average accuracy, the generic preselection was removed and the default key point limit and tie point parameters (40,000 and 4,000) were kept. The processing times are very different, the blue channel took only 1 minute 6 seconds, the red 2 minutes 28, while the green took much longer than the others - 8 minutes 12 seconds. The number of aligned images are also not the same for the different channels.

	Blue channel	Red channel	Green channel
Aligned images	69/155	121/155	155/155

Table 10 - aligned/total image for each channel

100

It is possible to see that the green channel has the best result and the blue the worst. So even though the green channel took much longer in alignment, it managed to get a better result.

The next step was to have the software recognise the markers automatically. Again, the properties applied are the same as in the previous case, i.e. maker 'Circular 12' and tolerance 90.
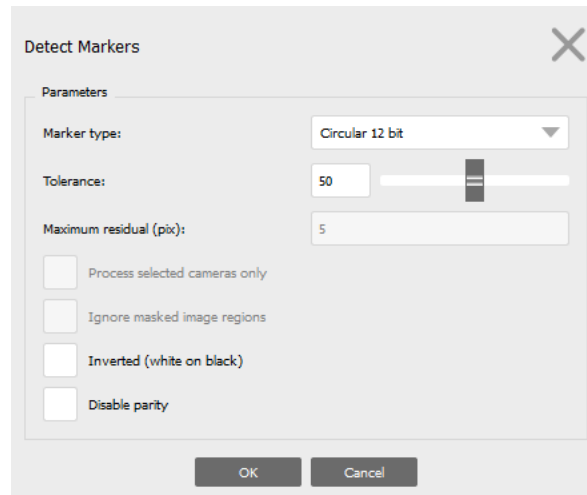
Figure 53 - Detect marker parameters

In this case, it is important that the marker recognition output is consistent with that processed earlier, i.e. that the recognised targets have the same encoding, because if they had a different encoding, an error would occur when importing the coordinates.

Figure 54 - Marker comparison between the original image and the channel divided image

The number of targets automatically collimates varies for each dataset.

	Blue channel	Red channel	Green channel
Target 1	12	7	15
Target 2	17	28	32
Target 3	7	18	16
Target 4	6	13	15
Target 5	15	12	18
Target 6	6	8	14
Target 7	2	12	14
Target 8	7	9	9
Target 13	15	20	30
Target 14	9	30	30
Target 15	14	21	21
Target 16	8	10	13
Target 17	29	27	38
Target 18	28	28	45
Target 19	2	26	28
Target 20	11	24	23

Table 11 - Number of targets recognised for each channel

Consistent with what we have seen so far, the automatic alignment is also better for the green channel and worse for the blue channel.

The next step is to import the coordinates. Since we have used a coded format, we import the points ignoring the name and it automatically recognise the target to which the coordinates belong. Also in this analysis 'target 7' was not recognised, while a new point 'C5' was created, but not in the correct position.

Here again, it is necessary to check the errors obtained, to be sure that we have no problems in our calibration. Comparing the results:

	Blue channel	Red channel	Green channel
Mean error	2.42 cm	2.42cm	2.431 cm

Table 12 – Mean error for each channel

The errors present in our calibration are not acceptable because point 'C4' has the largest error, 8.25 cm for the blue channel, 8.26 for the red channel and 8.25 for the green channel.

By placing it also as a control point, the tolerance is not respected, so it was chosen to remove it.

By doing this, the errors are reduced to:

	Blue channel	Red channel	Green channel
Mean error	0.89 cm	0.89 cm	0.89 cm

Table 13 – Mean error for each channel
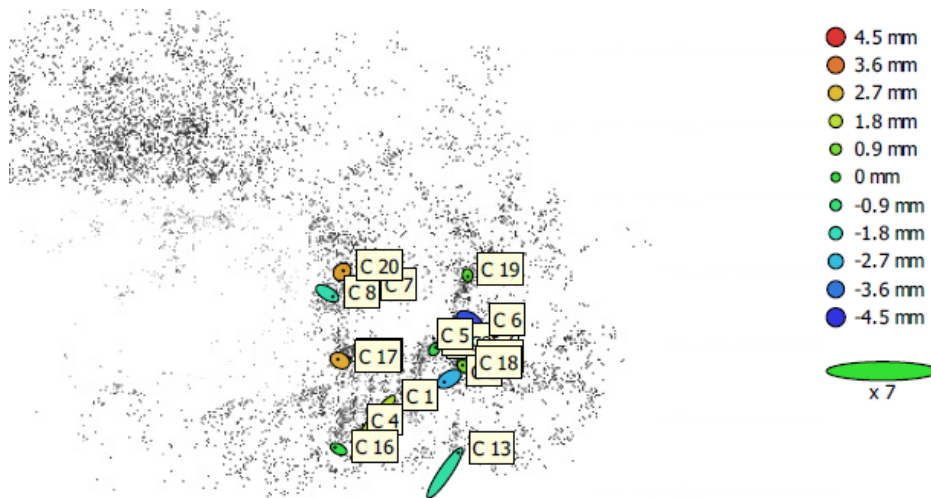
Figure 55 - GCP location and error estimates blue channel

Figure 56 - GCP location and error estimates red channel
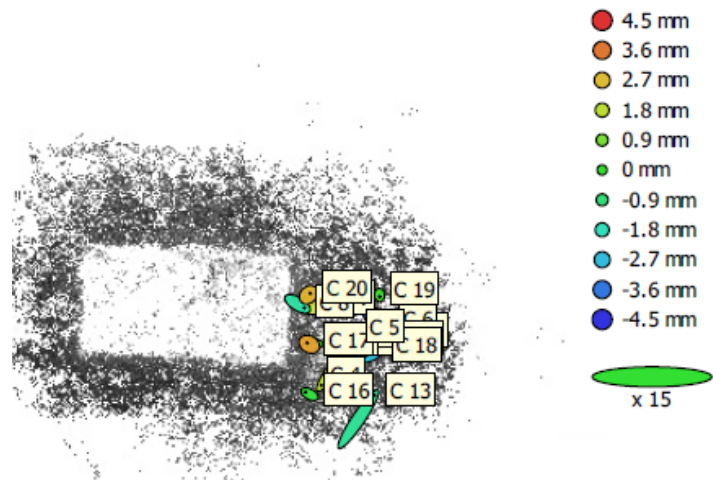
Figure 57 - GCP location and error estimates red channel

Errors are now acceptable, so calibration can proceed. The next step is to calculate all camera parameters ($f, c_x, c_y, k_1, k_2, k_3, k_4, b_1, b_2, p_1, p_2$). Comparing them, we obtain:

	Blue channel	Red channel	Green channel
f [pixel]	3944.89509	3941.42715	3949.82397
c_x [pixel]	12.861	8.74036	8.38659
c_y [pixel]	4.58619	1.50347	-2.53902
k_1	0.40405	0.384562	0.396237
k_2	0.240642	0.193631	0.191419
k_3	-0.133451	0.169984	0.0907841
p_1	0.00534186	0.0039436	0.00402977
p_2	0.00142804	0.000830126	0.000164465
b_1	0.364841	0.732239	1.25773
b_2	-0.15861	-0.158196	0.00278679

Table 14 - Distortion coefficients for each channel
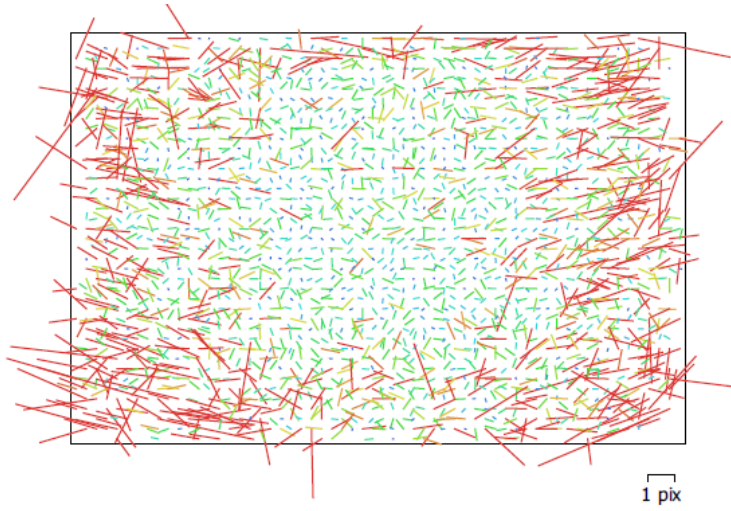
Figure 58 - Image residual after calibration of blue channel
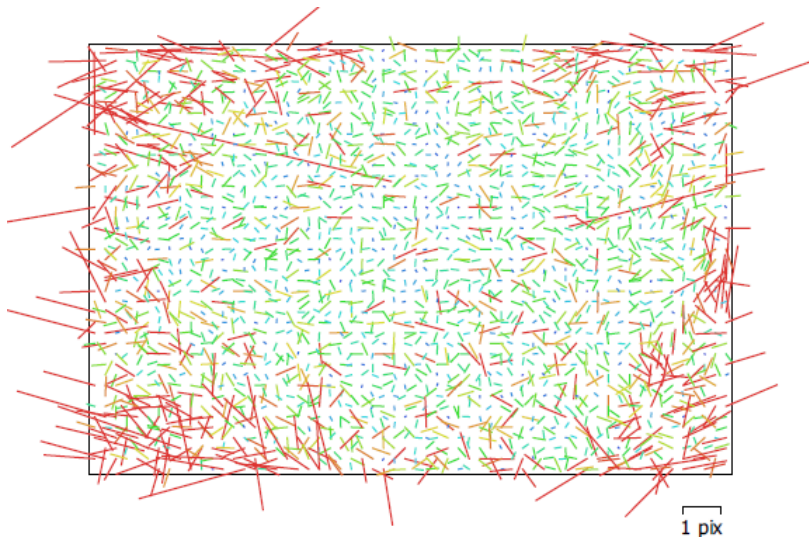
Figure 59 - Image residual after calibration of red channel
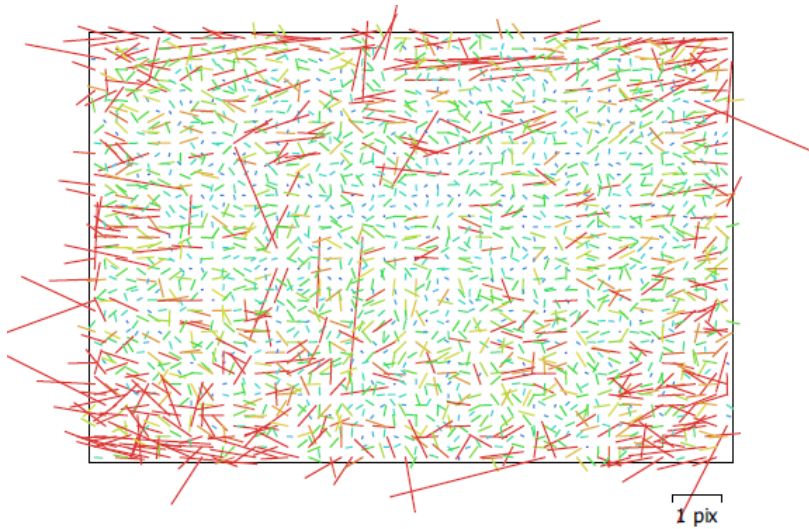
Figure 60 - Image residual after calibration green channel

After this, the images are exported and then merged using a code in Matlab (Appendix B). The result obtained is not satisfactory, as the images turn out not to be superimposed correctly.

Figure 61 - Unified undistorted image

As can be seen in Figure 61, there are coloured borders around the target, a blue one on the left, green on the bottom, yellow on the right and magenta at the top. This phenomenon is present because the undistorted images of the three RGB channels have very different coordinates of the main points, which causes the images not to be perfectly aligned during unification.

	Blue channel	Red channel	Green channel
c_x [pixel]	12.9	8.7	8.4
c_y [pixel]	4.6	1.5	-2.6

Table 15 - Principal point coordinates

7.2.3 Coluccia island results compared

As with Matlab, the choice of the dual approach was used to see if there was a better result by analysing the channels separately.

It can be seen that in this image dataset, the presence of distortions within the images is very evident.
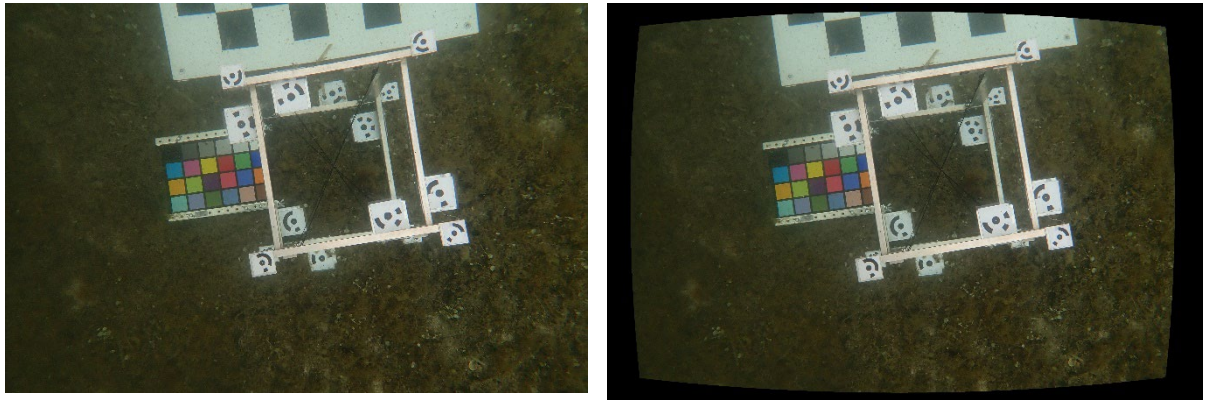
Figure 62 - Comparison of original (left) and undistorted image (right)

Unfortunately, since the effect shown in figure 61 is present in the unified image, it is not possible to make a direct comparison as to which of the two approaches is the best. For this reason, when processing the survey it is advisable to use either the parameters derived in Matlab for the split RGB channels, or to choose the approach with the original images on Metashape.

5.2.4 Application on original dataset of Porto Cesareo

For this calibration, 70 images were used. The alignment of the photos was done by setting an average accuracy, the generic preselection was removed and the default key point limit and tie point parameters (40,000 and 4,000) were kept. The processing is not complicated as the number of images is not high, in fact the time used is very low, only 43 seconds. At the end of the process only two images were not aligned.

The checkerboard was used for this analysis, but we wanted to try using automatic calibration point recognition anyway. In this case the marker chosen is 'Cross (not coded)' a tolerance of 50. The command took longer than the previous processing, but more importantly, many incorrect targets were created. This happens because there are many reflections due to the underwater environment.

Figure 63 - Target recognition with false positives

In an attempt to make the next steps easier, the automatic recognition was redone, but by drastically decreasing the tolerance, setting it to 9.
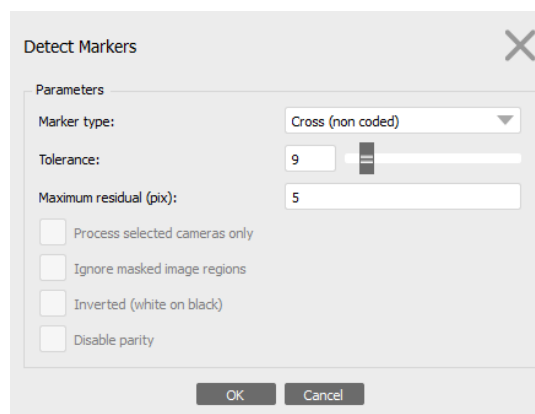
Figure 64 - Detect marker parameters

The result obtained is better than the previous one, but not sufficient, as many false positives are still present. All unnecessary targets were removed manually, resulting in a clear and clean result.
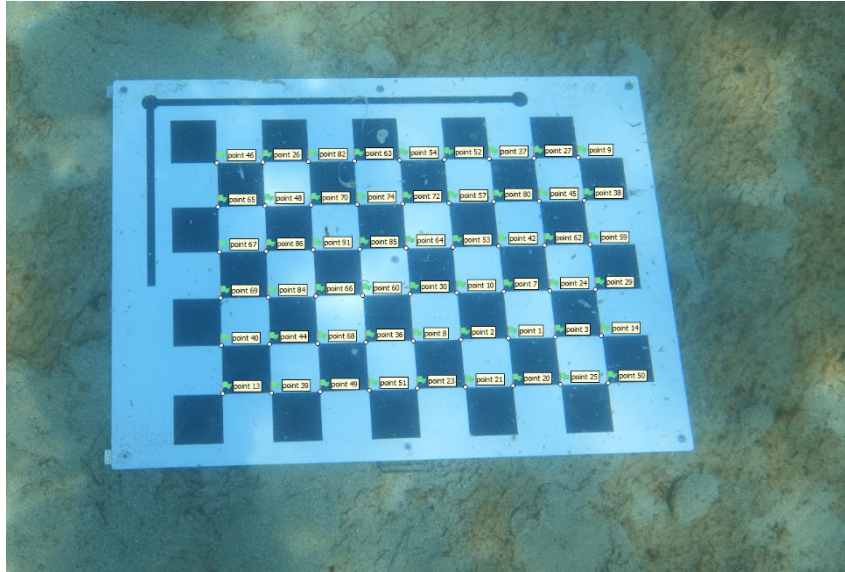
Figure 65 - Checkerboard with only points of interest

In order to continue with the calibration, an excel file was created containing the x, y and z coordinates of the panel. The first cross present following the plane drawn on the checkerboard was used as the point of origin, and a point was set every 10 cm (size of the square). This created a file with 54 points, which was exported in csv format to be imported into Metashape.

	A	B	C	D	E	F	G	H	I	J	K	L	M	N
1	1	0	0	0		11	0,1	0,1	0		21	0,2	0,2	0
2	2	0	0,1	0		12	0,1	0,2	0		22	0,2	0,3	0
3	3	0	0,2	0		13	0,1	0,3	0		23	0,2	0,4	0
4	4	0	0,3	0		14	0,1	0,4	0		24	0,2	0,5	0
5	5	0	0,4	0		15	0,1	0,5	0		25	0,2	0,6	0
6	6	0	0,5	0		16	0,1	0,6	0		26	0,2	0,7	0
7	7	0	0,6	0		17	0,1	0,7	0		27	0,2	0,8	0
8	8	0	0,7	0		18	0,1	0,8	0		28	0,3	0	0
9	9	0	0,8	0		19	0,2	0	0		29	0,3	0,1	0
10	10	0,1	0	0		20	0,2	0,1	0		30	0,3	0,2	0
11														

Figure 66 - Part of the excel file created for point coordinates

During automatic target recognition, the software also makes projections on the images:

Name	N° collimations	Name	N° collimations	Name	N° collimations
1	60	19	60	37	60
2	62	20	62	38	61
3	63	21	62	39	62
4	67	22	65	40	62
5	67	23	67	41	63
6	68	24	68	42	63
7	68	25	68	43	62
8	68	26	68	44	63
9	68	27	67	45	63
10	60	28	60	46	61
11	62	29	61	47	61
12	63	30	64	48	61
13	67	31	65	49	60
14	66	32	64	50	61
15	68	33	65	51	61
16	67	34	64	52	60
17	68	35	64	53	61
18	68	36	63	54	60

Table 16 - Number of collimations per point

Keeping in mind that there are 68 aligned images and the lowest number of collimations and 60, we can be more than satisfied.

Again, it is necessary to do a check on the errors obtained, to make sure there are no problems in our calibration. The average error obtained is 0.006 m, which is much lower then 0.4 cm.

Figure 67 – GCP location an error estimates

The next step is to calculate all the camera parameters (f, c_x, c_y, k_1, k_2, k_3, k_4, b_1, b_2, p_1, p_2). The result obtained is:

f [pixel]	5291.6
c_x [pixel]	-22.7
c_y [pixel]	-31.2
k_1	-0.0158164
k_2	-0.0155306
k_3	0.02568
p_1	0.000326137
p_2	-0.000674787
b_1	-0.682092
b_2	-0.482134

Table 17 – Calibration coefficients
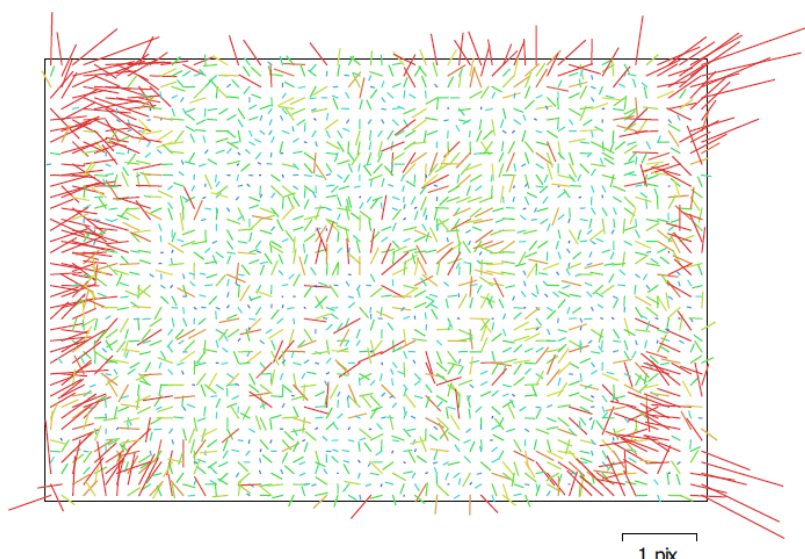
Figure 68 – Image residuals

5.2.5 Application on division of the dataset into channels of Porto Cesareo

As with the Coluccia Island analysis, this dataset of 70 images was divided into RBG channels, creating three different datasets. For all channels the photo alignment was done by setting an average accuracy, generic preselection was removed and the default key point limit and tie point parameters (40,000 and 4,000) were kept. Processing times are very

similar, here, the blue channel took only 15 seconds, the red 14 seconds, and the green 21 seconds. Even the number of aligned images are not the same for the different channels.

	Blue channel	Red channel	Green channel
Aligned images	68/70	65/70	70/70

Table 18 - Aligned/total image for each channel

It can be seen that the green channel has the best result and the red channel the worst, although 93% of the images were also aligned for the red channel.

The next step, the recognition of points, was done with the same settings as in the previous application. Again, there were false positives which were removed manually until only the points of interest were obtained.
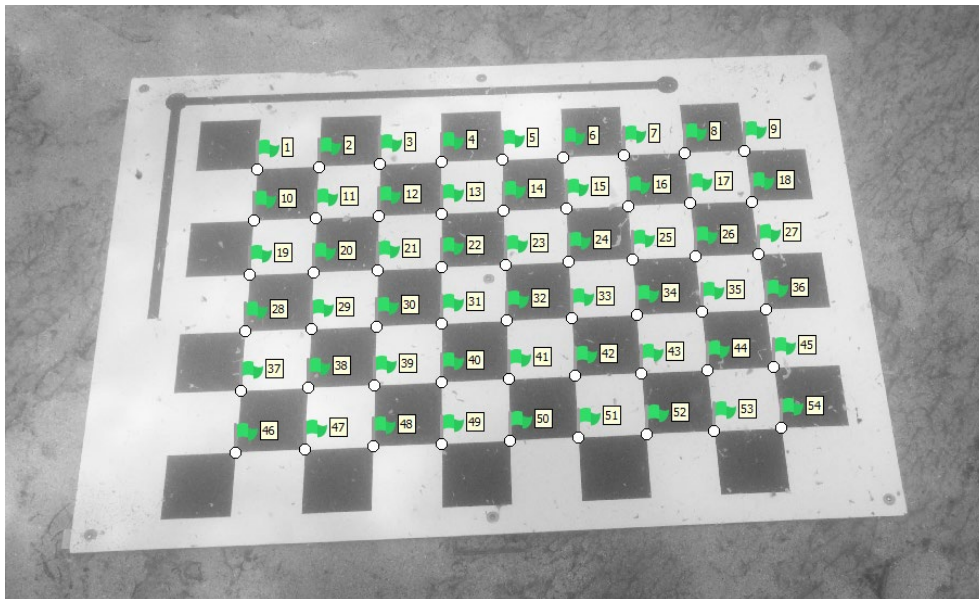
Figure 69 - Target image with correct coding

It is necessary to check the errors obtained, to be sure that we have no problems in our calibration. Comparing the results:

	Blue channel	Red channel	Green channel
Mean error	0.0006 m	0.0006 m	0.0006 m

Table 19 - Mean error for each channel
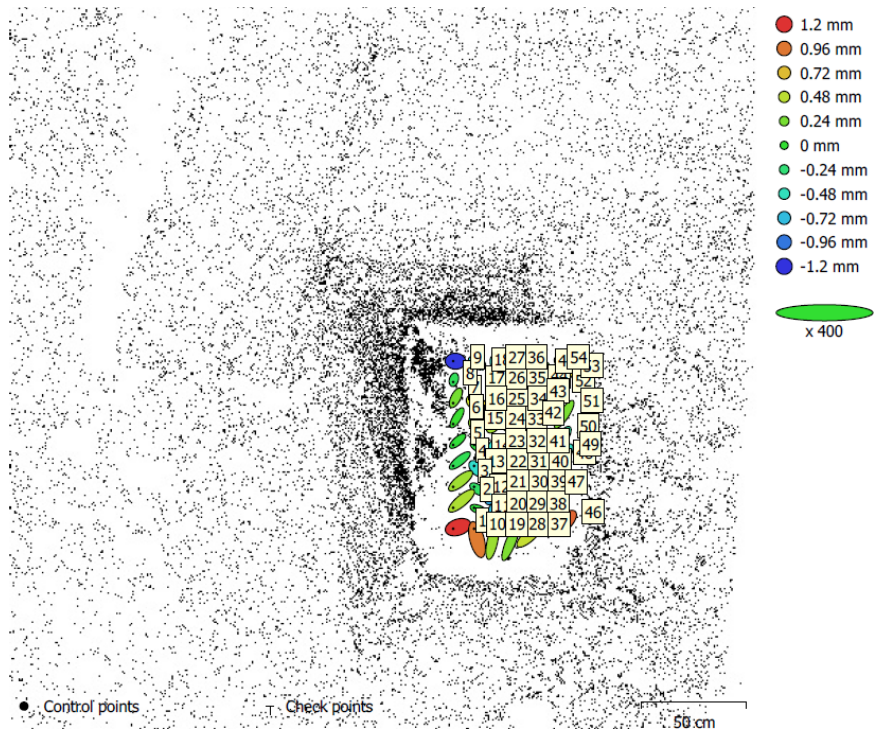
Figure 70 – GCP location and error estimates blue channel
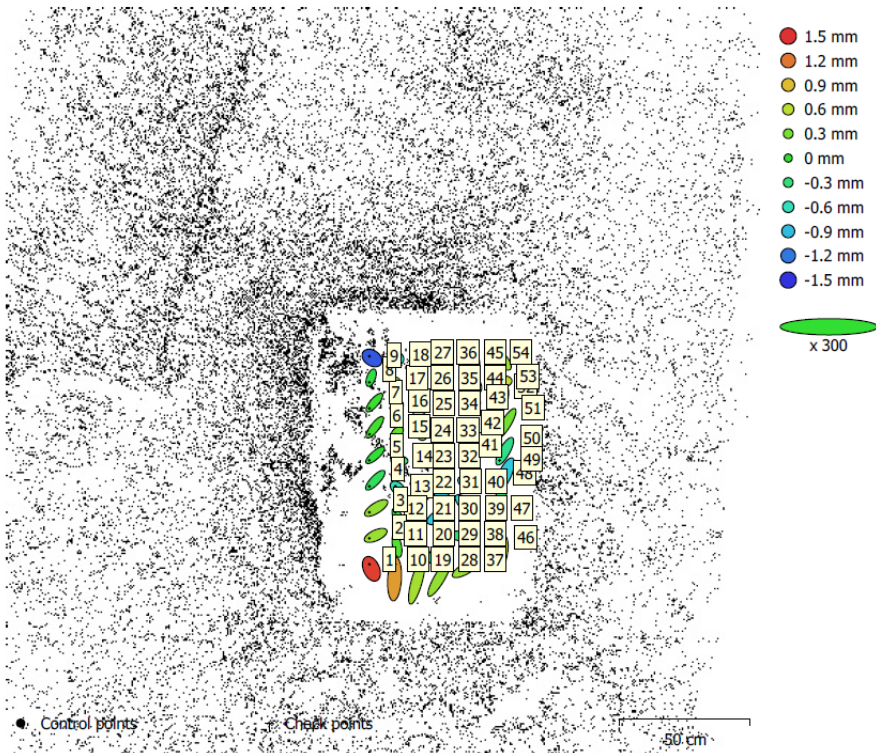
Figure 71 – GCP location and error estimates red channel

113
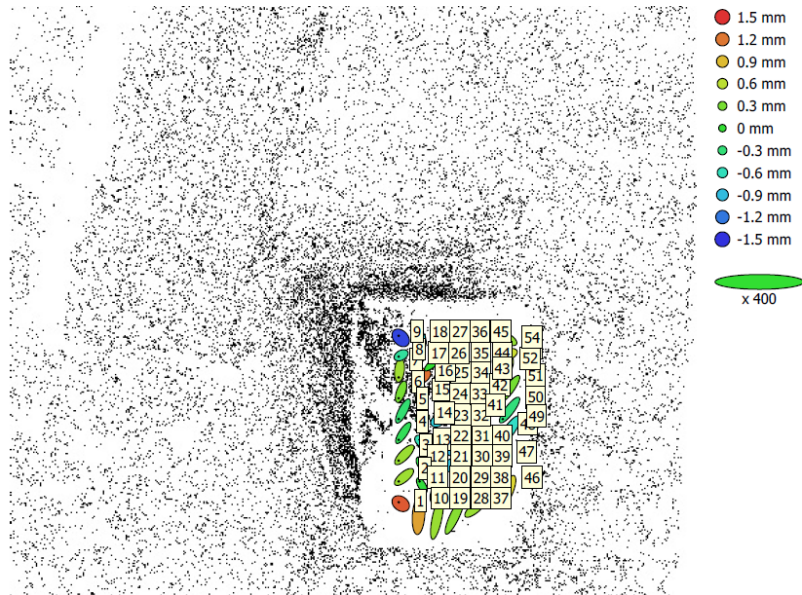
Figure 72 – GCP location and error estimates green channel

Since the errors are acceptable, we can proceed with the processing.

Once the coordinate file has been imported, it is possible to make initial considerations on point collimations.

For the blue channel:

Name	N° collimations	Name	N° collimations	Name	N° collimations
1	60	19	59	37	59
2	62	20	62	38	61
3	63	21	62	39	62
4	67	22	65	40	62
5	67	23	67	41	61
6	68	24	68	42	62
7	68	25	68	43	63
8	68	26	68	44	63
9	68	27	67	45	62
10	60	28	60	46	59
11	62	29	61	47	60
12	63	30	64	48	61
13	66	31	65	49	60
14	67	32	64	50	61
15	68	33	65	51	61
16	67	34	64	52	61
17	68	35	64	53	61
18	68	36	63	54	58

Table 20 - Number of collimations per point blue channel

For the red channel:

Name	N° collimations	Name	N° collimations	Name	N° collimations
1	57	19	57	37	56
2	59	20	59	38	58
3	60	21	59	39	59
4	64	22	62	40	59
5	64	23	64	41	60
6	65	24	65	42	60
7	65	25	65	43	59
8	65	26	65	44	60
9	65	27	64	45	60
10	57	28	57	46	58
11	59	29	58	47	58
12	60	30	61	48	58
13	64	31	62	49	57
14	64	32	61	50	58
15	65	33	62	51	58
16	65	34	61	52	58
17	65	35	61	53	58
18	62	36	60	54	57

Table 21 - Number of collimations per point red channel

For the green channel:

Name	N° collimations	Name	N° collimations	Name	N° collimations
1	60	19	60	37	60
2	62	20	62	38	61
3	63	21	62	39	62
4	67	22	65	40	62
5	68	23	69	41	63
6	69	24	70	42	63
7	70	25	70	43	62
8	69	26	69	44	63
9	68	27	67	45	63
10	60	28	60	46	61
11	62	29	61	47	61
12	63	30	64	48	61
13	67	31	65	49	60
14	68	32	64	50	61
15	70	33	65	51	61
16	69	34	64	52	60
17	69	35	64	53	61
18	68	36	63	54	60

Table 22 - Number of collimations per point

The next step is to calculate all camera parameters (f, c_x, c_y, k_1, k_2, k_3, k_4, b_1, b_2, p_1, p_2).

Comparing them, we obtain:

	Blue channel	Red channel	Green channel
f [pixel]	5286.3	5293.0	5287.5
c_x [pixel]	-27.4	-20.0	-22.3
c_y [pixel]	-28.3	-32.1	-29.0
k_1	-0.0117561	-0.017462	-0.01559679
k_2	-0.0212461	-0.0147184	-0.015252
k_3	0.0239272	0.0201351	0.0202128
p_1	0.000107262	0.000405257	0.000323839
p_2	-0.000328702	-0.000762068	-0.000577875
b_1	-0.548623	0.078127	-0.717824
b_2	0.456559	-0.764986	-0.687674

Table 23 - Distortion coefficients and correlation matrix for each channel
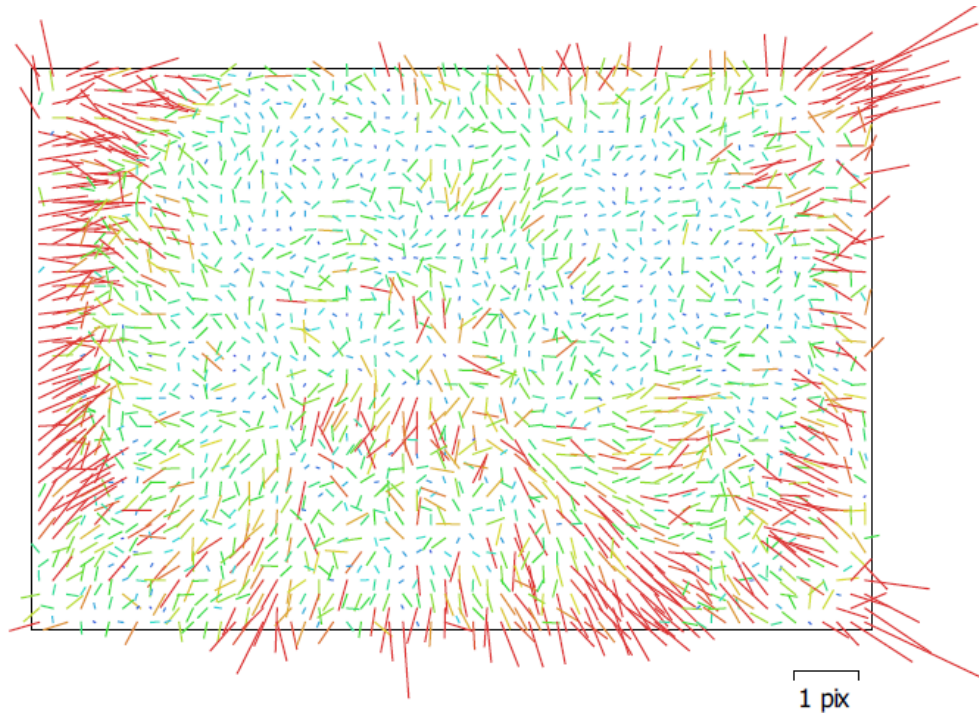
Figure 73 – Image residuals blue channel

116

1 pix
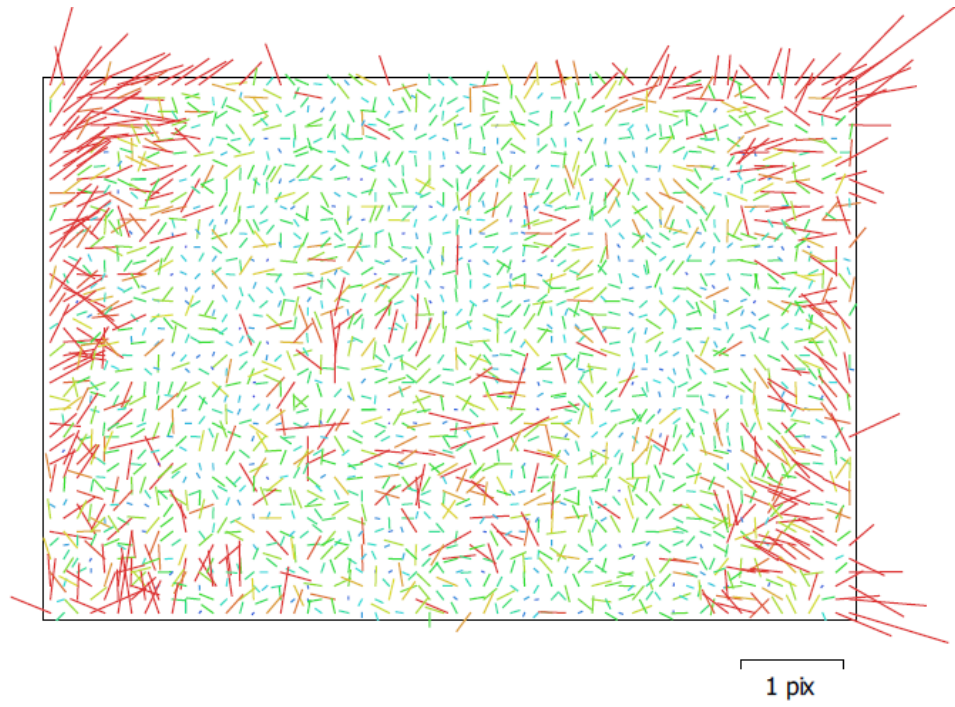
Figure 74 – Image residuals red channel

1 pix
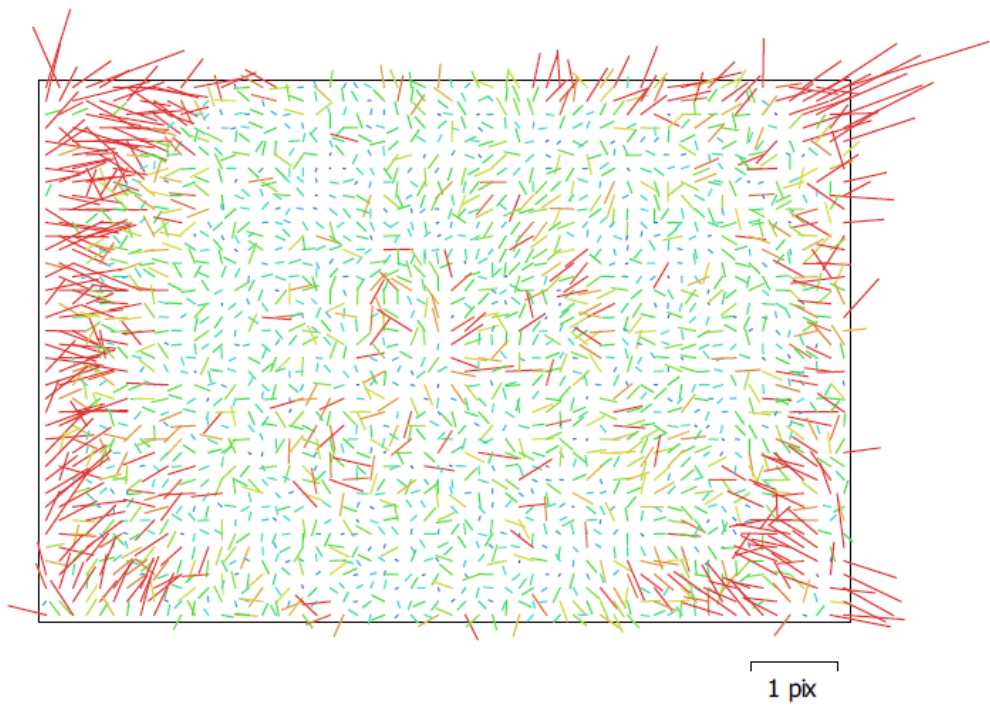
Figure 75 – Image residuals green channel

Firstly the images are exported and then merged using a code in Matlab (Appendix B).

117

The result obtained is not satisfactory, as the images turn out not to be superimposed correctly.
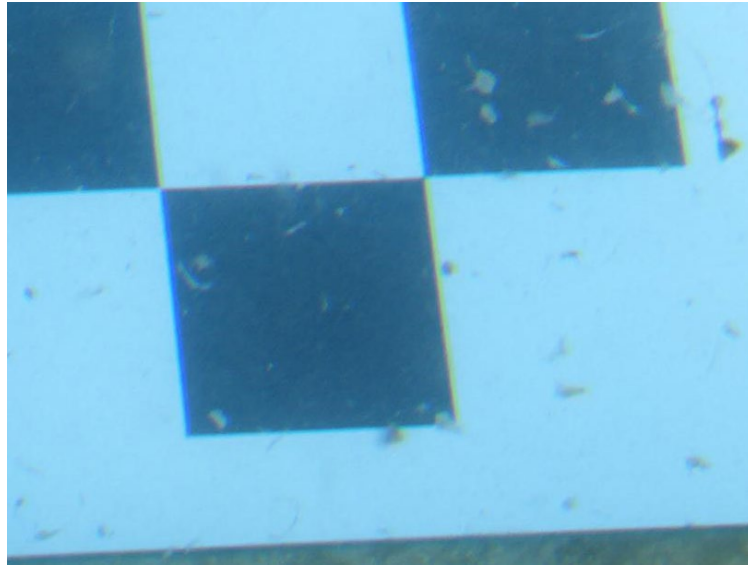
Figure 76 - Unified undistorted image

As can be seen in Figure 76, there are coloured borders around the target, a blue one on the left, green on the bottom, yellow on the right and magenta at the top. This phenomenon is present because the undistorted images of the three RGB channels have very different coordinates of the main points, which causes the images not to be perfectly aligned during unification.

	Blue channel	Red channel	Green channel
c_x [pixel]	-27.4241	-20.0344	-22.3261
c_y [pixel]	-28.25.79	-32.1156	-29.005

Table 24 - Principal point coordinates

5.2.6 Porto Cesareo results compared

One should note the considerable difference between the images acquired at Coluccia Island and Porto Cesareo in terms of the presence of distortion. The second dataset shows much less radial distortion thanks to the use of a dome, which greatly helps the camera to

reduce it. In fact, it is possible to notice a small correction of the images only at the edges, which is much less pronounced than in the first dataset analysed.
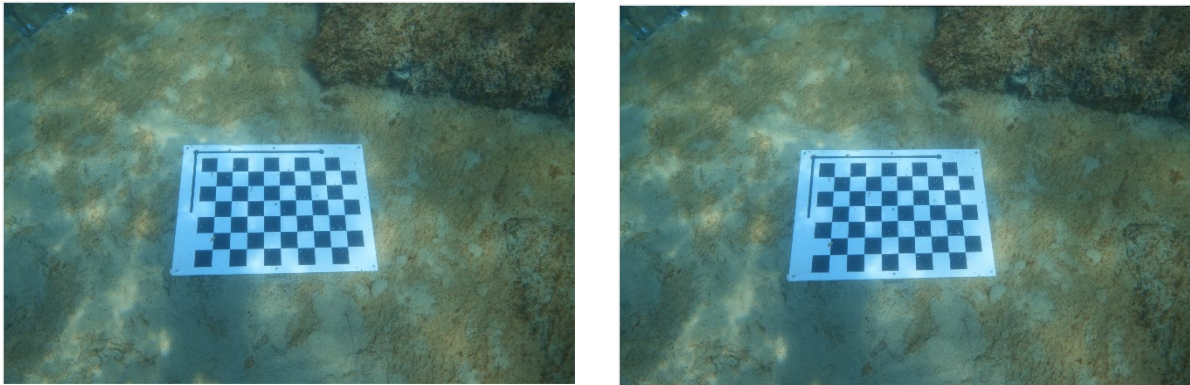
Figure 77 - Comparison of original (left) and undistorted image (right)

In fact, it is possible to notice a small correction of the images only at the edges, which is much less pronounced than in the first dataset analysed.

Figure 78 - Focus on the image to show distortion

As with the Coluccia Island processing and as shown in Figure 76, it is not possible to make a direct comparison as to which of the two approaches is the best.

For this reason, when processing the survey, it is advisable to use either the parameters derived in Matlab for the split RGB channels, or to choose the approach with the original images on Metashape.

Chapter 6

Stereoscopic camera calibration

The DIATI and DAD departments of the Polytechnic University of Turin have collaborated to create a stereoscopic system consisting of two Sony ILX-LR1 cameras and the use of the dome. The cameras are protected by an enclosure that allows them to withstand higher pressures. A screen was connected to the back of the cameras to preview the image acquisition.

Figure 79 - Sony with the protective case

For both cameras, electrical connections have been made connected to an external switch that allows for synchronized triggering of images.

Figure 80 - System for synchronized shooting

The whole system is connected by a rigid rod that is intended to keep the cameras from moving during acquisition. This instrument should not weigh excessively so as not to put the operator in difficulty during the survey.

Figure 81 - Stereoscopic system

This system was used for the survey at the columns of Porto Cesareo. A few considerations must be made before proceeding with the results. The system used was not perfectly synchronised, as some images were only acquired with one camera and not with both. The number of images acquired, during the entire survey, with the right camera (A) are 736, those acquired with the left camera are 1402 and those that turn out to be well synchronised are 697. Therefore about 35% of the images are not synchronised and cannot be used for stereoscopic processing.

A total of 70 images of the checkerboard were used for calibration. For this first part, the system is well synchronised as the two cameras have the same number of images. As in the previous cases, we will proceed using the original images and those divided by RGB channels, using only the Metashape software. Another analysis that has been carried out is to assess whether there is an improvement and, if so, by how much, if you constrain the processing by imposing a distance between the two centres. So a processing without any constraint and one by imposing a distance between the cameras will be shown. Furthermore, the best results will be used on the complete survey dataset to complete the whole photogrammetric process.

6.1 Application without constraints between the two cameras

6.1.1 Application on original dataset

The first analysis is done using the original images and without using any constraints, to allow the software to move and rotate the images. As mentioned above, 70 images were used. During the processing, the Metashape user manual [45] was used where it shows how to import and process images correctly.

Before importing the images into the software, they must be organised correctly. You will need to import a folder into Metashape, with a sub-folder inside for each camera used. The program uses the one on the left as the master camera, but it is not recognised automatically. In fact, the software uses the first folder as master, so you have to make sure that the first subfolder is that of the camera on the left. It is therefore necessary that only the paired images are inside the subfolder.

Once the images to be processed have been properly prepared, they can be imported into the software. Selecting the Metashape folder, it will ask how you want to import the images, whether as single, multi-camera or dynamic.
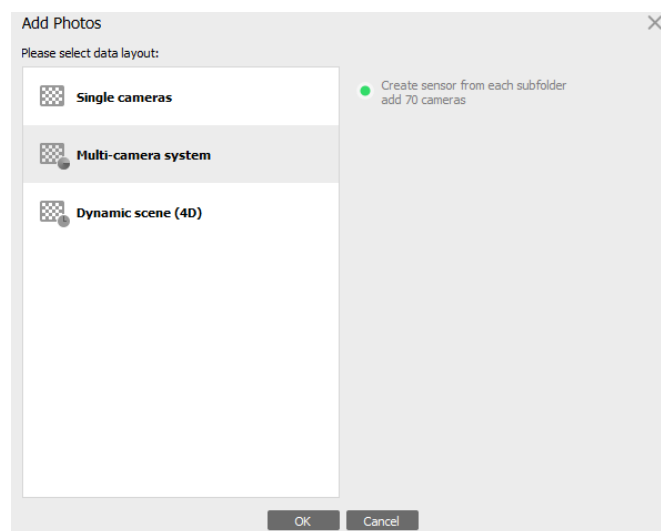
Figure 82 - Metashape Image Import Screen

If you select multi-camera the images will be automatically matched by the software.
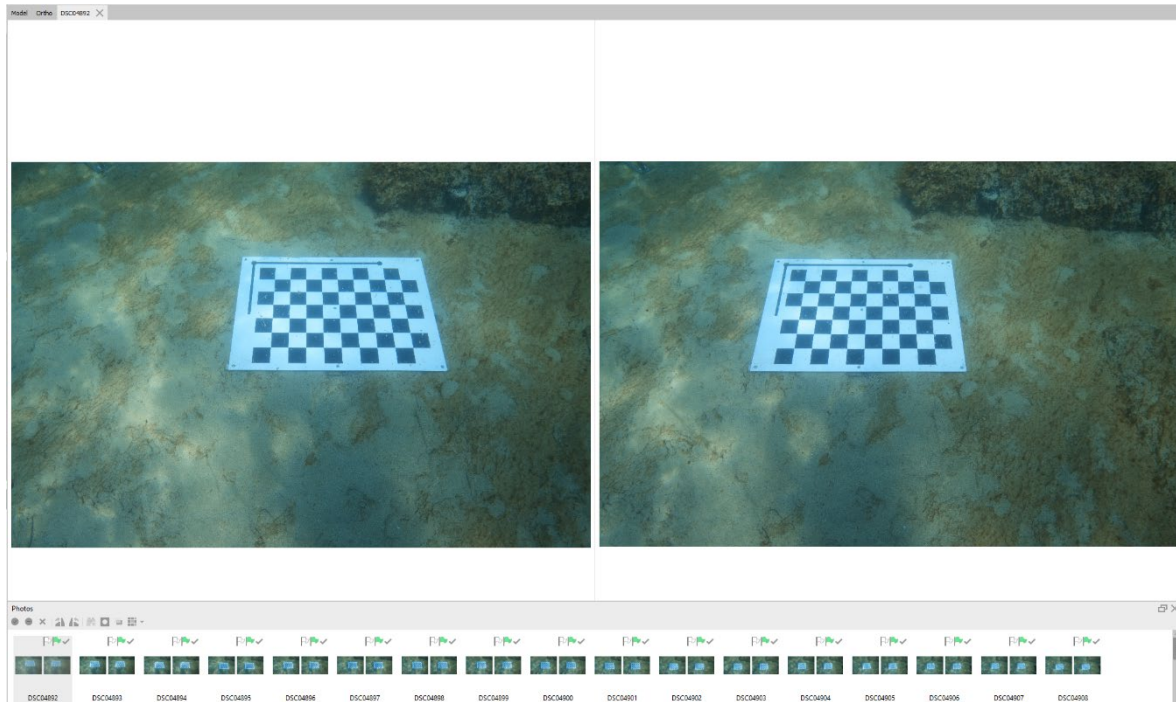
Figure 83 - Visualisation of stereoscopic images on Metashape

Once the import is finished, if you go to the 'Camera calibration' section, you can see both cameras, the first being the master. It is possible to notice a section that is not present in classic processing, 'Slave offset', which can only be selected for the second camera, as inside it is possible to set the offset parameters from the master camera's grip centre. In this case, we only tick the boxes 'adjust rotation', 'enable reference' (for x, y, and z as well as for Omega, phi and kappa), 'adjust location'.
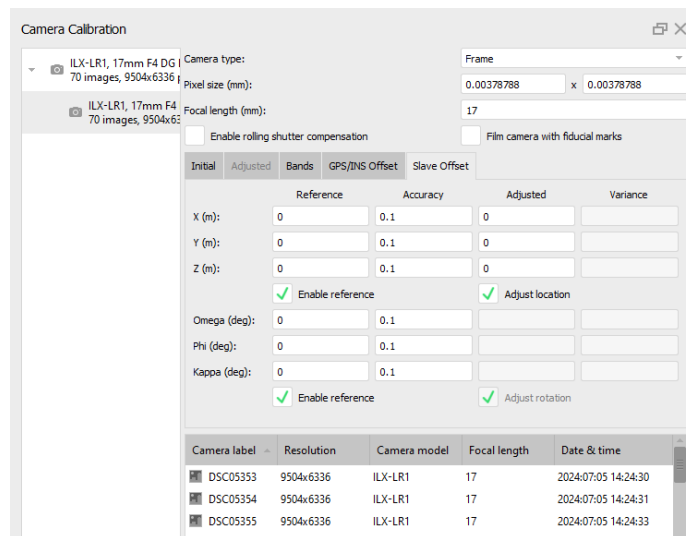
Figure 84 - Camera calibration tool

Afterwards, the classic photogrammetric procedures could be carried out. The photo alignment was done by setting an average accuracy, generic preselection was removed, and the default key point limit and tie point parameters (40,000 and 4,000) were kept. The processing is not complicated as the number of images is not high, in fact the time used is very low, 43 seconds. At the end of the process two pairs of images were not aligned.

The checkerboard was used for this processing, so automatic marker recognition is carried out again, as explained in the previous paragraphs, also using the same parameters as in section 7.2.4.

Once recognition is complete, we delete all targets that do not belong to the checkerboard and import the coordinates of the points. The number of targets that are automatically collimated is:

Name	N° collimations	Name	N° collimations	Name	N° collimations
1	5	19	5	37	10
2	4	20	6	38	11
3	7	21	5	39	11
4	35	22	10	40	37
5	36	23	35	41	38
6	36	24	36	42	39
7	36	25	36	43	39
8	37	26	35	44	39
9	38	27	36	45	38
10	5	28	13	46	11
11	5	29	10	47	10
12	5	30	10	48	14
13	5	31	36	49	36
14	35	32	37	50	37
15	36	33	38	51	37
16	35	34	38	52	37
17	36	35	37	53	37
18	36	36	37	54	36

Table 25 - Number of collimations per point

It is necessary to check the errors obtained, to make sure there are no problems in our calibration. The average error obtained is 0.007 m, which is much lower than 0.4 cm.
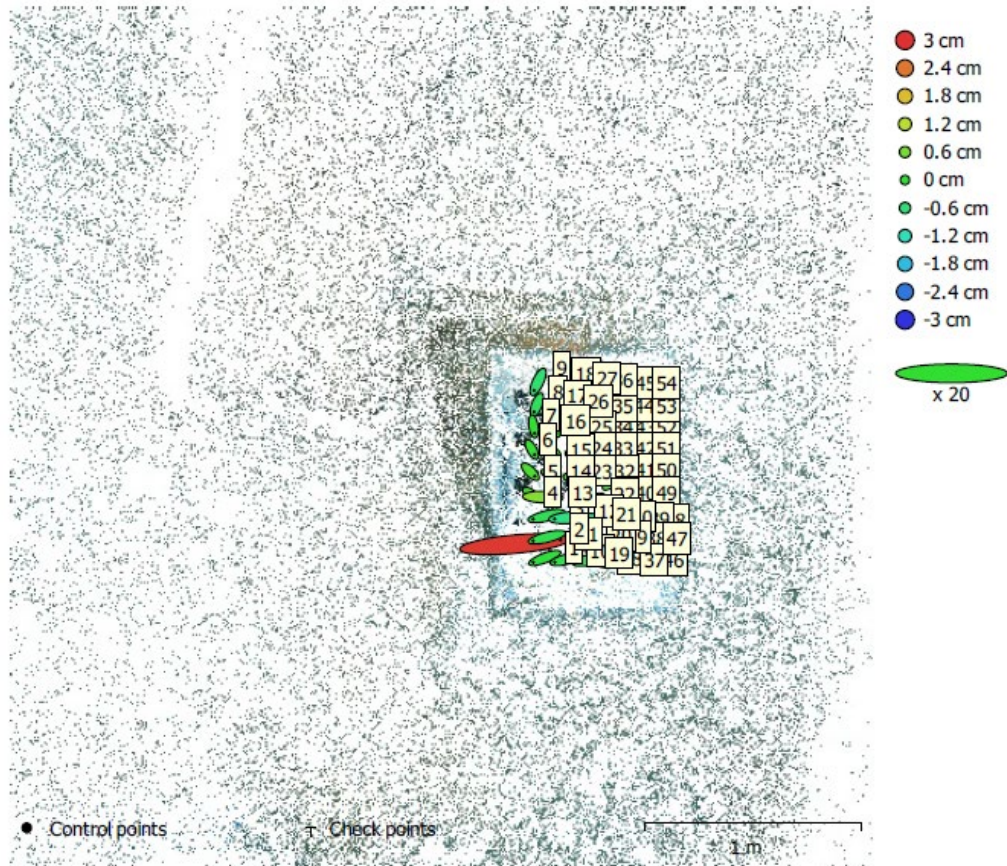
Figure 85 – GCP locations and error estimates

The next step is to calculate all the camera parameters(f, c_x, c_y, k_1, k_2, k_3, k_4, b_1, b_2, p_1, p_2). The result obtained is for each camera:

	Camera A	Camera B
f [pixel]	5253.4	5297.0
c_x [pixel]	-5.7	19.4
c_y [pixel]	109.4	106.5
k_1	-0.0432495	0.0127579
k_2	0.0303681	-0.0553145
k_3	-0.00449246	0.0427557
p_1	0.00254722	0.00436207
p_2	0.00472266	0.0039821
b_1	2.63531	4.61169
b_2	-8.98253	-13.279

Table 26 - Distortion coefficients for each camera
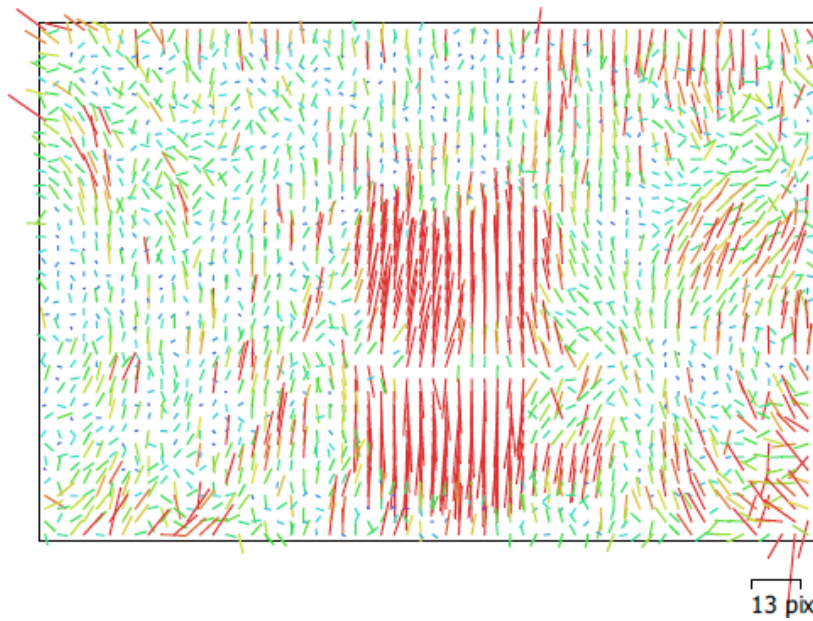
Figure 86 - Image residuals camera B
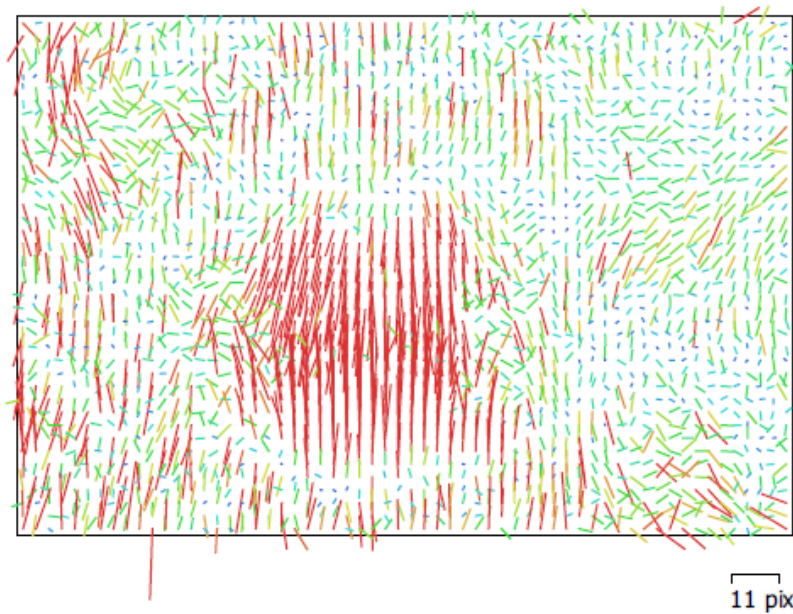
Figure 87 - Image residuals camera A

The last point to be made is about the 'Slave offset' parameters. By not imposing any limits, the software was able to rotate and translate the images freely, resulting in:

	Adjusted	Sqm
x	0.3397	0.0025
y	0.0021	6.7374e-05
z	0.0225	0.0002

Table 27 - Slave offset output

This means that the software calculated a distance between the gripping centres of 33,97 cm.

6.1.2 Application on division of the dataset into channels

This section shows the results obtained from the analysis of images divided into RGB channels. A folder was created for each channel and, within it, the two cameras were divided.

For all channels the photo alignment was done by setting an average accuracy, generic preselection was removed and the default key point limit and tie point parameters (40,000 and 4,000) were kept. Processing times are very similar here, the blue channel took only 15 seconds, the red 14 seconds, and the green 21 seconds. Even the number of aligned images are not the same for the different channels.

	Blue channel	Red channel	Green channel
Aligned images	68/70 couples	67/70 couples	70/70 couples

Table 28 - Aligned/total image for each channel

It can be seen that the green channel has the best result and the red channel the worst, although 96% of the images were also aligned for the red channel.

The next step, the recognition of points, was done with the same settings as in the previous application. Again, there were false positives which were removed manually until only the points of interest were obtained.

Once the coordinate file has been imported, it is possible to make initial considerations on point collimations.

For the blue channel:

Name	N° collimations	Name	N° collimations	Name	N° collimations
1	3	19	36	37	8
2	14	20	6	38	8
3	8	21	4	39	10
4	38	22	35	40	37
5	37	23	14	41	36
6	37	24	38	42	40
7	36	25	40	43	41
8	38	26	38	44	40
9	37	27	38	45	37
10	4	28	9	46	9
11	4	29	10	47	10
12	37	30	11	48	10
13	38	31	36	49	12
14	4	32	38	50	37
15	35	33	39	51	37
16	37	34	41	52	37
17	37	35	40	53	10
18	38	36	38	54	34

Table 29 - Number of collimations per point blue channel

For the red channel:

Name	N° collimations	Name	N° collimations	Name	N° collimations
1	34	19	7	37	7
2	9	20	4	38	6
3	36	21	34	39	4
4	36	22	5	40	4
5	36	23	37	41	34
6	37	24	36	42	34
7	36	25	35	43	33
8	36	26	35	44	32
9	36	27	34	45	31
10	4	28	6	46	5
11	34	29	6	47	36
12	34	30	36	48	2
13	37	31	5	49	16
14	37	32	35	50	33
15	36	33	34	51	33
16	36	34	33	52	34
17	35	35	32	53	32
18	34	36	38	54	14

Table 30 - Number of collimations per point red channel

For the green channel:

Name	N° collimations	Name	N° collimations	Name	N° collimations
1	5	19	6	37	12
2	7	20	6	38	12
3	4	21	11	39	11
4	35	22	10	40	38
5	36	23	35	41	38
6	36	24	35	42	39
7	36	25	36	43	39
8	37	26	36	44	39
9	38	27	36	45	37
10	6	28	12	46	12
11	5	29	12	47	11
12	5	30	11	48	12
13	34	31	36	49	36
14	34	32	35	50	37
15	36	33	36	51	37
16	34	34	37	52	37
17	36	35	37	53	39
18	36	36	35	54	37

Table 31 - Number of collimations per point green channel

It is necessary to check the errors obtained, to be sure that we have no problems in our calibration. Comparing the results:

	Blue channel	Red channel	Green channel
Mean error	0.0100 m	0.0103 m	0.0006 m

Table 32 - Mean error for each channel
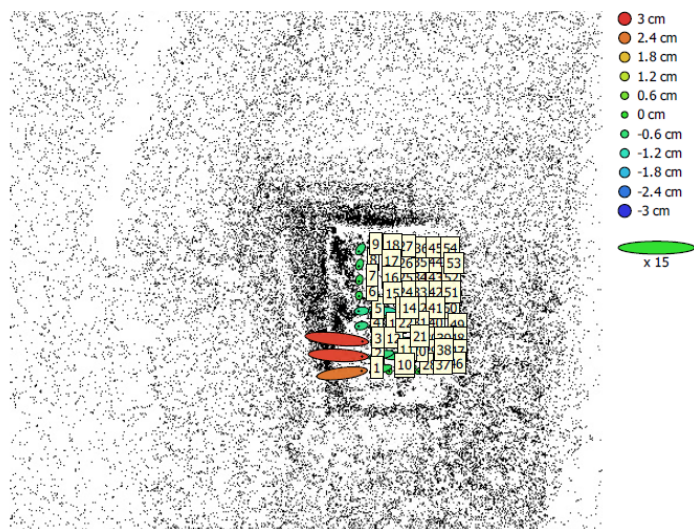
Figure 88- GCP locations and error estimates blue channel
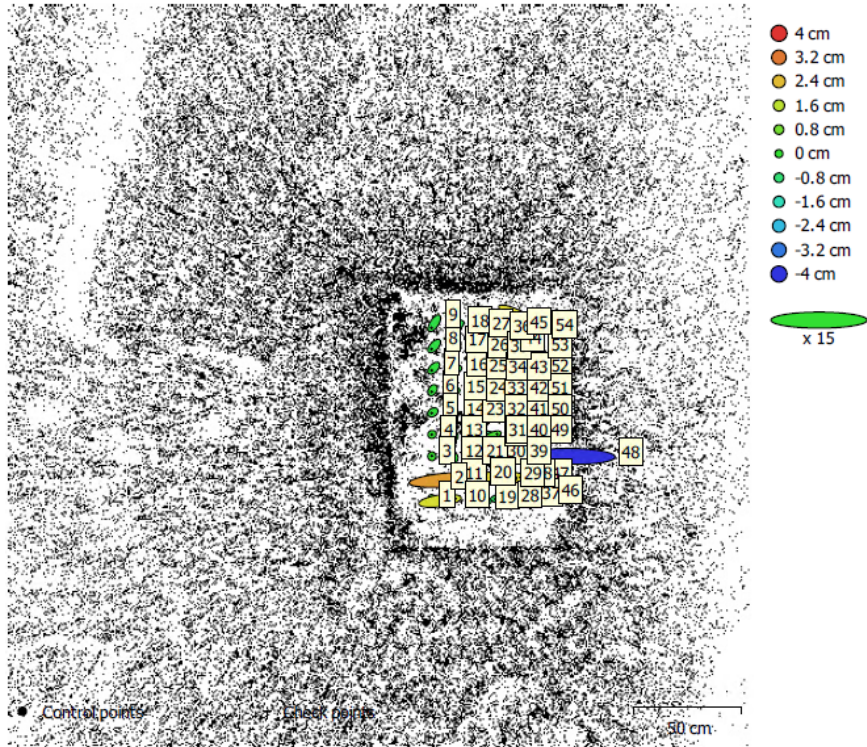
Figure 89 - GCP locations and error estimates red channel

Figure 90 - GCP locations and error estimates green channel

The next step is to calculate all camera parameters (f, c_x, c_y, k_1, k_2, k_3, k_4, b_1, b_2, p_1, p_2).

Comparing them, we obtain for the camera A:

	Blue channel	Red channel	Green channel
f [pixel]	5236.8	5258.3	5251.9
c_x [pixel]	-18.5	65.6	-7.9
c_y [pixel]	61.1	189.1	111.0
k_1	-0.0360312	-0.054719	-0.0433629
k_2	0.022099	0.0461191	0.0319431
k_3	-0.000996459	-0.0122075	-0.00547544
p_1	0.00251312	0.00507281	0.00238124
p_2	0.00358893	0.00764247	0.0049779
b_1	1.97869	5.3453	3.77515
b_2	-9.9818	1.02232	-8.5233

Table 33 - Distortion coefficients for each channel (camera A)

For the camera B:

	Blue channel	Red channel	Green channel
f [pixel]	5293.6	5305.8	5296.8
c_x [pixel]	-12.5	74.7	9.8
c_y [pixel]	61.9	191.8	105.6
k_1	0.0116123	0.00730554	0.0129144
k_2	-0.0513206	-0.0464711	-0.0534587
k_3	0.040197	0.0383037	0.0408212
p_1	0.00321137	0.00616674	0.00367986
p_2	0.00160398	0.0081511	0.00369452
b_1	4.0558	6.92328	4.62869
b_2	-11.626	-5.59257	-12.5834

Table 34 - Distortion coefficients for each channel (camera B)

14 pix   12 pix
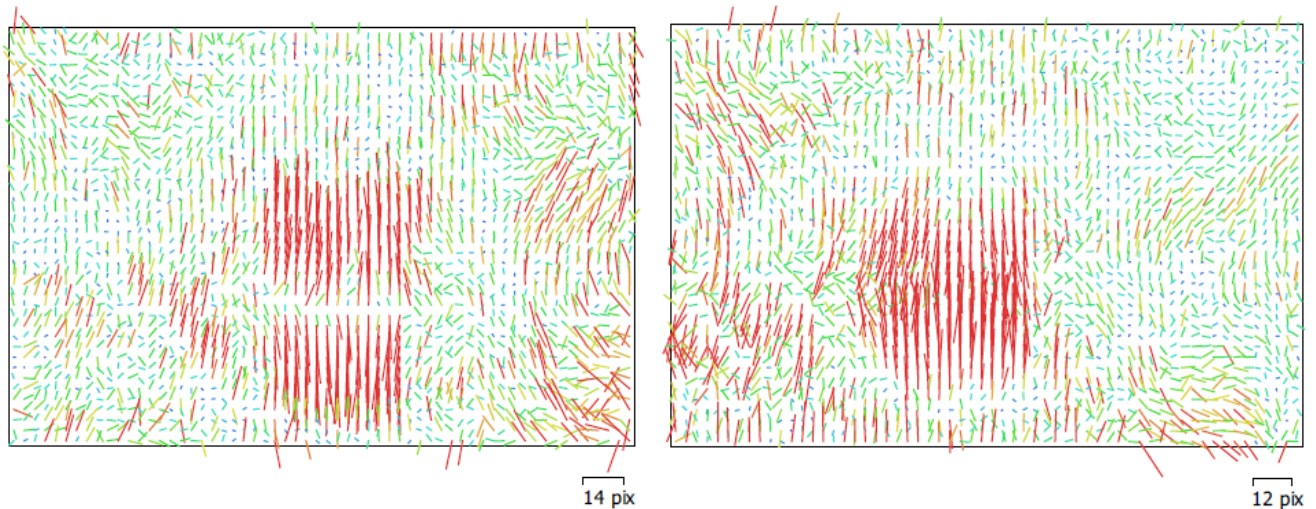
Figure 91 - Image residuals camera A (left) camera B (right) blue channel

132
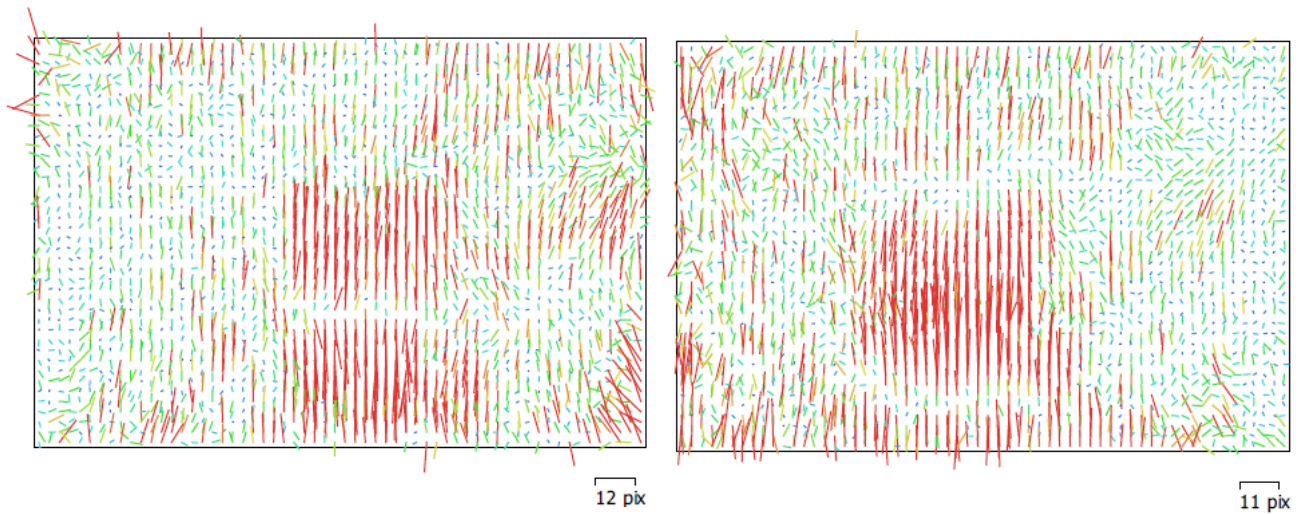
Figure 92 - Image residuals camera A (left) camera B (right) red channel
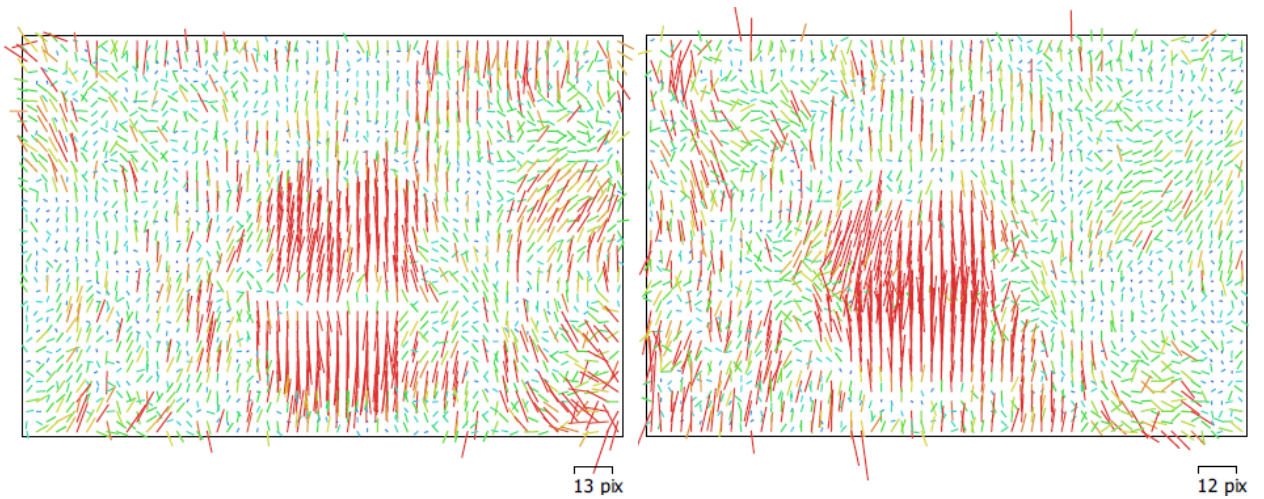
Figure 93 - Image residuals camera A (left) camera B (right) green channel

The last point to be made is about the 'Slave offset' parameters. By not imposing any limits, the software was able to rotate and translate the images freely, resulting in:

For blue channel:

	Adjusted	Sqm
x	0.342618	0.00217403
y	0.000306675	6.86895e-05
z	0.0251515	0.000248697

Table 35 - Slave offset output blue channel

133

For red channel:

	Adjusted	Sqm
x	0.3390	0.0027
y	0.0040	9.10707e-05
z	0.0265	0.0003

Table 36 - Slave offset output red channel

For green channel:

	Adjusted	Sqm
x	0.3393	0.0024
y	0.0019	7.02654e-05
z	0.0221	0.00024

Table 37 - Slave offset output green channel

The results obtained are different, the centre of take of the blue channel is 34 cm while for the other channels it is 33 cm.

As a final step, all images are exported and then merged using a code in Matlab (Appendix B).

The result obtained is not satisfactory, as the images are not superimposed correctly.
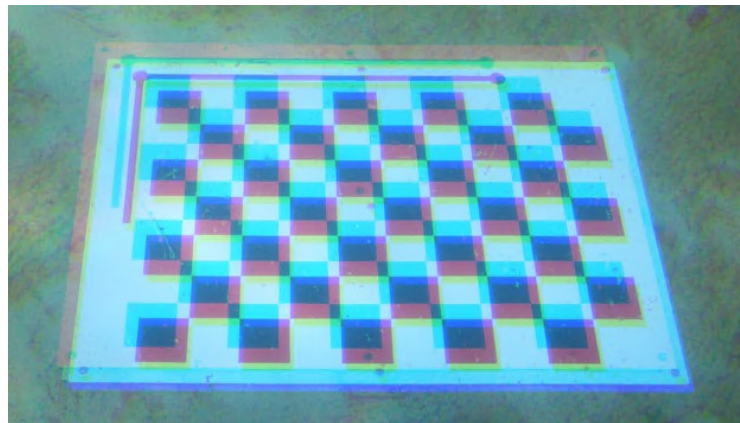
Figure 94 - Unified undistorted image

As can be seen in Figure 94, the different channels are shifted. This phenomenon is present because the undistorted images of the three RGB channels have very different coordinates of the main points, which causes the images not to be perfectly aligned during unification.

134

For camera A:

	Blue channel	Red channel	Green channel
c_x [pixel]	-18.5	65.6	-7.9
c_y [pixel]	61.1	189.1	110.9

Table 38 - Principal point coordinates camera A

For camera B:

	Blue channel	Red channel	Green channel
c_x [pixel]	-12.5	74.7	9.8
c_y [pixel]	61.9	191.8	105.6

Table 39 - Principal point coordinates camera B

6.1.3 Comparison of unconstrained processing results

After the analysis has been carried out, it is possible to make the necessary considerations as to which of its approaches is the most appropriate.

It can be seen that in this image dataset, the presence of distortions within the images is very evident.

Figure 95 - Comparison of original (left) and undistorted image (right)

It is possible to see the correction of distortions laterally.

As with previous processing and as shown in Figure 94, it is not possible to make a direct comparison as to which of the two approaches is best.

For this reason, when processing the survey, it is better to use the classical approach.

135

6.2 Application with constraints between the two cameras

6.2.1 Application on original dataset

The same number of images and the same parameters used in the previous section were used for this processing. The only constraint that was applied was to limit the x-axis translation of the images. This constraint was placed in the 'Camera calibration' tool in the 'Slave offset' group. An offset of 0.75 was set with an accuracy of 0.25, to allow the software to still make large movements.
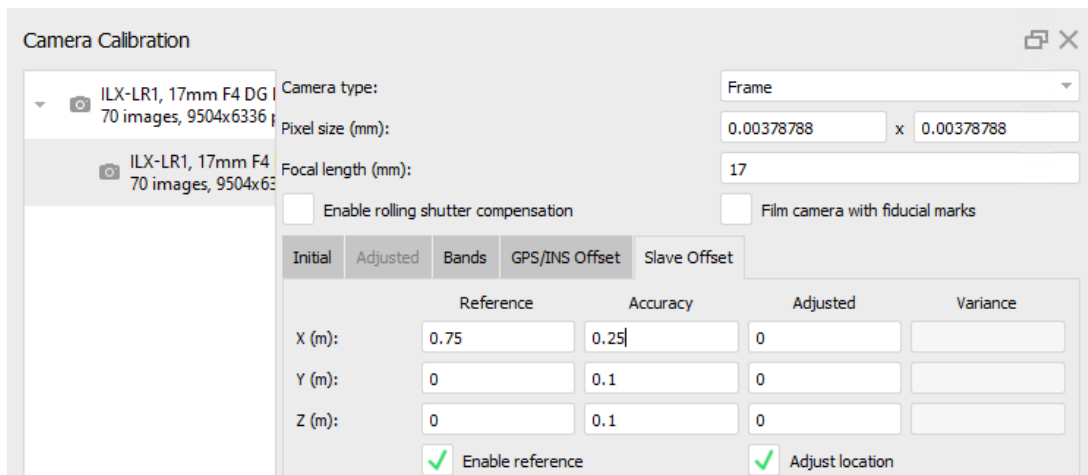
Figure 96 - Constraint in the camera calibration tool

There are 68/70 aligned images and it took only 43 seconds to complete the process.

Once all the steps explained in the previous paragraphs have been completed, we obtain the collimations for each point, which are:

Name	N° collimations	Name	N° collimations	Name	N° collimations
1	36	19	35	37	36
2	37	20	34	38	36
3	34	21	34	39	35
4	35	22	34	40	37
5	36	23	35	41	38
6	36	24	36	42	39
7	36	25	36	43	39
8	37	26	35	44	39
9	38	27	36	45	38
10	35	28	35	46	38
11	36	29	34	47	36
12	35	30	35	48	36
13	35	31	36	49	36
14	35	32	37	50	37
15	36	33	38	51	37
16	35	34	38	52	37
17	36	35	37	53	37
18	36	36	37	54	36

Table 40 - Number of collimations per point

It is necessary to check the errors obtained, to make sure there are no problems in our calibration. The average error obtained is 0.002 m, which is much lower than 0.4 cm.
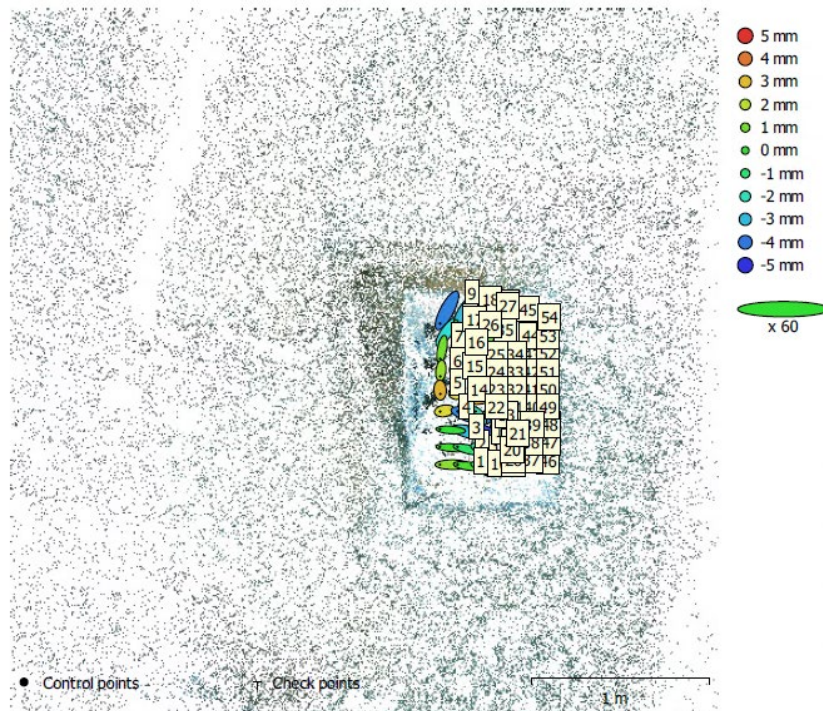
Figure 97 - GCP locations and error estimates

The next step is to calculate all the camera parameters (f, c_x, c_y, k_1, k_2, k_3, k_4, b_1, b_2, p_1, p_2).

The result obtained is for each camera:

	Camera A	Camera B
f [pixel]	5253.4183	5297.77388
c_x [pixel]	-5.67407	22.068
c_y [pixel]	109.373	99.8917
k_1	-0.0432495	0.0117169
k_2	0.0303681	-0.0528834
k_3	-0.00449246	0.0414856
p_1	0.00254722	0.0044503
p_2	0.00472266	0.00357976
b_1	2.63531	6.27314
b_2	-8.98253	-12.9544

Table 41 - Distortion coefficients for each camera

13 pix
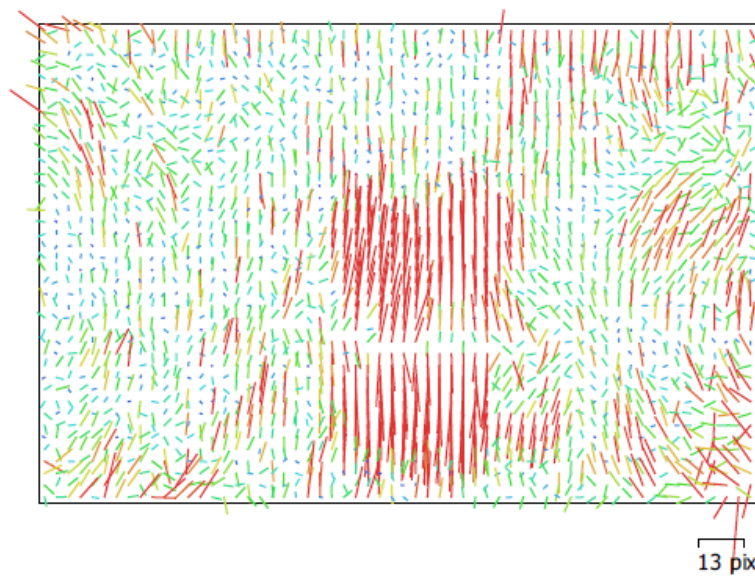
Figure 98 - Image residuals camera A
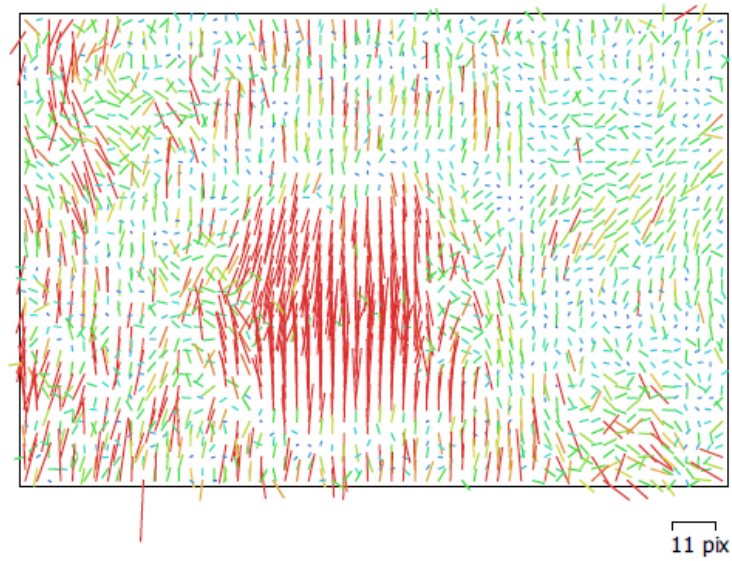
Figure 99 - Image residuals camera B

The last point to be made is about the 'Slave offset' parameters. By not imposing any limits, the software was able to rotate and translate the images freely, resulting in:

	Adjusted	Variance
x	0.3397	0.0025
y	0.00208704	6.71485e-05
z	0.0226	0.0002

Table 42 - Slave offset output

This means that the software calculated a distance between the gripping centres of 33,97 cm and a variation in y of 0.21 cm, which indicates that the cameras are not perfectly aligned.

6.2.2 Application on division of the dataset into channels

This last analysis takes up the division into RGB channels by adding the offset constraint, while the other parameters remain unchanged. The constraint placed is the same as in section 9.2.1.

Processing times are very similar here, the blue channel took only 37 seconds, the red 39 seconds, and the green 1 minute and 11 seconds. Even the number of aligned images are not the same for the different channels.

	Blue channel	Red channel	Green channel
Aligned images	68/70 couples	67/70 couples	70/70 couples

Table 43 - Aligned/total image for each channel

It can be seen that the green channel has the best result and the red channel the worst, although 96% of the images were also aligned for the red channel.

Once the coordinate file has been imported, it is possible to make initial considerations on point collimations.

For the blue channel:

Name	N° collimations	Name	N° collimations	Name	N° collimations
1	37	19	36	37	8
2	14	20	6	38	3
3	8	21	5	39	10
4	38	22	36	40	3
5	37	23	14	41	36
6	37	24	38	42	40
7	36	25	40	43	41
8	38	26	38	44	40
9	37	27	38	45	37
10	4	28	6	46	9
11	16	29	10	47	10
12	37	30	11	48	10
13	38	31	36	49	12
14	4	32	38	50	37
15	35	33	39	51	37
16	37	34	41	52	37
17	37	35	40	53	10
18	38	36	38	54	34

Table 44 - Number of collimations per point blue channel

For the red channel:

Name	N° collimations	Name	N° collimations	Name	N° collimations
1	34	19	7	37	7
2	9	20	5	38	6
3	36	21	34	39	5
4	36	22	35	40	3
5	36	23	37	41	34
6	37	24	36	42	34
7	36	25	35	43	33
8	36	26	35	44	32
9	36	27	34	45	31
10	7	28	6	46	5
11	34	29	6	47	6
12	34	30	36	48	3
13	37	31	35	49	16
14	37	32	35	50	33
15	36	33	36	51	33
16	36	34	34	52	34
17	35	35	33	53	32
18	34	36	32	54	14

Table 45 - Number of collimations per point red channel

For the green channel:

Name	N° collimations	Name	N° collimations	Name	N° collimations
1	5	19	11	37	12
2	7	20	6	38	12
3	4	21	11	39	11
4	35	22	10	40	37
5	36	23	35	41	38
6	36	24	35	42	38
7	36	25	35	43	39
8	37	26	36	44	39
9	38	27	35	45	37
10	6	28	12	46	12
11	5	29	12	47	11
12	5	30	11	48	12
13	34	31	36	49	36
14	34	32	35	50	37
15	36	33	36	51	37
16	34	34	37	52	37
17	36	35	37	53	39
18	36	36	35	54	37

Table 46 - Number of collimations per point green channel

It is necessary to check the errors obtained, to be sure that we have no problems in our calibration. Comparing the results:

	Blue channel	Red channel	Green channel
Mean error	0.0100 m	0.0103 m	0.0006 m

Table 47 - Mean error for each channel
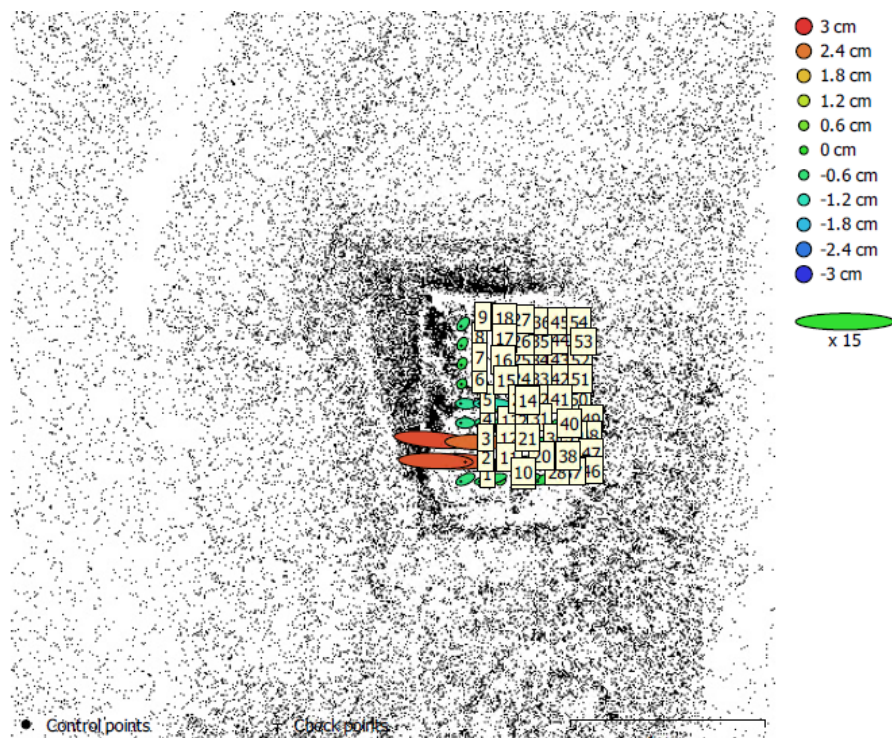
Figure 100 - GCP locations and error estimates blue channel

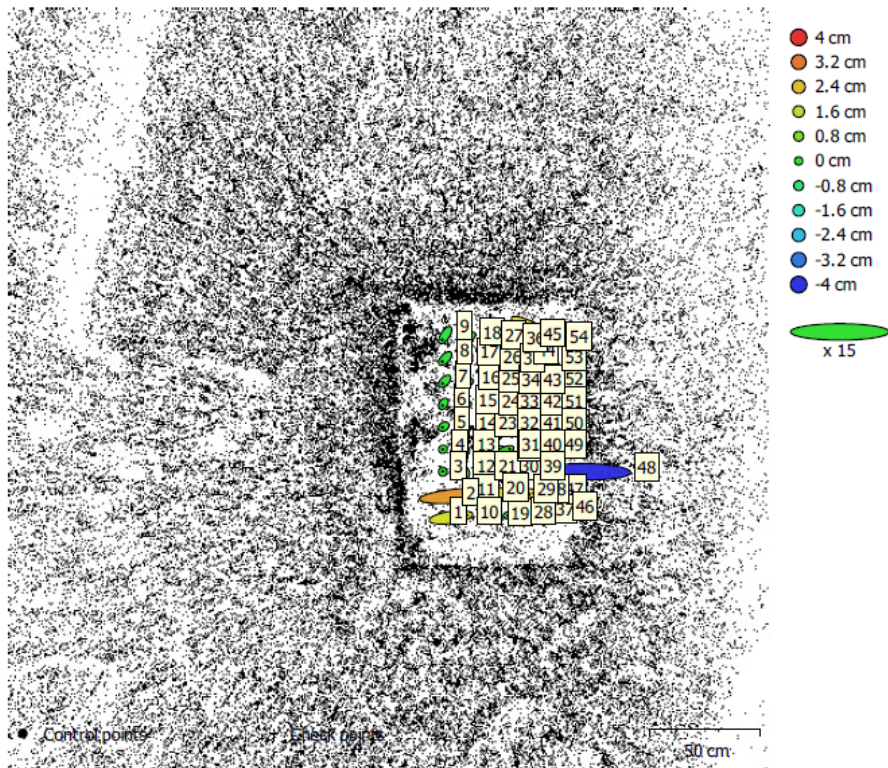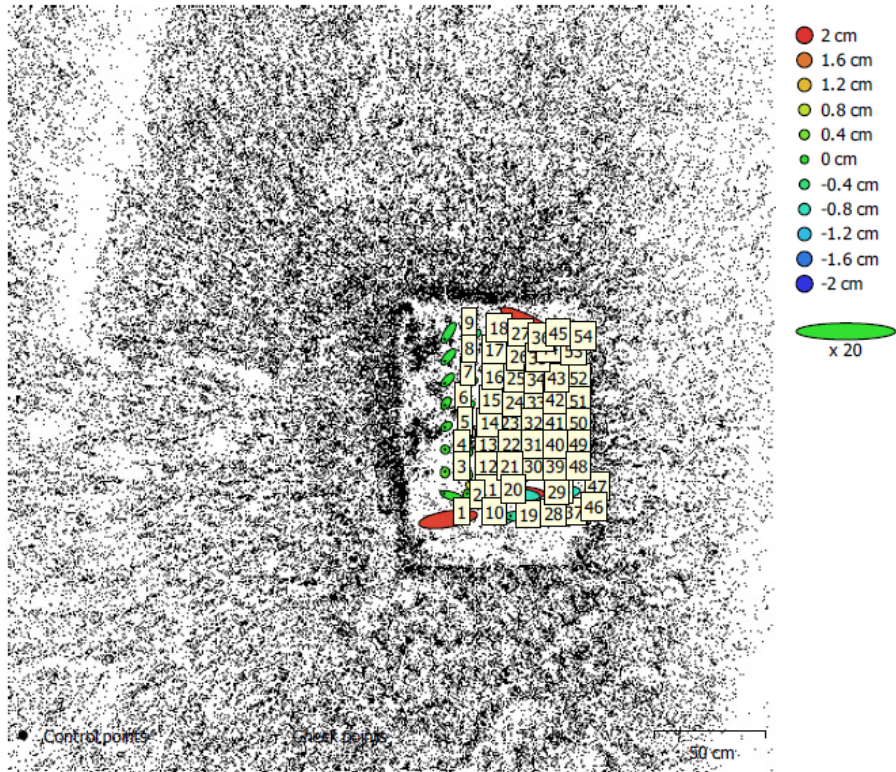*Figure 101 - GCP locations and error estimates red channel*
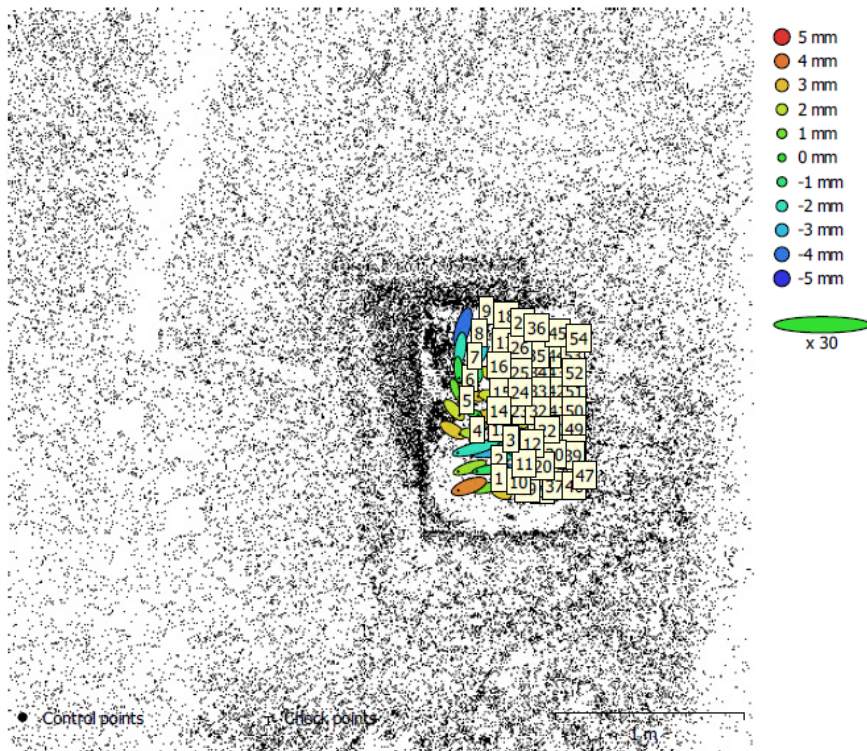
Figure 102 - GCP locations and error estimates green channel

The next step is to calculate all camera parameters(f, c_x, c_y, k_1, k_2, k_3, k_4, b_1, b_2, p_1, p_2)).

Comparing them, we obtain for the camera A:

	Blue channel	Red channel	Green channel
f [pixel]	5236.77409	5257.26496	5250.83125
c_x [pixel]	-18.5142	62.9866	-7.50398
c_y [pixel]	61.147	190.149	112.217
k_1	-0.0360312	-0.0548362	-0.0431495
k_2	0.022099	0.0461385	0.0315715
k_3	-0.000996459	-0.0122106	-0.00528193
p_1	0.00251312	0.00499333	0.00239621
p_2	0.00358893	0.00769142	0.00502396
b_1	1.97869	4.57094	3.83959
b_2	-9.9818	0.375215	-8.81846

Table 48 - Distortion coefficients and correlation matrix for each channel (camera A)

For the camera B:

	Blue channel	Red channel	Green channel
f [pixel]	5235.27653	5305.00418	5296.1837
c_x [pixel]	-18.2202	192.613	10.2441
c_y [pixel]	62.662	191.84	106.856
k_1	-0.0361529	0.00677093	0.0129068
k_2	0.0225311	-0.0455872	-0.0534474
k_3	-0.00127189	0.0377335	0.0408189
p_1	0.00249976	0.00607701	0.003693
p_2	0.00365135	0.00817826	0.00371891
b_1	1.97575	5.98898	4.86231
b_2	-9.8936	-6.34592	-12.874

Table 49 - Distortion coefficients and correlation matrix for each channel (camera B)

14 pix

12 pix
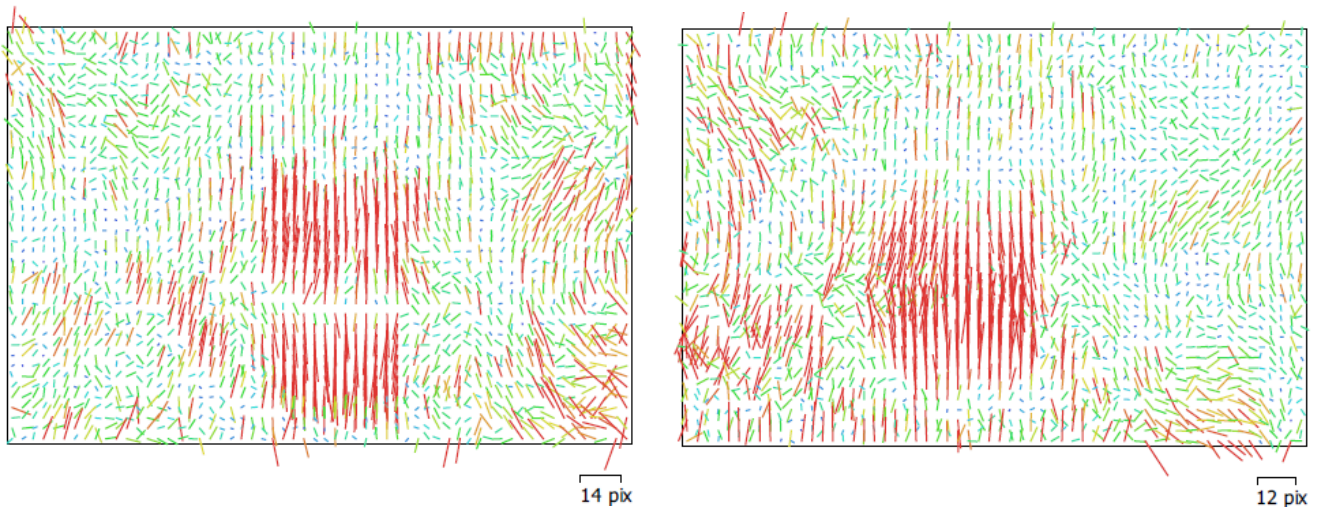
Figure 103 - Image residuals camera A (left) camera B (right) blue channel
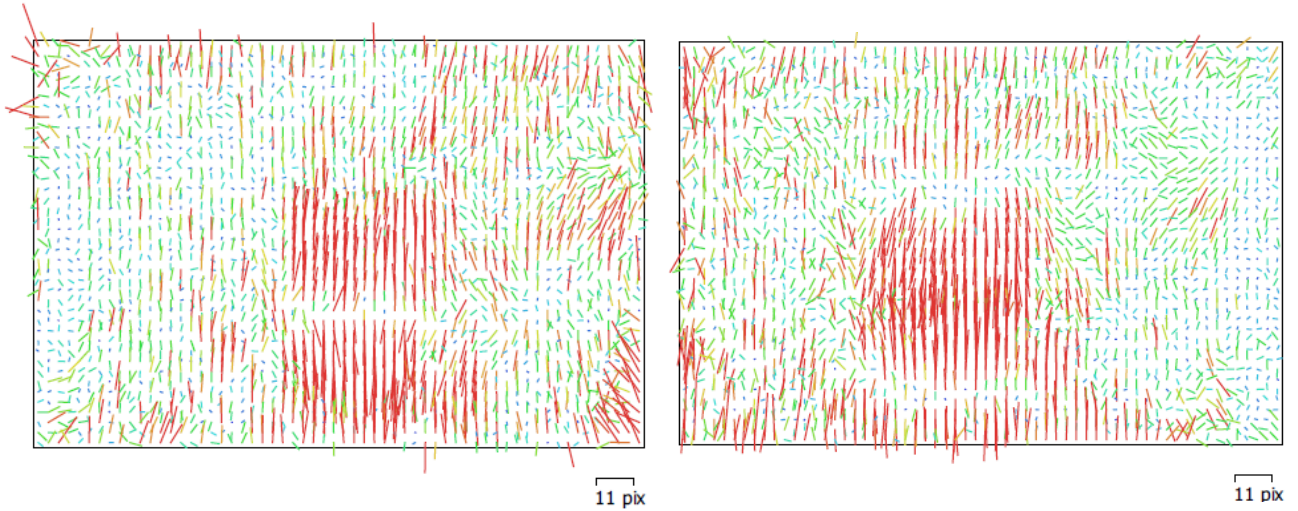
Figure 104 - Image residuals camera A (left) camera B (right) red channel
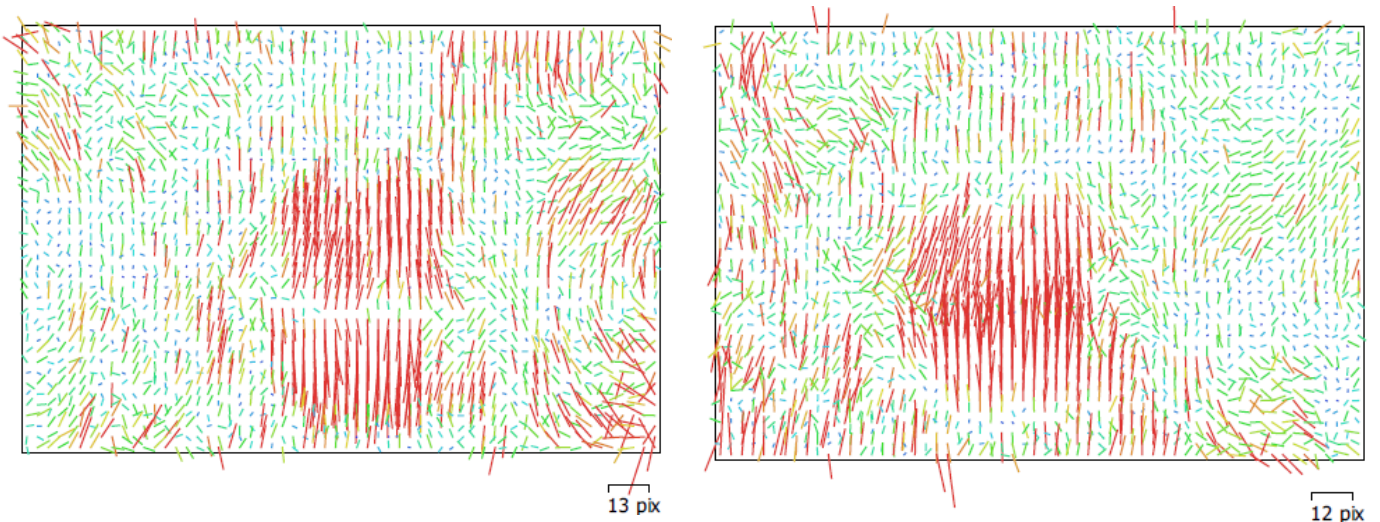
Figure 105 - Image residuals camera A (left) camera B (right) green channel

The last point to be made is about the 'Slave offset' parameters. By not imposing any limits, the software was able to rotate and translate the images freely, resulting in:

For blue channel:

	Adjusted	Sqm
x	0.3426	0.0027
y	0.0003	6.8228e-05
z	0.0252	0.0002

Table 50 - Slave offset output blue channel

For red channel:

	Adjusted	Sqm
x	0.3390	0.0027
y	0.0039	9.13868e-05
z	0.0265	0.0003

Table 51 - Slave offset output red channel

For green channel:

	Adjusted	Sqm
x	0.3393	0.0024
y	0.0019	7.0297e-05
z	0.0223	0.0002

Table 52 - Slave offset output green channel

In this case the results are very similar, if we round up to the centimetre all channels, we achieve an offset of 34 cm. So the result is acceptable at the moment.

As a final step, all images are exported and then merged using a code in Matlab (Appendix B).

The result obtained is not satisfactory, as the images are not superimposed correctly.
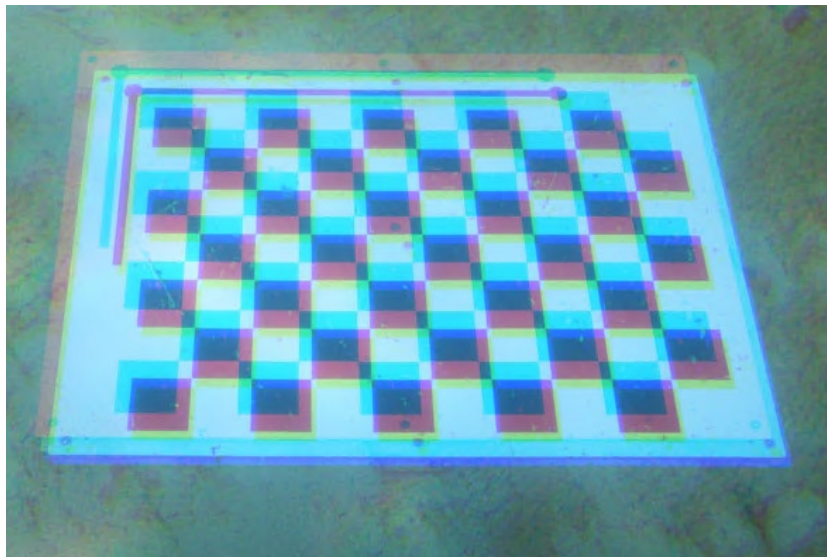
Figure 106 - Unified undistorted image

As can be seen in Figure 106, the different channels are shifted. This phenomenon is present because the undistorted images of the three RGB channels have very different coordinates of the main points, which causes the images not to be perfectly aligned during unification.

6.2.3 Comparison of constrained processing results

After the analysis has been carried out, it is possible to make the necessary considerations as to which of its approaches is the most appropriate.

It can be seen that in this image dataset, the presence of distortions within the images is very evident.
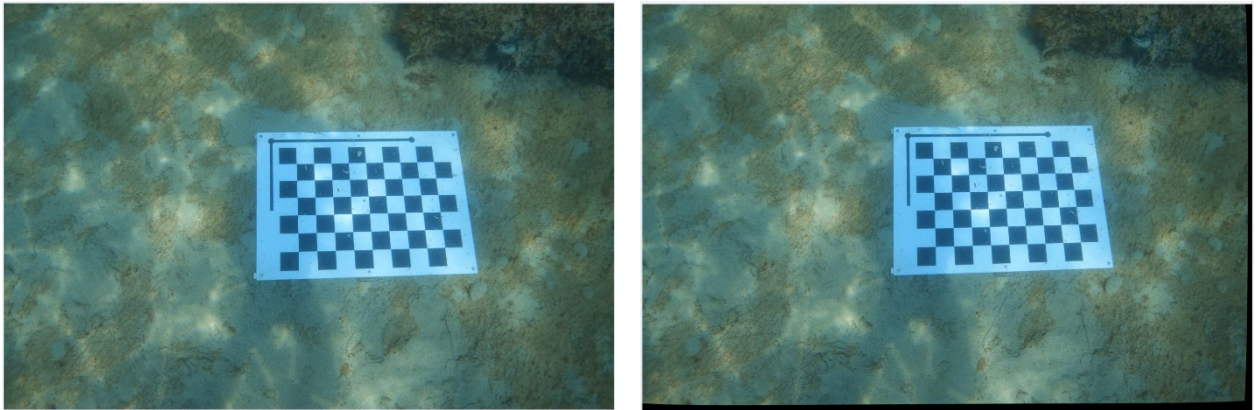
Figure 107 - Comparison of original (left) and undistorted image (right)

It is possible to see the correction of distortions laterally.

As with previous processing and as shown in Figure 106, it is not possible to make a direct comparison as to which of the two approaches is best.

For this reason, when processing the survey, it is better to use the classical approach.

6.3 Comparison of constrained and unconstrained processing results

Since the results from splitting the RGB channels cannot be considered acceptable, it is necessary to understand which approach, between the presence or absence of the

constraint, it is better to proceed with the processing of the entire dataset.

Comparing the 'Slave offset' parameters, we have:

	Adjusted (no constrain)	Sqm (no constrain)	Adjusted (with constrain)	Sqm (with constrain)	Delta adjusted
x	0.3397	0.0025	0.3397	0.0025	-0,000045
y	0.0021	6.7374e-05	0.0021	6.71485e-05	-0,000027
z	0.0225	0.000248697	0.0226	0.00025	-0,000113

Table 53 - Slave offset output and delta adjusted

Comparing the results obtained after collimation and calibration of the cameras, we obtain:

	without constrain	with constrain
Mean error	0.006838 m	0.00238

Table 54 – Mean errors comparison

The comparison shows that by imposing even a small constraint, there is an improvement in the calibration phase, in this case by 35% on the average error.
It is now possible to say which pre-calibration parameters will be used when processing the data.

	Camera A	Camera B
f [pixel]	5253.4183	5297.77388
c_x [pixel]	-5.67407	22.068
c_y [pixel]	109.373	99.8917
k_1	-0.0432495	0.0117169
k_2	0.0303681	-0.0528834
k_3	-0.00449246	0.0414856
p_1	0.00254722	0.0044503
p_2	0.00472266	0.00357976
b_1	2.63531	6.27314
b_2	-8.98253	-12.9544

Table 55 - Pre-calibration parameters

Chapter 7

Radiometric correction

Underwater images undergo radiometric variation in proportion to the depth at which they are acquired, as explained in section 7. In this section we will show a few different methods for colour correction. The first is the use of a filter already present within the Olympus camera, which automatically does a white balance and increases red tones. The second is the use of the ColourChecker and its software. Another one is using artificial lighting during the survey phase.

7.1 Olympus Auto Correction

To use the automatic colour correction of the Olympus camera, the 'Underwater' mode must be set. Once the survey is finished, it is possible to make a comparison between the acquired colours and the standard CIE94 colours [46]. A code in Matlab (Appendix C) and the help of ColourChecker was used to make the comparison. The software recognises the calibration panel and calculates the difference between the colours.
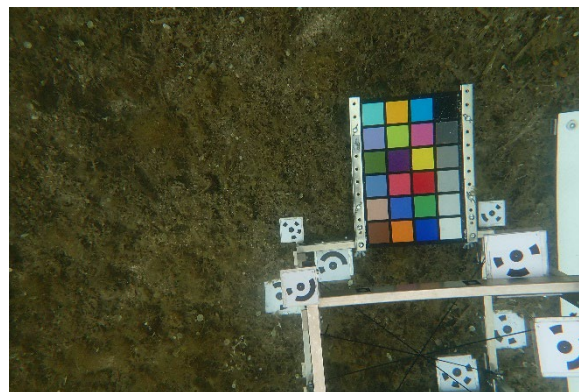
Figure 108 - Original Olympus camera image

The script measures the colour in each ROI and returns the measurements in a table, 'colourTable'. The intensity values measured for the eight main colours are:

	B	G	R	Y	M	C	W	B
R	1	84	178	210	183	35	200	33
G	50	142	1	178	71	135	200	30
B	184	106	68	86	159	221	227	54

Table 56 – Measured RGB for the eight main colours

The measurements of the colour difference in the variable ΔE in the table follow the CIE96 standard. The graph compares the colours detected in the image (centre) and the standard colours (border).
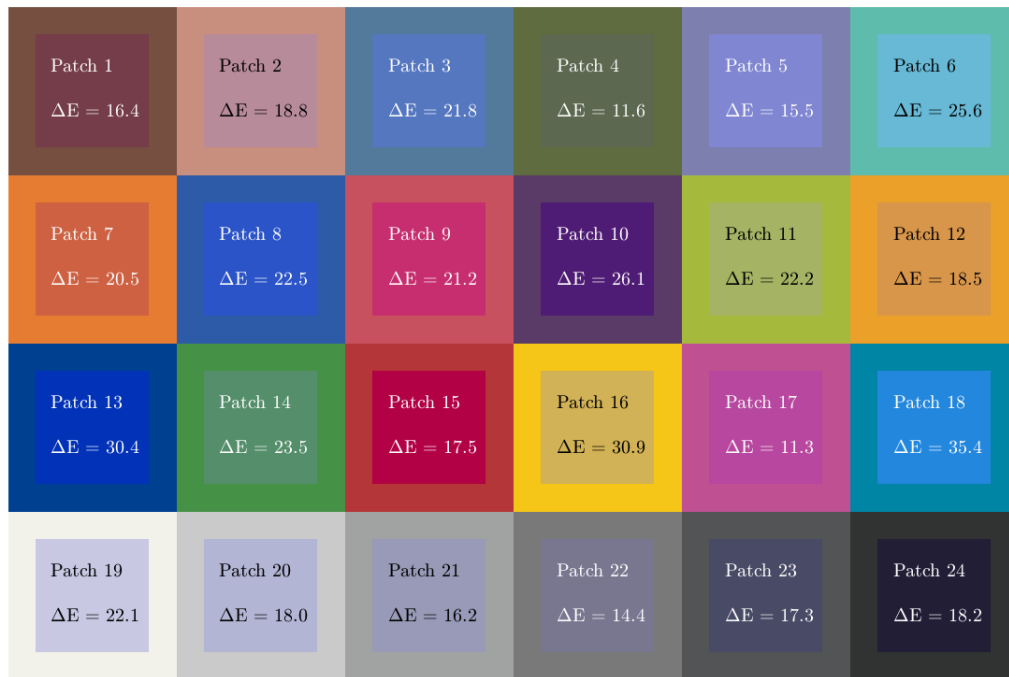
Figure 109 - Colour accuracy measurements of the Olympus

ΔE is calculated:

$$\Delta E = \sqrt{(L_2 - L_1)^2 + (a_2 - a_1)^2 + (b_2 - b_1)^2} \qquad (20)$$

where:

- L_1, a_1, b_1 are the LAB values of the reference colour;
- L_2, a_2, b_2 are the LAB values of the measured colour.

The closer ΔE is to zero, the more real the colour is:

- $\Delta E = 0$ means that the two colours are indistinguishable;
- $\Delta E < 1$ is generally considered imperceptible to the human eye.
- $1 < \Delta E < 2$ can be perceived by an experienced observer.
- $2 < \Delta E < 10$ is an obvious colour difference, visible even to the non-expert observer.
- $\Delta E > 10$ is an easily perceptible colour difference, often unacceptable in precision applications.

In this case there is a high difference in the colour cyan (35.4) while the colour with the smallest difference is magenta. This indicates that the automatic correction of the camera increases the red colour, but distorts the blue component a lot. It must be considered that no data can be entered within the camera, so it is a standard correction.

7.2 ColourChecker correction

The ColourChecker Classic is a radiometric correction panel. Its operation is simple: when surveying, simply place it close to the object of interest and photograph it. The image must then be processed with the panel manufacturer's software, 'ColourChecker camera calibration'. This software makes it possible to extract a colour profile with ΔE data inside.

The first step, in this case study, was to convert the image. The software used does not allow the reading of many formats, only Tiff, RAW and DNG. The images that were captured are in jpg and ORF format. Therefore, an Adobe tool was used to convert the image. Once the necessary extension was obtained, it was sufficient to import the image into the software.
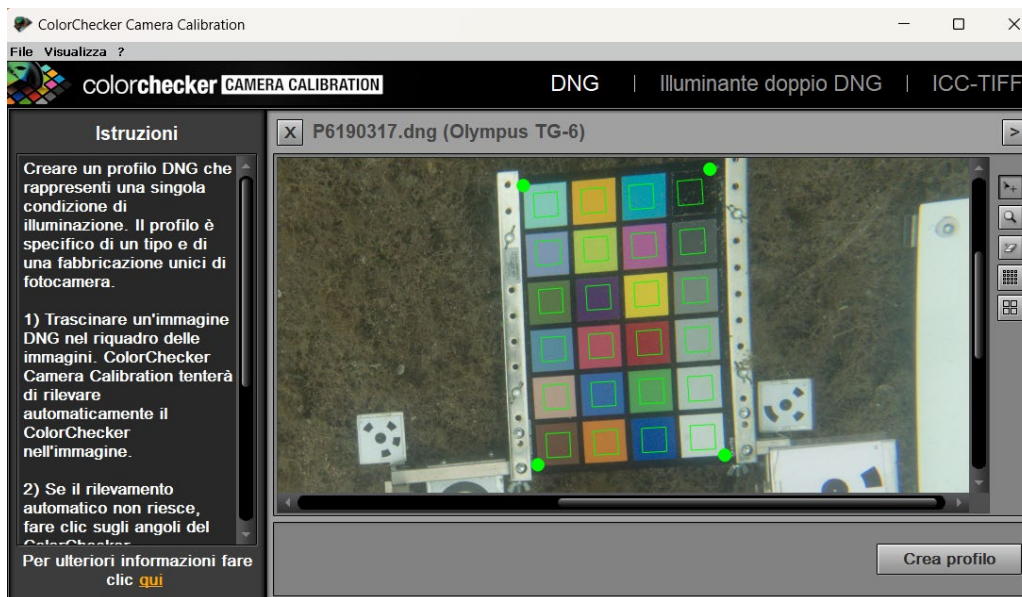
Figure 110 - Colour Profile Creation

Next, a colour profile is created with the dcp extension, which can be used in graphic software such as Lightroom Classic. The last step is to apply the colour profile to all images in the survey.

Figure 111 - Comparison of original image (left) and radiometric correction with ColourChecker (right)

At first glance, the image does not seem to have undergone any change, but if you look at the vegetation on the sides of the photo, you can see that the original vegetation is darker. Furthermore, a variation can be seen by analysing the colour histograms.

Figure 112 - Comparison of original histogram (left) and radiometric correction with ColourChecker (right)

Observing them, it can be seen that in both cases the predominance of blue and green colour is greater than red, but, in the histogram of the corrected image, there is a greater presence of red tones, so there is an improvement in the image.

Analysing the corrected image with the same methodology as in the paragraph before we obtain:

	B	G	R	Y	M	C	W	B
R	1	12	168	205	178	0	184	28
G	49	166	53	203	79	147	209	50
B	147	64	61	0	150	172	194	43

Table 57 – Measured RGB for the eight main colours

The values of ΔE for each colour result:

Patch 1 $\Delta E = 8.3$	Patch 2 $\Delta E = 15.6$	Patch 3 $\Delta E = 15.2$	Patch 4 $\Delta E = 17.1$	Patch 5 $\Delta E = 14.9$	Patch 6 $\Delta E = 8.9$
Patch 7 $\Delta E = 14.6$	Patch 8 $\Delta E = 9.5$	Patch 9 $\Delta E = 5.1$	Patch 10 $\Delta E = 9.0$	Patch 11 $\Delta E = 15.1$	Patch 12 $\Delta E = 17.4$
Patch 13 $\Delta E = 11.2$	Patch 14 $\Delta E = 17.3$	Patch 15 $\Delta E = 6.5$	Patch 16 $\Delta E = 15.3$	Patch 17 $\Delta E = 6.8$	Patch 18 $\Delta E = 8.4$
Patch 19 $\Delta E = 16.8$	Patch 20 $\Delta E = 14.3$	Patch 21 $\Delta E = 13.9$	Patch 22 $\Delta E = 15.4$	Patch 23 $\Delta E = 10.6$	Patch 24 $\Delta E = 11.1$
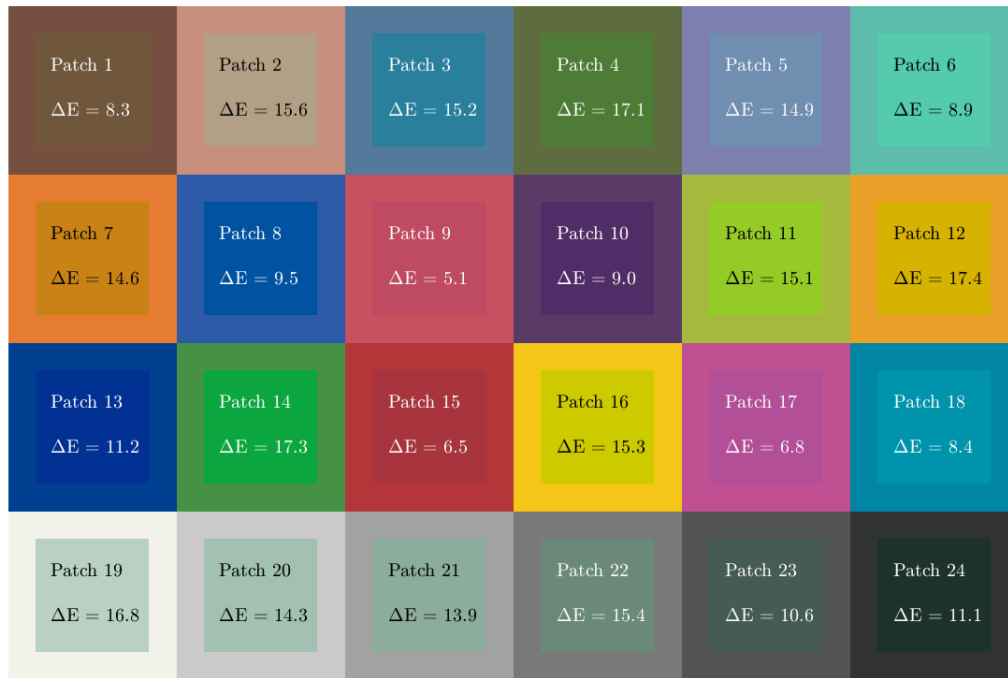
Figure 113 - Colour accuracy measurements of the Olympus with ColourChecker

In this case, there is a high difference in the colour yellow (15.3), while the colour with the smallest difference is pink (5.1). Looking at the other colours, it can be seen that the ΔE of red is very low, indicating an improvement in the image, as it is the first component to disappear with depth.

7.3 Artificial light

Artificial light was used during the survey at the columns in Porto Cesareo. Illuminating the survey object counteracts selective absorption. The intensity values measured for the eight main colours are:

	B	G	R	Y	M	C	W	B
R	14	103	144	238	199	14	174	26
G	77	205	54	198	136	212	213	53
B	255	126	63	43	252	255	231	63

Table 58 – Measured RGB for the eight main colours

The values of ΔE for each colour result:

Patch 1	Patch 2	Patch 3	Patch 4	Patch 5	Patch 6
$\Delta E = 14.4$	$\Delta E = 28.7$	$\Delta E = 33.0$	$\Delta E = 19.8$	$\Delta E = 29.8$	$\Delta E = 25.9$
Patch 7	Patch 8	Patch 9	Patch 10	Patch 11	Patch 12
$\Delta E = 10.4$	$\Delta E = 28.8$	$\Delta E = 23.8$	$\Delta E = 49.9$	$\Delta E = 13.3$	$\Delta E = 15.2$
Patch 13	Patch 14	Patch 15	Patch 16	Patch 17	Patch 18
$\Delta E = 51.7$	$\Delta E = 21.1$	$\Delta E = 18.7$	$\Delta E = 5.7$	$\Delta E = 40.0$	$\Delta E = 29.3$
Patch 19	Patch 20	Patch 21	Patch 22	Patch 23	Patch 24
$\Delta E = 22.4$	$\Delta E = 19.7$	$\Delta E = 23.5$	$\Delta E = 25.1$	$\Delta E = 27.2$	$\Delta E = 12.3$
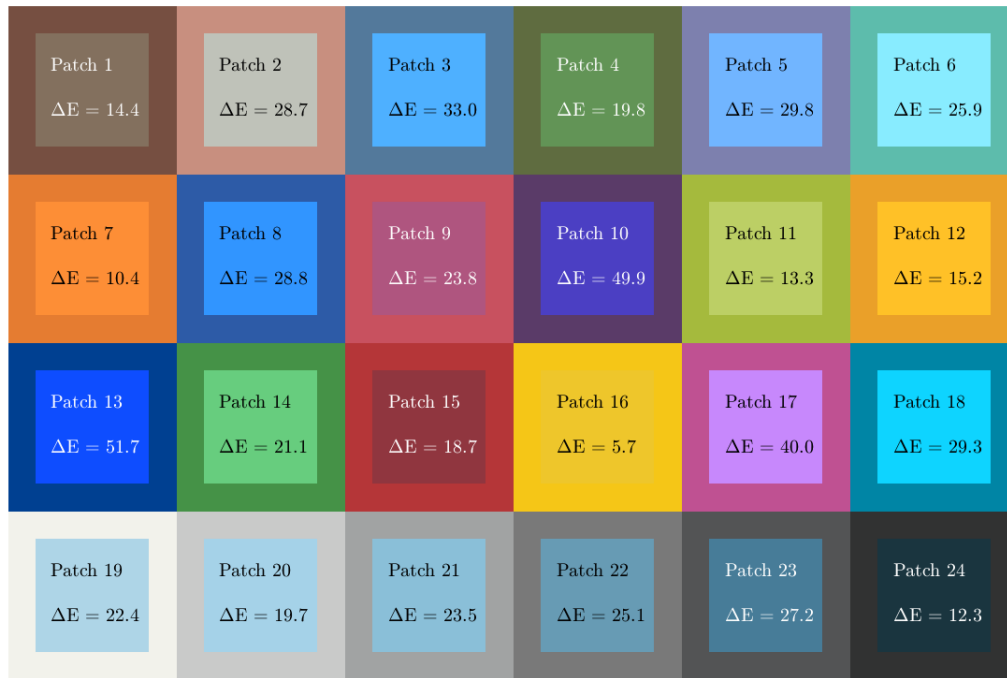
Figure 114 - Colour accuracy measurements of the Sony with artificial light

In this case, there is a high difference in the colour violet (49.9), while the colour with the smallest difference is yellow (5.7). Looking at the other colours, it can be seen that the ΔE of red is high, indicating that the presence of illumination increases the red hue, even making it excessive.

7.4 Matlab correction

With the help of Prof. Andrea Lingua, Matlab's code (appendix C) was implemented by adding a part where it is possible to correct the image directly on the software, without using external platforms (appendix D). By summarising the first part of the code, it is possible to see how the image is read and the radiometric calibration panel is detected. Then the LAB values representing the correct colours are extracted, the RGB colours of the calibration panel are extracted and 'measuredLab' is used to convert the measured values from RGB to LAB using the standard white point 'd50'.

Three different graphs are then shown. The crosses in cyan are the comparison of luminance values between the detected and measured LAB values(l), in red the values of the green/red component (a) and in blue the blue/yellow components (b).
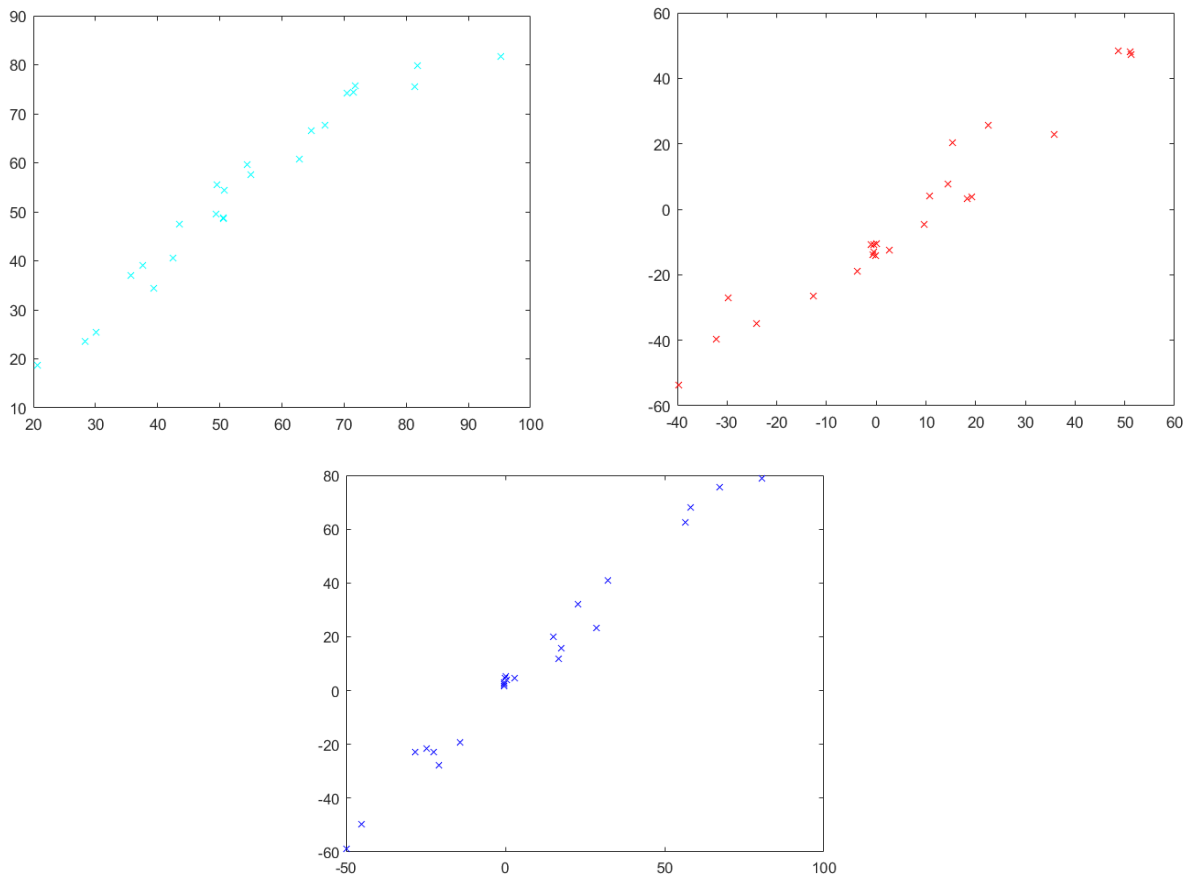
Figure 115 - Graphs for the comparison of luminance values between the detected and measured Lab values(l) in cyan, in red the values of the green/red component (a) and in blue the blue/yellow components (b).

It can be seen that all the graphs do not have a constant trend, so they cannot be described with a simple linear function

In the following steps, the image is loaded again and converted to LAB values. A 'for' loop is created through each pixel of the loaded image. In this double loop, the 'a' and 'b'

components are corrected for each pixel. To make this correction, an interpolating function is created using the values from the previous graphics.

As a final step, the image is corrected by applying the corrections calculated in the double 'for' cycle and displayed in a new image.

It can be seen that the corrected image produced is not perfect, there are areas where errors (black spots) are present.

Figure 116 - Comparison between image corrected with Colorchecker (left) and Matlab (right)

In addition, a comparison between the corrected image and the image corrected with the colourchecker shows that there is a greater red component. This is a first approach of the colour correction that has been applied to Matlab for this project, the result is not optimal, but there is good room for improvement. The final goal is to develop a code that allows, in total autonomy, a correct radiometric calibration of the images.

Chapter 8

Case study of the columns of Porto Cesareo

A survey campaign was carried out in July 2024, coordinated by the DIATI and DAD departments of the Politecnico di Torino and in collaboration with the Department of CH of the University of Salento. The activities took place in Porto Cesareo marine protected area.

Figure 117 - Site location

The object of the survey is a shallow archaeological site where there are five columns half-covered by the seabed that are assumed to derive from the sinking of a boat in the Roman/pre-Roman period during a trade route.

The site is excellent for carrying out various tests with the technologies we have discussed, as it is located not far from the coast, at shallow depths and there are no particular sea currents or other criticalities.

Several analyses will be shown in this section, the first a stereographic processing, the second a processing without the use of pre-calibration parameters, shown in the previous section, while the third will be done using these parameters from the beginning. The expected result is an improvement between the first and second processing

8.1 Case study with stereographic system

The first analysis is to test the data derived from Sony cameras, as a stereographic system. The steps are those of classical photogrammetry. Already in doing image alignment there turn out to be problems as little more than half of the images had been aligned, but more importantly the depth map produced turned out to be curved.

The obtained alignment was discarded and a second one was made, but with low density. Once finished, since the result was acceptable, a second alignment was made with medium density, but without resetting the previous one. This caused the software to align more images and create a correct depth map, aligning a total of 617 images, but some of them do not appear to be in the correct position.

Next the point cloud was created, with medium density, again there were significant critical issues, first of all the time it took to create the dense cloud, 10 hours and 37 minutes. Upon completion it created a cloud containing 241,543,125 points, but it turned out to be extremely unclean and co significant misalignments.

Figure 118 - Point cloud with noise and misalignments

The same procedure was done by entering the pre-calibration parameters, but the result did not improve.

The causes for this may be multiple. One can assume that there was a problem with the synchronization of the system in the long run, since the first images acquired, the ones used for calibration in the previous chapters, turn out to be perfectly synchronized and have no problems. It was possible to see that as time progresses, the number of images that were discarded, because they did not belong to a photo pair, increased significantly.

For this reason, a different approach was chosen.

8.2 Case study without pre-calibration

For the reasons explained in the previous chapter, a different approach was chosen, namely, to use acuisite images with the stereographic system but to analyze them as single cameras.

The process used is the classical process of photogrammetry. The alignment of the images was done with the same parameters used so far. There are 1394 imported images of which 1379 have been aligned.

Since no footholds were acquired during the survey phase, the point cloud from Alessio Calantropio's [17] work was used. Since the marine environment undergoes considerable changes over time, the seabed was removed from the point cloud in order to obtain a better result at the end of the process. The reference cloud is georeferenced, they were both imported into 'CloudCompare' and an initial rototranslation was done. Next, an ICP procedure was performed, which by means of its algorithm allows the distance between the two clouds to be minimised. The step is very simple and intuitive.
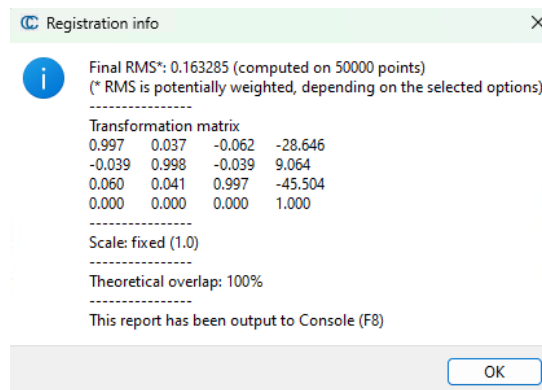
Figure 119 – RMS and transformation matrix

The output result is RMS (Root Mean Square), which is 0.16. Also present is the transformation matrix, inside which are the values of the rotations, translations and scaling performed. The diagonal contains the scaling and rotation values along the x, y and z axes. The values in the last column represent the translation applied along the axes and the remaining values indicate the extent of the rotations.
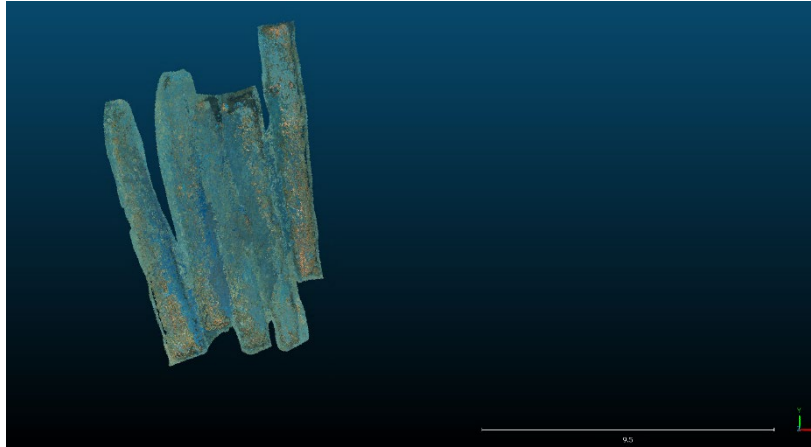
Figure 120 – Point Cloud on CloudCompare

8.3 Case study with pre-calibration

In this case study, the pre-calibration parameters obtained in the previous paragraphs will be applied. They were applied as early as the camera alignment stage, in order to have a complete comparison between this case study and the one presented in the previous subchapter.

Once the images are imported, it is necessary to split the data into the two different cameras utlized. The software is unable to do this automatically since the cameras have the same characteristics, so manual action must be taken for the division. Two groups, A and B, are created.
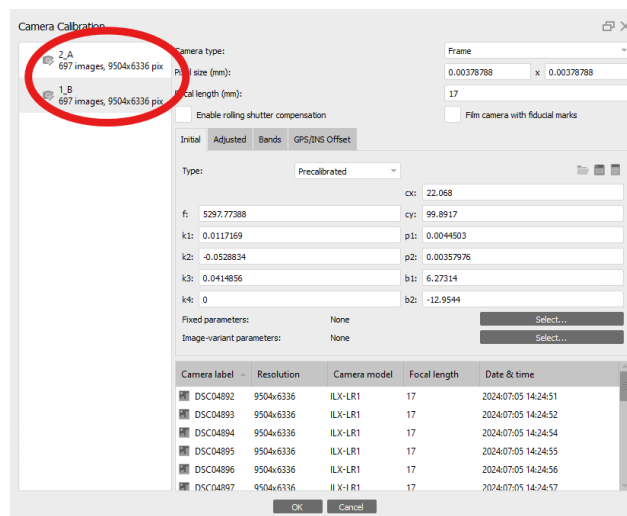
Figure 121 – Division of cameras

This division is necessary because each camera has different pre-calibration parameters, which allows for correct data entry.

There are 1394 imported images and 1379 were aligned, the same amount as the previous processing. Like the previous case, the seabed was removed and the ICP was done. Obtaining this result:
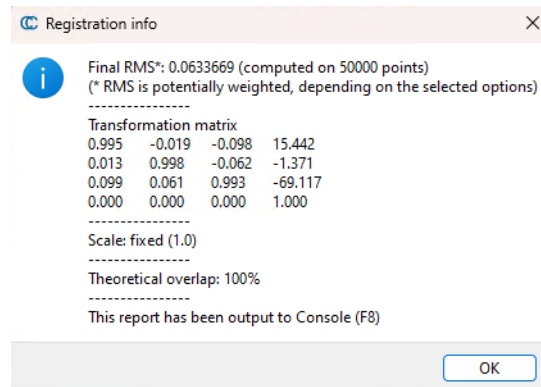
Figure 122 – RMS and transformation matrix

For this point cloud too, we proceeded via 'CloudCompare' by doing an initial alignment and then the ICP. The results obtained are different. The obtained RMS value is 0.063, which is lower than the one previously shown. This indicates that this cloud is better, as a lower RMS means better overlap.

Thanks to the results we can say that, as expected, the inclusion of pre-calibration parameters at the beginning of the procedure allows an improvement in the data. Once this is achieved, it is possible to import the scaled and rotated the point cloud into Metashape and continue with the processing in order to create and export the final results.

Figure 123 – Point Cloud on CloudCompare

8.4 Final case study

Once the correct procedure is understood, the georeferenced cloud is imported back to Metashape, can be created the mesh and orthophoto of the site can be processed.

A textured mesh was created, which is a mesh of triangles to which an image is applied that defines the colours, light and details of the surface. The mesh produced has 16.717.391 faces and 8.373.567 vertices. The processing time was 1 hours and 5 minutes.
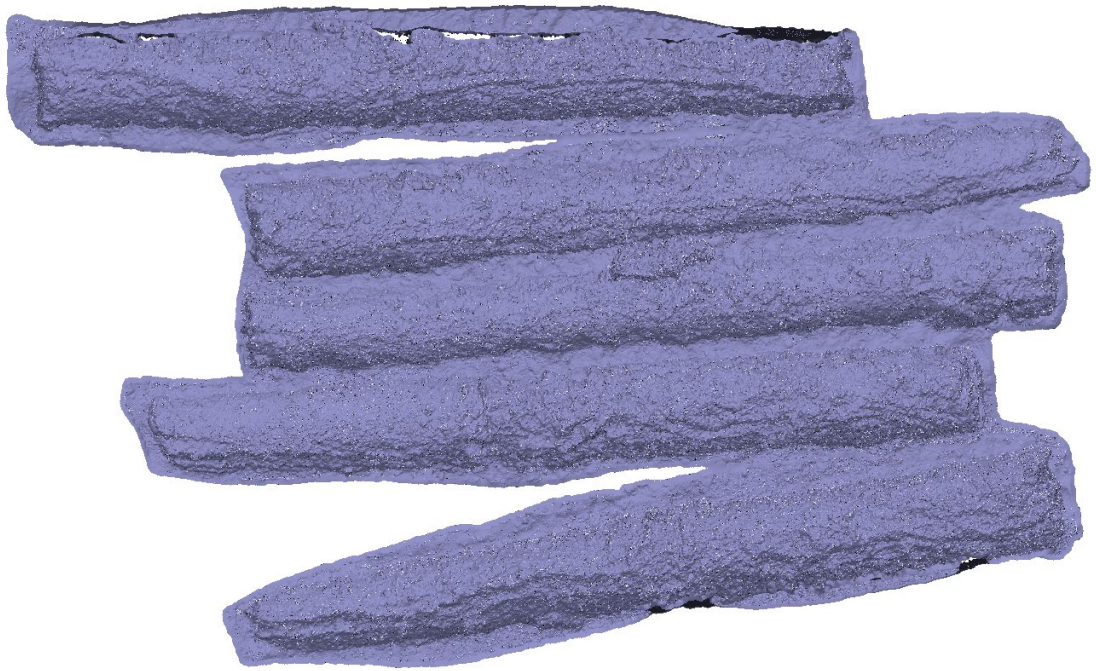
Figure 124 – Final mesh in wireframe view

Figure 125 – Final texture mesh

Lastly, the orthophoto, a geometrically corrected image, was created. The processing time was 3 hours and 20 minutes, with a pixel size of 0.001x0.001.

Figure 126 – Final orthophoto

All deliverables can be found in Appendix H.

In order to contextualise the orthophoto created, an overlay was made between the orthophoto of the coastline processed by Alessio Calantropio [17] and the one created during our processing.
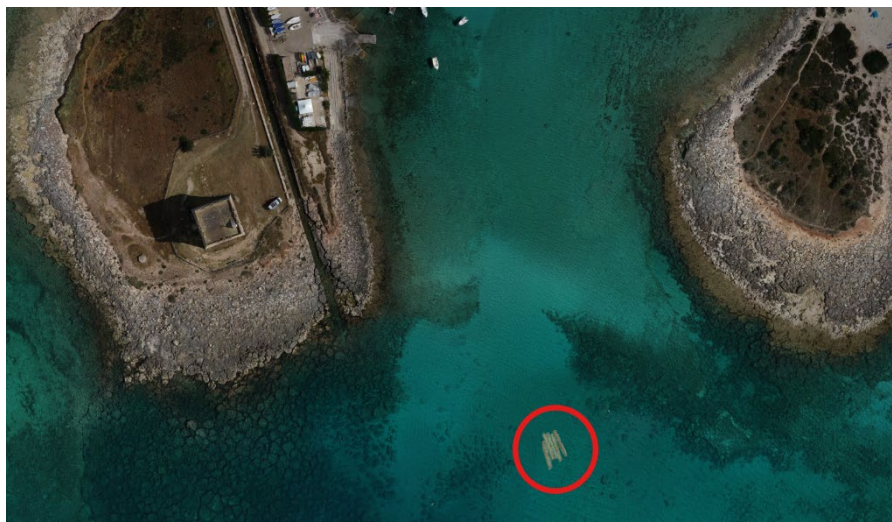
Figure 127 – Final orthophoto in the context

Conclusion

In this thesis, we set out to understand some of the best approaches for underwater surveying in order to make underwater cultural assets more accessible.

The analysis focused mainly on the geometric calibration phase of the camera and the radiometric calibration.

For the geometric calibration, we analysed different types of analysis. We diversified the approaches, one by analysing the different RGB channels, the other by analysing the raw data without any alteration. We could see that splitting the RGB channels resulted in an improvement of the images by reducing radial distortions.

The second analysis was made on the stereoscopic images, again the dual approach was used, but it did not produce the expected results as it was not possible to make a direct comparison between the data obtained from the analysis of the RGB channels and that on the raw data. This is due to the fact that when merging the RGB channels after calibration, the values of the grip centres were too different from each other and created a channel shift when merging the data.

A few considerations must be made about the stereographic system that has been presented. Unfortunately, it turns out not to be well synchronised, which means that during the survey phase, sometimes one of the two cameras did not take a picture and the pair was then discarded. This repeated event over time means that either data is lost or more strip have to be taken to obtain a homogeneous and correct survey. Increasing the number of strip is a negative aspect, as underwater surveys present certain problems for the operator, so it is better to try to acquire the best data in the shortest possible time.

169

The third analysis presented is the radiometric analysis. As presented in the previous chapters, the deeper one goes, the more the phenomenon of selective absorption is present. In the analyses presented, the correction was not so pronounced because the depth was not great.

This means that the deeper the object is, the more attention must be paid to the correction techniques. The colourchecker is an excellent tool for this type of analysis, with the disadvantage that it must be replaced every 6 months in order to always have a good result. The development of AI and NeRFs, on the other hand, makes it possible to have a fast and effective tool, its downside is that, like all technologies, it must be implemented to make the return of the data as truthful as possible.

Another issue related to radiometric correction and the use of the colourchecker is that RAW data are required. This causes the data acquisition time to increase by a few seconds, due to the time required to store the data in the camera. Using only JPG formats, even at the highest quality, it does not allow for proper image correction. As the acquisition time increases, attention must be paid to the speed at which one moves between shots, as the overlap necessary for a successful photogrammetric process may not be respected.

The entire research is part of the Archimedes project, whose aim is to enhance the value of Underwater Cultural Heritage.

The work shown in this dissertation is only the first step towards enabling everyone to safely enjoy the submerged heritage. Figuring out the best way to acquire the data will not only make it possible to make these cultural assets available to all people in the future, but it will also be possible to make the experience unique, through high quality three-dimensional models that can fully involve the user.

In addition, it is important to emphasise that a functional and correct data acquisition allows a safer environment for the surveyor. The underwater world is a unique place, but attention must be paid to many factors, on which the human cannot intervene. Therefore,

the more confident an operator is with the whole surveying procedure, the safer operators will be.

The long-term aim of Archimedes is to create a database, within which all data related to the submerged heritage can be found. This requires the collaboration of several professionals, who are able to understand, map and analyse the finds in its entirety. This is why figures such as archaeologists, architects and engineers converge in this project. Fully understanding a find is necessary, not only for its valorisation, but also for its conservation.

The mapping of these assets will make it possible to promote a tourism that is growing rapidly, the underwater one. This is because assets cannot always be brought back to the surface, as their degradation may increase considerably, so it is important to train people who are able to show these assets where they are located.

This project has great potential for growth, as our coasts and seas are rich in artefacts that have already been found and studied and many more that are waiting to be discovered.

Acknowledgements

At the end of this thesis, which represents the crowning achievement of my training at the Politecnico di Torino, I would like to say a few words for all those who have supported me over the last few years and beyond.

First of all, I would like to express my gratitude to my lecturers who have been instrumental in this thesis. I thank Professors Andrea Maria Lingua and Filiberto Chiabrando for sharing their experience with me throughout these academic years. I also thank them for the opportunities they gave me that allowed me to grow professionally and academically. I also thank Dr Francesca Matrone for her presence during this journey. I would also like to thank Edward Borgogno, who was always available for clarification and help.

Thanks to the company Biru S.r.l Agricola who kindly hosted us during the data acquisition phases for the Poseidon project.

I would also like to thank Dr Alessio Calantropio of the University of Sassari, for his willingness to share the data obtained during his PhD and for the help he gave me during some of the most difficult moments in the writing of my thesis. I would also like to thank him for the passion he has transmitted to me over the years for this subject, and for allowing me to learn more about it, enriching me professionally.

Desidero alla fine di questa tesi, che rappresenta il coronamento del mio percorso di formazione al Politecnico di Torino, spendere due parole per tutti coloro che mi hanno sostenuto in tutti questi ultimi anni e non solo.

Innanzitutto, rivolgo la mia gratitudine ai miei relatori che sono stati protagonisti di questo percorso di tesi. Ringrazio i professori Andrea Maria Lingua e Filiberto Chiabrando per aver condiviso con me la loro esperienza durante tutti questi anni accademici. Li ringrazio anche per le opportunità che mi hanno dato che mi hanno permesso di crescere professionalmente e accademicamente. Ringrazio anche la dottoressa Francesca Matrone per la sua presenza durante questo percorso. Ci tengo anche a ringraziare Edward Borgogno, sempre stato disponibile per chiarimenti e aiuti.

Grazie all'azienda Biru S.r.l Agricola che durante le fasi di acquisizione dati per il progetto di Poseidon ci ha gentilmente ospitato.

Un grazie al dottor Alessio Calantropio dell'Università di Sassari, per la disponibilità nella condivisione dei dati ottenuti nel suo percorso di dottorato e per l'aiuto che mi ha fornito in alcuni dei momenti più ostici nella stesura della tesi. Inoltre ci tengo a ringraziarlo per la passione che mi ha trasmesso in questi anni per questo argomento, e per avermi permesso di apprenderlo più a fondo arricchendomi professionalmente.

References

[1] N. O. and A. A. US Department of Commerce, «NOAA's National Ocean Service». Consultato: 19 settembre 2024. [Online]. Disponibile su: https://oceanservice.noaa.gov/

[2] «Home page», IPCC - Focal Point Italia. Consultato: 19 settembre 2024. [Online]. Disponibile su: https://ipccitalia.cmcc.it/

[3] UNEP, «Lanciato un nuovo quadro per monitorare i progressi sulla biodiversità delle barriere coralline». Consultato: 19 settembre 2024. [Online]. Disponibile su: https://www.unep.org/technical-highlight/new-framework-launched-track-progress-coral-reef-biodiversity

[4] «Plastic waste inputs from land into the ocean | Science». Consultato: 19 settembre 2024. [Online]. Disponibile su: https://www.science.org/doi/10.1126/science.1260352

[5] R. Auriemma Alberti e F. Chiabrando, «PRIN: PROGETTI DI RICERCA DI RILEVANTE INTERESSE NAZIONALE – Bando 2022».

[6] M. A. Lingua, «multitemPOral SEagrass mapping and monitoring of posIDONia meadows and banquettes for blue carbon conservation (POSEIDON)». 2022.

[7] UNESCO General Conference, «Recommendation on international principles applicable to archaeological excavation». 1957.

[8] The General Conference of the United Nations Educational, Scientific and Cultural Organization, «Convention Concerning the Protection of the World Cultural and Natural Heritage.» 1972.

[9] The Third United Nations Conference on the Law of the Sea, «United Nations Convention on the Law of the Sea.» 1982.

[10] International Committee for the Management of Archaeological Heritage (ICAHM), «Charter for the Protection and Management of the Archaeological Heritage.» 1990.

[11] Council of Europe, «European Convention on the Protection of the Archaeological Heritage, vol. No. 143». 1992.

[12] Università di Milano"Bicocca" (Dipartimento Giuridico delle Istituzioni Nazionali ed Europee), Regione Siciliana (Assesorato dei Beni Culturali ed Ambientali e della Pubblica Istruzione), and Università degli Studi di Palermo, Facoltà di Economia (Istituto di Diritto del Lavoro e della Navigazione), «Siracusa Declaration on the Submarine Cultural Heritage of the Mediterranean Sea.» 2001.

[13] «Convenzione sul patrimonio culturale subacqueo 2001 | UNESCO». Consultato: 23 settembre 2024. [Online]. Disponibile su: https://www.unesco.org/en/underwater-heritage

[14] Council of Europe, Directorate of Democratic Governance, DG II, Managing Diversity Division, «Framework Convention on the Value of Culturale Heritage for Society.» 2011.

[15] International Council on Monuments and Sites (ICOMOS), «Charter on the Protection and Management of Underwater Cultural Heritage.» 1996.

[16] M. Capulli, «Il patrimonio culturale sommerso. Ricerche e proposte per il futuro dell'archeologia subacquea in Italia.» 2016.

[17] A. Calantropio, «Geomatic techniques for the documentation of the Underwater Cultural Heritage». 2023.

[18] G. IUCN, «Protection of the Coastal and Marine Environment, vol. Resolution n 17.38. 1988.» 1988.

[19] IUCN General Assembly, «Marine and Coastal Area Conservation». 1944.

[20] G. Kelleher, «Guidelines for marine protected areas». IUCN, Gland, Switzerland and Cambridge, UK, 1999.

[21] «Geomatica per la gestione del territorio - Enciclopedia», Treccani. Consultato: 29 luglio 2024. [Online]. Disponibile su: https://www.treccani.it/enciclopedia/geomatica-per-la-gestione-del-territorio_(Enciclopedia-della-Scienza-e-della-Tecnica)/

[22] D. Naser e T. Hassan, «Mobile Mapping Systems -The New Trend in Mapping and GIS Applications», *Alta. Land Surv.*, lug. 2007.

[23] «Zanichelli_Cannarozzo_Principi_e_strumenti_fotogrammetria.pdf». Consultato: 29 luglio 2024. [Online]. Disponibile su: https://archivio-online.scuola.zanichelli.it/cannarozzomisure-5ed-files/Zanichelli_Cannarozzo_Principi_e_strumenti_fotogrammetria.pdf

[24] «Equazioni di collinearita.pdf». Consultato: 29 luglio 2024. [Online]. Disponibile su: https://moodle2.units.it/pluginfile.php/324656/mod_resource/content/1/Equazioni%20di%20collinearita.pdf

[25] C. S. Fraser, «Digital camera self-calibration». ISPRS Journal of Photogrammetry and Remote Sensing, 1997.

[26] C. McGlone, «Manual of photogrammetry», gen. 2004, Consultato: 29 luglio 2024. [Online]. Disponibile su: https://www.academia.edu/69009469/Manual_of_photogrammetry

[27] «notesEce660Chap5.pdf». Consultato: 29 luglio 2024. [Online]. Disponibile su:

https://web.uettaxila.edu.pk/CMS/coeCGbsSp09/notes%5CEce660Chap5.pdf

[28]   F. Menna e E. Nocerino, «UNDERWATER PHOTOGRAMMETRY». settembre 2024.

[29]   «Rifrazione». Consultato: 21 agosto 2024. [Online]. Disponibile su: https://www.chimica-online.it/download/rifrazione.htm

[30]   «CRC Handbook of Chemistry and Physics 95th Edition.pdf». Consultato: 21 agosto 2024. [Online]. Disponibile su: https://edisciplinas.usp.br/pluginfile.php/4557662/mod_resource/content/1/CRC%20Handbook%20of%20Chemistry%20and%20Physics%2095th%20Edition.pdf

[31]   J. S. Jaffe, «Computer modeling and the design of optimal underwater imaging systems», *IEEE J. Ocean. Eng. Vol 15*, 1990.

[32]   A. Calantropio e F. Chiabrando, «Underwater Cultural Heritage Documentation Using Photogrammetry», *J. Mar. Sci. Eng.*, vol. 12, fasc. 3, Art. fasc. 3, mar. 2024, doi: 10.3390/jmse12030413.

[33]   Y. Wang, W. Song, G. Fortino, L.-Z. Qi, W. Zhang, e A. Liotta, «An Experimental-Based Review of Image Enhancement and Image Restoration Methods for Underwater Imaging», *IEEE Access*, vol. 7, pp. 140233–140251, 2019, doi: 10.1109/ACCESS.2019.2932130.

[34]   Y. Bekerman, S. Avidan, e T. Treibitz, «Unveiling Optical Properties in Underwater Images», in *2020 IEEE International Conference on Computational Photography (ICCP)*, apr. 2020, pp. 1–12. doi: 10.1109/ICCP48838.2020.9105267.

[35]   Menna, F., Agrafiotis, P., Georgopoulos, A., «State of the art and applications in archaeological underwater 3D recording and mapping.», *J. Cult. Herit. 33*, 2018.

[36]   G. Bianco, M. Muzzupappa, F. Bruno, R. Garcia, e L. Neumann, «A NEW COLOR CORRECTION METHOD FOR UNDERWATER IMAGING», *Int. Arch. Photogramm. Remote Sens. Spat. Inf. Sci.*, vol. XL-5-W5, pp. 25–32, apr. 2015, doi: 10.5194/isprsarchives-XL-5-W5-25-2015.

[37]   F. Menna *et al.*, «IMPROVING UNDERWATER ACCURACY BY EMPIRICAL WEIGHTING OF IMAGE OBSERVATIONS», *Int. Arch. Photogramm. Remote Sens. Spat. Inf. Sci.*, vol. XLII–2, pp. 699–705, mag. 2018, doi: 10.5194/isprs-archives-XLII-2-699-2018.

[38]   F. Menna, E. Nocerino, S. Ural, e A. Gruen, «MITIGATING IMAGE RESIDUALS SYSTEMATIC PATTERNS IN UNDERWATER PHOTOGRAMMETRY», *Int. Arch. Photogramm. Remote Sens. Spat. Inf.*

Sci., vol. XLIII-B2-2020, pp. 977–984, ago. 2020, doi: 10.5194/isprs-archives-XLIII-B2-2020-977-2020.

[39]   «Tabelle SSI». Consultato: 13 settembre 2024. [Online]. Disponibile su: http://web.tiscali.it/ektoland/altre/sub/tabelle.html

[40]   D. L. Ruderman, T. W. Cronin, e C.-C. Chiao, «Statistics of cone responses to natural images: implications for visual coding», *JOSA A*, vol. 15, fasc. 8, pp. 2036–2045, ago. 1998, doi: 10.1364/JOSAA.15.002036.

[41]   «Colorimetria 5». Consultato: 2 settembre 2024. [Online]. Disponibile su: http://www.contrografismo.info/TPP/Colorimetria5.html

[42]   «IEC-61966-2-1-1999-AMD1-2003.pdf». Consultato: 20 settembre 2024. [Online]. Disponibile su: https://cdn.standards.iteh.ai/samples/10795/ae461684569b40bbbb2d9a22b1047f05/IEC-61966-2-1-1999-AMD1-2003.pdf

[43]   D. Levy *et al.*, «SeaThru-NeRF: Neural Radiance Fields in Scattering Media», in *2023 IEEE/CVF Conference on Computer Vision and Pattern Recognition (CVPR)*, Vancouver, BC, Canada: IEEE, giu. 2023, pp. 56–65. doi: 10.1109/CVPR52729.2023.00014.

[44]   «SeaThru-NeRF: Neural Radiance Fields in Scattering Media». Consultato: 3 settembre 2024. [Online]. Disponibile su: https://sea-thru-nerf.github.io/

[45]   «Agisoft Metashape User Manual - Professional Edition, Version 2.1».

[46]   «Calculate CIE94 Color Difference of Colors on Test Chart - MATLAB & Simulink - MathWorks Italia». Consultato: 29 agosto 2024. [Online]. Disponibile su: https://it.mathworks.com/help/images/calculate-cie94-color-differences-of-colors-measured-on-test-chart.html

Appendix

Appendix A

Camera calibration

```matlab
% Define images to process
imageFileNames = {' Image Path ' };

% Detect calibration pattern in images
detector = vision.calibration.monocular.CheckerboardDetector();
[imagePoints, imagesUsed] = detectPatternPoints(detector, imageFileNames);
imageFileNames = imageFileNames(imagesUsed);

% Read the first image to obtain image size
originalImage = imread(imageFileNames{1});
[mrows, ncols, ~] = size(originalImage);

% Generate world coordinates for the planar pattern keypoints
squareSize = 10;  % in units of 'centimeters'
worldPoints = generateWorldPoints(detector, 'SquareSize', squareSize);

% Calibrate the camera
[cameraParams, imagesUsed, estimationErrors] = 
estimateCameraParameters(imagePoints, worldPoints, ...
    'EstimateSkew', true, 'EstimateTangentialDistortion', true, ...
    'NumRadialDistortionCoefficients', 3, 'WorldUnits', 'centimeters', ...
    'InitialIntrinsicMatrix', [], 'InitialRadialDistortion', [], ...
    'ImageSize', [mrows, ncols]);

% View reprojection errors
h1=figure; showReprojectionErrors(cameraParams);

% Visualize pattern locations
h2=figure; showExtrinsics(cameraParams, 'CameraCentric');

% Display parameter estimation errors
displayErrors(estimationErrors, cameraParams);

% For example, you can use the calibration data to remove effects of lens
distortion.
undistortedImage = undistortImage(originalImage, cameraParams);


% Extraction of inverse matrix and distortion coefficients
% Intrinsic camera matrix
cameraMatrix = cameraParams.IntrinsicMatrix';

% Inverse matrix
inverseCameraMatrix = inv(cameraMatrix);
```

```matlab
% Distortion coefficients
distortionCoefficients =
[cameraParams.RadialDistortion,cameraParams.TangentialDistortion,
cameraParams.Skew];

% Results
disp(' Intrinsic camera matrix:');
disp(cameraMatrix);
disp(' Inverse matrix: ');
disp(inverseCameraMatrix);
disp(' Distortion coefficients ');
disp(distortionCoefficients);

% Directory to save the correct images
outputDir = ' image saving path';

% Create the directory if it does not exist
if ~exist(outputDir, 'dir')
    mkdir(outputDir);
end

% Itera through all images in the datastore
for i = 1:numel(imageFileNames)
    % Read the original image
    I = imread(imageFileNames{i});

    % Correct image distortion
    J = undistortImage(I, cameraParams);

    % Decompose the file path to obtain the file name and extension
    [~, name, ext] = fileparts(imageFileNames{i});

    % Generate a new file name by adding '_undistorted' to the original name
    newFileName = fullfile(outputDir, [name, '_undistorted', ext]);

    % Save the correct image
    imwrite(J, newFileName);
end

% Creazione del file di  testo con i dati di calibrazione
fileID = fopen('name of the file','w');
fprintf(fileID, 'fx = %f\n', cameraMatrix(1,1));
fprintf(fileID, 'fy = %f\n', cameraMatrix(2,2));
fprintf(fileID, 'cx = %f\n', cameraMatrix(1,3));
fprintf(fileID, 'cy = %f\n', cameraMatrix(2,3));
fprintf(fileID, 'k1 = %f\n', distortionCoefficients(1));
fprintf(fileID, 'k2 = %f\n', distortionCoefficients(2));
fprintf(fileID, 'k3 = %f\n', distortionCoefficients(3));
fprintf(fileID, 'p1 = %f\n', distortionCoefficients(4));
fprintf(fileID, 'p2 = %f\n', distortionCoefficients(5));
fprintf(fileID, 'b1, b2 = %f\n', distortionCoefficients(6));
fclose(fileID);

disp(' Finished processing');
```

Appendix B

Merging image channels

```matlab
% Folder Paths
redFolder = 'Red path';
greenFolder = 'Green path ';
blueFolder = 'Blu path ';

% Read the files
redFiles = dir(fullfile(redFolder, '*.png'));
greenFiles = dir(fullfile(greenFolder, '*.png'));
blueFiles = dir(fullfile(blueFolder, '*.png'));

% Check that all folders have the same number of images
if length(redFiles) ~= length(greenFiles) || length(redFiles) ~=
length(blueFiles)
    error('Folders must contain the same number of images.');
end

% Output directory for saving combined images
outputFolder = ' image saving path ';
if ~exist(outputFolder, 'dir')
    mkdir(outputFolder);
end

% Merge channels for each image
for i = 1:length(redFiles)
    % Read channel images
    redImage = imread(fullfile(redFolder, redFiles(i).name));
    greenImage = imread(fullfile(greenFolder, greenFiles(i).name));
    blueImage = imread(fullfile(blueFolder, blueFiles(i).name));

    % If the image has more than two dimensions, extract only the first channel
if ndims(redImage) > 2
        redImage = redImage(:,:,1);
    end
    if ndims(greenImage) > 2
        greenImage = greenImage(:,:,1);
    end
    if ndims(blueImage) > 2
        blueImage = blueImage(:,:,1);
    end

    % Check that the dimensions of the images are the same
    if ~isequal(size(redImage), size(greenImage)) || ~isequal(size(redImage),
size(blueImage))
        error(' Images must be the same size.');
    end

    % Combine channels into a single RGB image
    rgbImage = cat(3, redImage, greenImage, blueImage);

    % Convert the combined image to uint8 if necessary
    if ~isa(rgbImage, 'uint8')
```

```matlab
        rgbImage = uint8(rgbImage);
    end

    % Generates the output file name
    [~, name, ext] = fileparts(redFiles(i).name);
    outputFileName = fullfile(outputFolder, [name, '_combined', ext]);

    % Save the combined image
    try
        imwrite(rgbImage, outputFileName);
    catch ME
        disp(['Error while saving the file:', outputFileName]);
        disp(ME.message);
    end

end

disp(' Finished processing.');
```

Appendix C

Calculate CIE94 Color Difference of Colors on Test Chart

```matlab
%Image reading
I = imread("Image Path ");

%Graph with colour codes
chart = colorChecker(I);
displayChart(chart)

%Measure colour and return in a table
colorTable = measureColor(chart);

%Measured and reference colour display
displayColorPatch(colorTable)
disp(colorTable.Properties.VariableNames);

%Extracting colour values between RGB and LAB
referenceLab = colorTable{:,["Reference_L","Reference_a","Reference_b"]};
measuredRGB = colorTable{:,["Measured_R","Measured_G","Measured_B"]};


disp(' Finished processing.');
```

Appendix D

```matlab
measuredLab = rgb2lab(measuredRGB,WhitePoint="d50");

%Graphs value 'l', 'a' and 'b'
figure
plot(referenceLab(:,2),measuredLab(:,2),"xr");
figure
plot(referenceLab(:,3),measuredLab(:,3),"xb");
figure
plot(referenceLab(:,1),measuredLab(:,1),"xc");

%Image reading
I_dacal = imread("Image Path ");
I_lab_dacal= rgb2lab(I_dacal,WhitePoint="d50");
dim_im=size(I_dacal);
I_cal= I_lab_dacal;

%Correction of each pixel
for r=1:dim_im(1)
    for c=1:dim_im(2)

        I_cal(r,c,2)=interp1(measuredLab(:,2),referenceLab(:,2),I_lab_dacal(r,c,2
        ));

        I_cal(r,c,3)=interp1(measuredLab(:,3),referenceLab(:,3),I_lab_dacal(r,c,3
        ));
```

```matlab
        end
        r
end

%Correct image
I_cal_rgb=lab2rgb(I_cal,WhitePoint="d50");

figure
imshow(I_cal_rgb);

disp(' Finished processing.');
```

Appendix E

Report of calibration for dataset of Coluccia island

Agisoft Metashape

Processing Report
19 July 2024

Survey Data
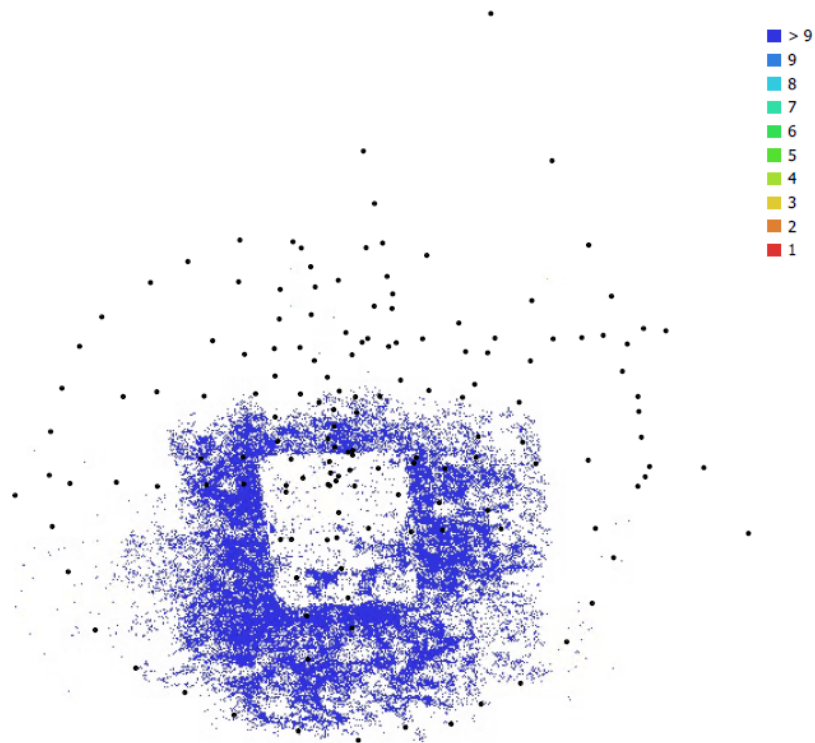
Fig. 1. Camera locations and image overlap.

Number of images:	152	Camera stations:	152
		Tie points:	55,098
		Projections:	133,001
		Reprojection error:	1.97 pix

Camera Model	Resolution	Focal Length	Pixel Size	Precalibrated
unknown	4000 x 2672	unknown	unknown	No

Table 1. Cameras.

Camera Calibration
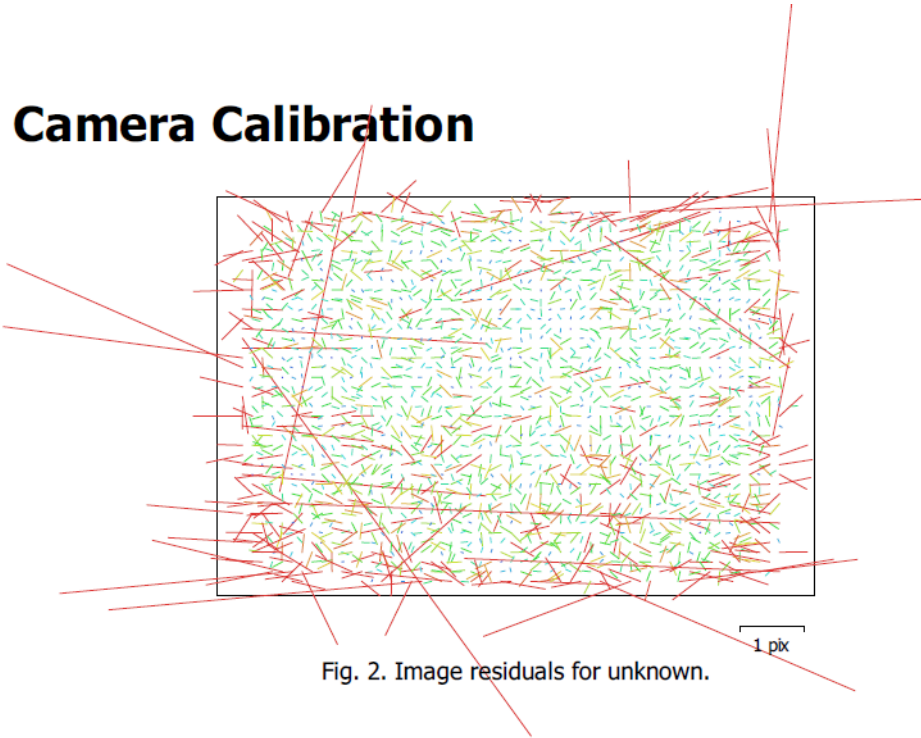
Fig. 2. Image residuals for unknown.

unknown

152 images

Type	Resolution	Focal Length	Pixel Size
Frame	**4000 x 2672**	**unknown**	**unknown**

	Value	Error	F	Cx	Cy	B1	B2	K1	K2	K3	P1	P2
F	**3946.05**	0.65	1.00	0.03	-0.56	0.02	-0.12	-0.20	0.23	-0.20	0.03	-0.34
Cx	**15.0425**	0.57		1.00	-0.02	-0.06	0.04	0.08	-0.06	0.05	0.94	-0.02
Cy	**-1.76679**	0.61			1.00	-0.14	0.07	-0.02	-0.02	0.02	-0.01	0.86
B1	**-0.463918**	0.082				1.00	0.03	-0.04	-0.00	0.01	-0.07	-0.00
B2	**-0.276839**	0.065					1.00	-0.01	0.01	-0.02	0.07	-0.01
K1	**0.00569726**	0.001						1.00	-0.97	0.91	0.08	-0.03
K2	**-0.0291941**	0.0089							1.00	-0.98	-0.07	-0.01
K3	**0.0538605**	0.023								1.00	0.06	0.02
P1	**0.00138336**	5.1e-05									1.00	-0.01
P2	**-0.000295159**	5e-05										1.00

Table 2. Calibration coefficients and correlation matrix.

Processing Parameters

General

Cameras	152
Aligned cameras	152
Markers	16
Coordinate system	Local Coordinates (m)
Rotation angles	Yaw, Pitch, Roll

Point Cloud

Points	55,098 of 63,159
RMS reprojection error	0.207868 (1.97053 pix)
Max reprojection error	1.08879 (36.7274 pix)
Mean key point size	8.66784 pix
Point colors	3 bands, uint8
Key points	No
Average tie point multiplicity	2.50941

Alignment parameters

Accuracy	Medium
Generic preselection	Yes
Reference preselection	No
Key point limit	40,000
Tie point limit	4,000
Exclude stationary tie points	Yes
Guided image matching	No
Adaptive camera model fitting	No
Matching time	1 minutes 34 seconds
Matching memory usage	446.25 MB
Alignment time	42 seconds
Alignment memory usage	72.30 MB

Optimization parameters

Parameters	f, b1, b2, cx, cy, k1-k3, p1, p2
Adaptive camera model fitting	No
Optimization time	1 seconds
Software version	1.7.0.11736
File size	5.07 MB

System

Software name	Agisoft Metashape Professional
Software version	1.7.0 build 11736
OS	Windows 64 bit
RAM	31.73 GB
CPU	Intel(R) Core(TM) i7-10850H CPU @ 2.70GHz
GPU(s)	NVIDIA GeForce RTX 2080 Super with Max-Q Design

188

Appendix F

Report of calibration for dataset of Porto Cesareo (stereographic cameras)

Agisoft Metashape

Processing Report
23 September 2024

Survey Data
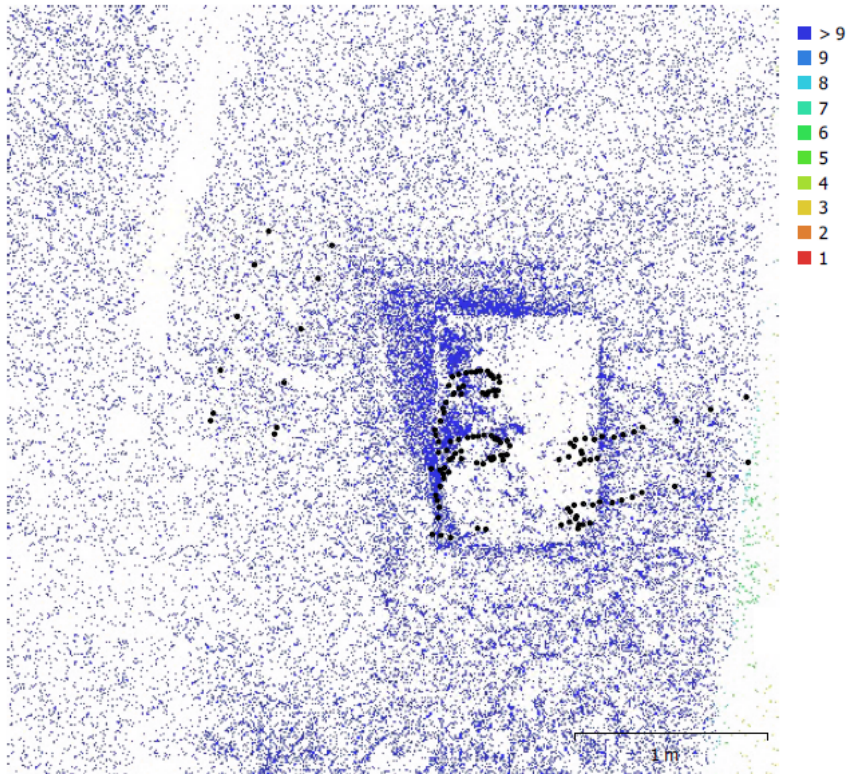
Fig. 1. Camera locations and image overlap.

Number of images:	140	Camera stations:	136
Flying altitude:	2.42 m	Tie points:	69,921
Ground resolution:	0.457 mm/pix	Projections:	551,785
Coverage area:	2.49 m²	Reprojection error:	25.1 pix

era Model	Resolution	Focal Length	Pixel Size	Precalibr
R1, 17mm F4 DG DN | Contemporary 023 (17mm)	9504 x 6336	17 mm	3.79 x 3.79 µm	No
R1, 17mm F4 DG DN | Contemporary 023 (17mm)	9504 x 6336	17 mm	3.79 x 3.79 µm	No

Table 1. Cameras.

Camera Calibration

13 pix

Fig. 2. Image residuals for ILX-LR1, 17mm F4 DG DN | Contemporary 023 (17mm).

ILX-LR1, 17mm F4 DG DN | Contemporary 023 (17mm)
70 images

Type	Resolution	Focal Length	Pixel Size
Frame	**9504 x 6336**	**17 mm**	**3.79 x 3.79 μm**

	Value	Error	F	Cx	Cy	B1	B2	K1	K2	K3	P1	P2
F	5297.77	3.6	1.00	-0.09	-0.20	0.07	-0.04	0.02	-0.02	0.10	-0.04	0.04
Cx	22.068	2.9		1.00	0.02	-0.07	0.11	0.02	0.00	0.02	0.85	0.05
Cy	99.8917	2.7			1.00	-0.17	-0.05	0.06	-0.02	-0.02	0.05	0.77
B1	6.27314	0.68				1.00	0.04	0.02	-0.02	0.04	-0.21	-0.02
B2	-12.9544	0.65					1.00	0.04	-0.03	0.02	0.06	-0.20
K1	0.0117169	0.0008						1.00	-0.93	0.87	0.00	0.08
K2	-0.0528834	0.0016							1.00	-0.98	-0.01	-0.06
K3	0.0414856	0.0011								1.00	0.03	0.04
P1	0.0044503	0.00014									1.00	0.05
P2	0.00357976	0.00011										1.00

Table 2. Calibration coefficients and correlation matrix.

191

Camera Calibration

Fig. 3. Image residuals for ILX-LR1, 17mm F4 DG DN | Contemporary 023 (17mm).

ILX-LR1, 17mm F4 DG DN | Contemporary 023 (17mm)

70 images

Type	Resolution	Focal Length	Pixel Size
Frame	**9504 x 6336**	**17 mm**	**3.79 x 3.79 μm**

	Value	Error	F	Cx	Cy	B1	B2	K1	K2	K3	P1	P2
F	**5251.48**	3.6	1.00	-0.14	-0.20	0.08	-0.08	-0.05	0.11	-0.06	-0.11	0.06
Cx	**-4.92918**	2.8		1.00	0.02	-0.12	0.15	-0.00	-0.02	0.01	0.85	0.06
Cy	**103.246**	2.6			1.00	-0.16	-0.12	0.02	0.00	-0.02	0.04	0.74
B1	**4.19233**	0.62				1.00	0.06	-0.01	0.03	-0.02	-0.18	-0.01
B2	**-9.40817**	0.62					1.00	-0.03	0.02	-0.02	0.08	-0.18
K1	**-0.0413795**	0.0007						1.00	-0.93	0.86	-0.01	0.02
K2	**0.0276203**	0.0013							1.00	-0.98	-0.01	-0.01
K3	**-0.00304565**	0.00079								1.00	0.00	0.00
P1	**0.0025615**	0.00013									1.00	0.03
P2	**0.00441819**	0.0001										1.00

Table 3. Calibration coefficients and correlation matrix.

Ground Control Points
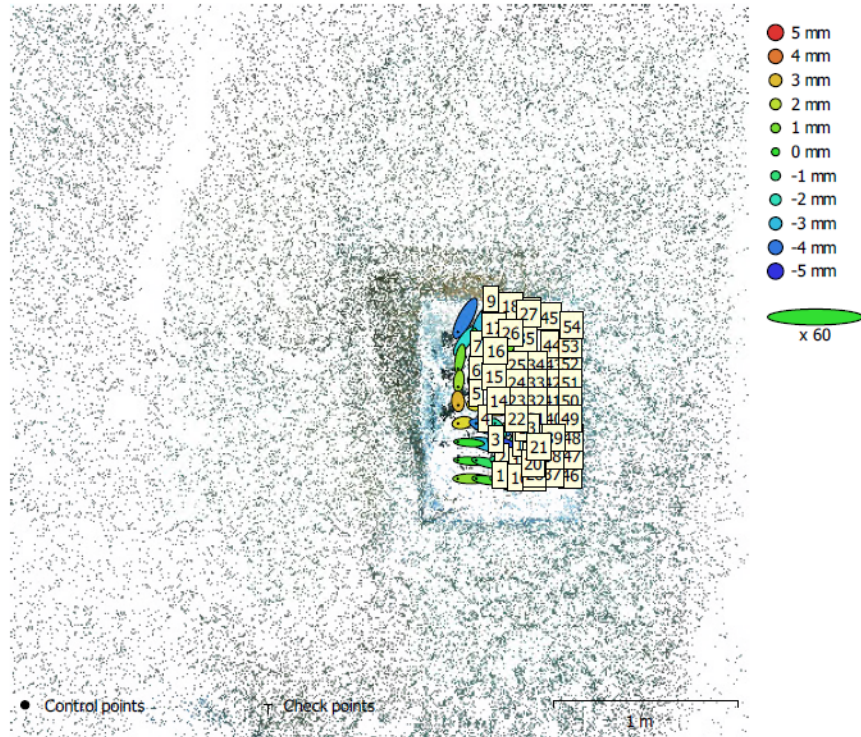
Fig. 4. GCP locations and error estimates.
Z error is represented by ellipse color. X,Y errors are represented by ellipse shape.
Estimated GCP locations are marked with a dot or crossing.

Count	X error (mm)	Y error (mm)	Z error (mm)	XY error (mm)	Total (mm)
54	1.22671	0.936507	1.81535	1.54333	2.38272

Table 4. Control points RMSE.

193

Label	X error (mm)	Y error (mm)	Z error (mm)	Total (mm)	Image (pix)
43	0.96855	0.214913	1.50294	1.80086	2.945 (39)
42	1.22432	0.870187	1.07148	1.84507	3.084 (39)
44	0.685004	-0.479522	0.967618	1.27885	3.509 (39)
34	1.08715	-0.164371	1.89622	2.19194	3.352 (38)
41	1.47163	1.32274	0.836038	2.14809	3.610 (38)
9	-1.30791	-2.47773	-3.82016	4.73745	3.768 (38)
33	1.28447	0.508844	2.07305	2.49125	3.557 (38)
46	0.957382	-0.349303	-0.479592	1.12632	4.221 (38)
45	0.325293	-1.01697	-0.859059	1.37041	3.896 (38)
52	0.762447	0.506623	0.250315	0.949026	3.119 (37)
51	1.05017	0.987987	0.222994	1.45901	2.994 (37)
50	1.32694	1.30697	-0.0401734	1.86294	3.257 (37)
35	0.752749	-0.777074	0.89518	1.40422	3.389 (37)
53	0.499665	-0.00211964	-0.0564803	0.502852	3.573 (37)
2	-2.48102	0.155465	0.193029	2.49337	4.487 (37)
8	-1.26963	-1.75928	-2.36006	3.20576	3.752 (37)
36	0.463837	-1.531	-0.59059	1.70526	4.041 (37)
32	1.66994	0.538923	3.21422	3.66202	3.701 (37)
40	1.57363	1.27559	1.64613	2.61021	4.240 (37)
7	-0.333263	-1.78955	0.982064	2.06833	3.033 (36)
18	-1.00104	-1.88546	-3.02424	3.70177	3.237 (36)
47	0.782433	0.107608	-0.728867	1.07472	3.683 (36)
37	0.643505	0.257029	0.315862	0.761532	3.593 (36)
25	0.78365	-0.587482	1.67444	1.93984	3.422 (36)
38	0.821468	0.612051	-0.0887077	1.02824	3.340 (36)
17	0.179839	-1.67567	0.000890443	1.6853	3.559 (36)
1	-2.3636	0.00890244	1.30243	2.6987	4.475 (36)
11	-2.20542	0.519065	-0.716821	2.37637	4.319 (36)
48	1.58119	0.859531	-0.822881	1.97891	3.590 (36)
54	0.0983592	-0.171766	-2.12539	2.13459	3.878 (36)
49	1.39748	1.36748	-0.42063	1.99997	3.560 (36)

Label	X error (mm)	Y error (mm)	Z error (mm)	Total (mm)	Image (pix)
6	-0.119351	-1.07156	1.578	1.91117	3.485 (36)
24	0.368958	0.0157979	1.37811	1.42673	3.567 (36)
5	0.0405769	-0.727589	3.1077	3.19199	3.625 (36)
15	0.374378	-0.555798	2.05776	2.16413	3.601 (36)
27	-0.962093	-1.15733	-2.99368	3.3507	3.761 (36)
31	1.61864	1.14706	2.57191	3.24815	4.009 (36)
26	0.46831	-1.07076	0.362122	1.22351	3.509 (35)
4	-0.778797	-0.140109	2.58486	2.70327	3.549 (35)
23	0.255705	0.324781	1.56023	1.61406	3.378 (35)
10	-2.10236	0.298404	0.367029	2.15491	4.293 (35)
30	0.0158979	0.947213	-1.54662	1.81369	3.377 (35)
19	-1.68131	0.367533	-1.14399	2.06654	4.326 (35)
39	0.680296	0.824605	-1.56521	1.89543	3.457 (35)
28	0.580273	0.667029	0.536065	1.03393	3.706 (35)
12	-2.30847	0.57183	-2.91932	3.76543	4.301 (35)
14	0.361337	-0.0468567	2.51861	2.54483	3.827 (35)
13	-2.5109	0.768942	-3.74137	4.57096	4.461 (35)
16	0.221565	-1.14154	1.42606	1.84007	3.352 (35)
3	-2.03573	0.141041	-0.0678203	2.04173	3.813 (34)
29	0.0482794	0.760077	-1.13284	1.36505	3.531 (34)
22	-0.634651	0.81979	-1.79693	2.07456	3.461 (34)
20	-1.49312	0.666764	-1.44422	2.18168	4.058 (34)
21	-1.83668	0.838073	-4.60771	5.03058	4.562 (34)
Total	**1.22671**	**0.936507**	**1.81535**	**2.38272**	**3.707**

Table 5. Control points.

Processing Parameters

General

Cameras	140
Aligned cameras	136
Markers	54
Coordinate system	Local Coordinates (m)
Rotation angles	Yaw, Pitch, Roll

Point Cloud

Points	69,921 of 77,807
RMS reprojection error	4.25226 (25.0843 pix)
Max reprojection error	14.5672 (643.204 pix)
Mean key point size	7.17322 pix
Point colors	3 bands, uint8
Key points	No
Average tie point multiplicity	7.93992

Alignment parameters

Accuracy	Medium
Generic preselection	Yes
Reference preselection	No
Key point limit	40,000
Tie point limit	4,000
Exclude stationary tie points	Yes
Guided image matching	No
Adaptive camera model fitting	No
Matching time	1 minutes 48 seconds
Matching memory usage	893.68 MB
Alignment time	43 seconds
Alignment memory usage	91.34 MB

Optimization parameters

Parameters	f, b1, b2, cx, cy, k1-k3, p1, p2
Adaptive camera model fitting	No
Optimization time	2 seconds
Software version	1.7.0.11736
File size	11.27 MB

System

Software name	Agisoft Metashape Professional
Software version	1.7.0 build 11736
OS	Windows 64 bit
RAM	63.73 GB
CPU	Intel(R) Core(TM) i7-14700KF
GPU(s)	NVIDIA GeForce RTX 4070 SUPER

196

Processing parameters of Porto Cesareo dataset

Agisoft Metashape

Processing Report
23 September 2024
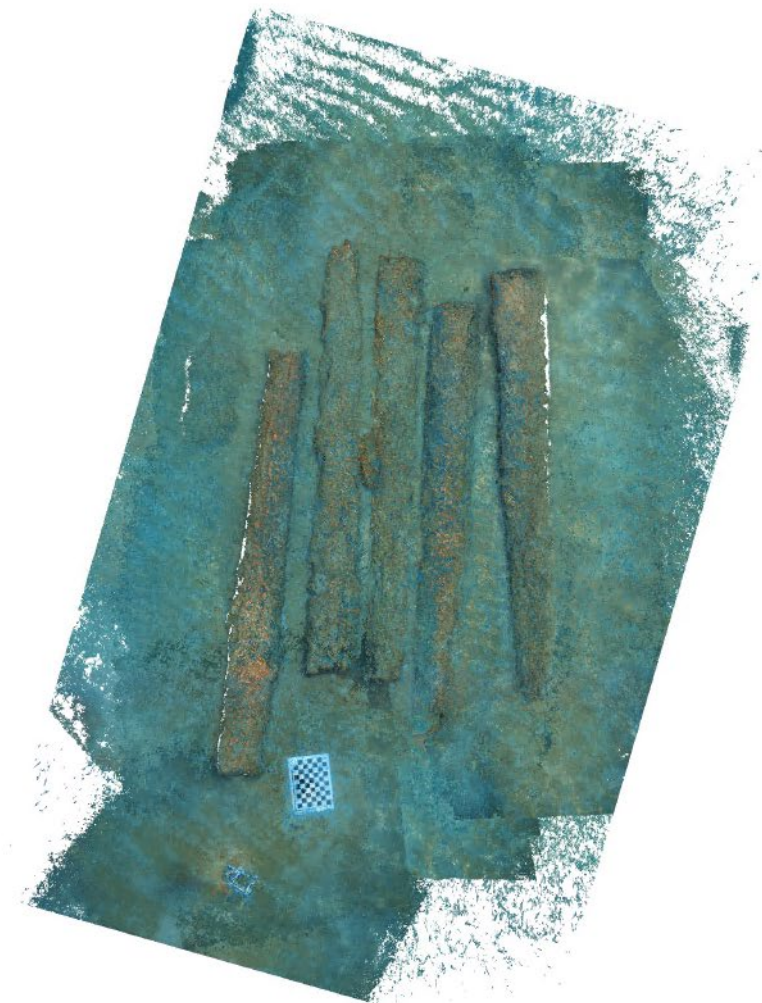
Processing Parameters

General

Cameras	1394
Aligned cameras	1379
Coordinate system	Local Coordinates (m)
Rotation angles	Yaw, Pitch, Roll

Point Cloud

Points	1,041,892 of 1,144,462
RMS reprojection error	0.169957 (1.41896 pix)
Max reprojection error	0.513715 (91.3346 pix)
Mean key point size	7.42552 pix
Point colors	3 bands, uint8
Key points	No
Average tie point multiplicity	4.98736

Alignment parameters

Accuracy	Medium
Generic preselection	Yes
Reference preselection	Source
Key point limit	40,000
Tie point limit	4,000
Exclude stationary tie points	Yes
Guided image matching	No
Adaptive camera model fitting	No
Matching time	32 minutes 47 seconds
Matching memory usage	1.03 GB
Alignment time	25 minutes 50 seconds
Alignment memory usage	1.57 GB
Software version	1.7.0.11736
File size	114.40 MB

Depth Maps

Count	1378

Depth maps generation parameters

Quality	Medium
Filtering mode	Mild
Processing time	1 hours 5 minutes
Memory usage	10.69 GB
Software version	1.7.0.11736
File size	8.12 GB

Dense Point Cloud

Points	182,611,074
Point colors	3 bands, uint8

Depth maps generation parameters

Quality	Medium
Filtering mode	Mild
Processing time	1 hours 5 minutes
Memory usage	10.69 GB

Dense cloud generation parameters

Processing time	13 hours 10 minutes
Memory usage	27.97 GB
Software version	1.7.0.11736
File size	2.36 GB

Model
  Faces   16,717,391
  Vertices   8,373,567
  Vertex colors   3 bands, uint8
  Texture   4,096 x 4,096, 4 bands, uint8
  Depth maps generation parameters
    Quality   Medium
    Filtering mode   Mild
    Processing time   1 hours 5 minutes
    Memory usage   10.69 GB
  Reconstruction parameters
    Surface type   Arbitrary
    Source data   Dense cloud
    Interpolation   Enabled
    Strict volumetric masks   No
    Processing time   21 minutes 6 seconds
    Memory usage   38.37 GB
  Texturing parameters
    Mapping mode   Generic
    Blending mode   Mosaic
    Texture size   4,096
    Enable hole filling   Yes
    Enable ghosting filter   Yes
    UV mapping time   4 minutes 17 seconds
    UV mapping memory usage   3.58 GB
    Blending time   5 hours 1 minutes
    Blending memory usage   7.98 GB
  Software version   1.7.0.11736
  File size   735.43 MB
Tiled Model
  Texture   3 bands, uint8
  Depth maps generation parameters
    Quality   Medium
    Filtering mode   Mild
    Processing time   1 hours 5 minutes
    Memory usage   10.69 GB
  Reconstruction parameters
    Source data   Dense cloud
    Tile size   256
    Face count   Low
    Enable ghosting filter   No
    Processing time   2 hours 28 minutes
    Memory usage   4.71 GB
  Software version   1.7.0.11736
  File size   498.95 MB
Orthomosaic
  Size   20,410 x 31,074
  Coordinate system   Local Coordinates (m)
  Colors   3 bands, uint8
  Reconstruction parameters
    Blending mode   Mosaic
    Surface   Mesh
    Enable hole filling   Yes
    Enable ghosting filter   No
    Processing time   3 hours 20 minutes
    Memory usage   16.73 GB

199

Software version   1.7.0.11736

File size   35.15 GB

System

Software name   Agisoft Metashape Professional

Software version   1.7.0 build 11736

OS   Windows 64 bit

RAM   63.73 GB

CPU   Intel(R) Core(TM) i7-14700KF

GPU(s)   NVIDIA GeForce RTX 4070 SUPER

Appendix H

Mesh wireframe view

Ortophoto

Ortophoto in the context